

©Copyright 2012

Jennifer C. Gadd

Single-Molecule Studies for the Characterization of Synaptic Vesicles

Jennifer C. Gadd

A dissertation
submitted in partial fulfillment
of the requirements for the degree of

Doctor of Philosophy

University of Washington

2012

Reading Committee:
Daniel T. Chiu, Chair
Dustin J. Maly
Robert E. Synovec

Program Authorized to Offer Degree:

Chemistry

University of Washington

Abstract

Single-Molecule Studies for the Characterization of Synaptic Vesicles

Jennifer C. Gadd

Chair of the Supervisory Committee:
Professor Daniel T. Chiu
Chemistry

Synaptic vesicles are subcellular organelles that are found in the synaptic bouton and are responsible for the propagation of signals between neurons. Synaptic vesicles undergo a fast and tightly regulated cycle in which exocytosis to release neurotransmitters and endocytosis to recycle empty vesicles take place for efficient neuronal communication. This dissertation reports the development and application of analytical techniques for the characterization of various physical properties of synaptic vesicles at the single vesicle/molecule level. First, two complementary techniques, single-particle tracking and fluorescence correlation spectroscopy (FCS), for sizing nanoparticles in free solution by confinement within picoliter volume aqueous droplets will be described. Single-particle tracking works well with bright particles that can be continuously illuminated and imaged and was used to size single fluorescent beads. While FCS detects small intensity bursts from particles or molecules diffusing through the confocal probe volume, which works well with dim and rapidly diffusing particles or molecules, was used to size individual synaptic vesicles.

Next, a method to determine both the average number and variance of proteins in the few to tens of copies in isolated synaptic vesicles will be described. Other currently available protein quantification techniques provide an average number but lack information on the intervesicler

variability of protein number, and thus on the precision with which proteins are sorted to vesicles. The technique we present entails labeling the synaptic vesicles with fluorescent primary-secondary antibody complexes, TIRF (total internal reflection fluorescence) microscopy imaging of the vesicles, digital image analysis, and deconvolution of the fluorescence intensity data. With this technique, 7 major membrane proteins were quantified and we found that the proteins fell into 2 classes; proteins that were monodispersed and polydispersed number. The use of photobleaching as an alternative to obtaining an accurate calibration intensity distribution from the sample directly will be discussed.

Finally, the initial steps towards the utilization of the exo- and endocytosis of synaptic vesicles to load nanoparticles as a means of probing the interior of the vesicles will be reported. We have developed a highly sensitive pH-sensing polymer dot, which we plan to use to probe the intravesicular pH of synaptic vesicles.

Table of Contents

	Page
List of Figures	vi
List of Tables	viii
Chapter 1: Introduction to Synaptic Vesicles	1
1.1 Synaptic Transmission and the Synaptic Vesicle Cycle	1
1.2 Chapter References	5
Chapter 2: Sizing Subcellular Organelles and Nanoparticles Confined within Aqueous Droplets.....	7
2.1 Introduction	7
2.2 Materials and Methods.....	9
2.2.1 Materials	9
2.2.2 Synaptic Vesicle Preparation	9
2.2.3 Droplet Preparation.....	10
2.2.4 Experimental Setup for FCS and Particle Tracking.....	11
2.2.5 Simulations of Particle Diffusion in a Confined Volume.....	13
2.3 Results and Discussion.....	15
2.3.1 Measuring Diffusion Coefficient in a Droplet with Single-Particle Tracking.....	16

2.3.2	Accurate Sizing of Synaptic Vesicles in Droplets with Fluorescence Correlation Spectroscopy.....	21
2.3.3	Factors That Affect Accurate Sizing in Droplets.....	22
2.4	Conclusion.....	29
2.5	Chapter References	30
Chapter 3: Synaptic Vesicle Protein Quantification at the Single Vesicle Level by Quantitative Microscopy		
		34
3.1	Introduction	34
3.2	Materials and Preparation of Synaptic Vesicle Samples.....	39
3.2.1	Antibodies	39
3.2.2	Isolation of vesicles from brain homogenates	40
3.2.3	Preparation of vesicles for fluorescence imaging	40
3.3	Experimental Design and Equipment Setup.....	41
3.3.1	Design and fabrication of microfluidic chips.....	41
3.3.2	Microscope Setup.....	43
3.3.3	Image Acquisition.....	45
3.3.4	Two-color labeling and selection of antibody	45
3.3.5	Determining antibody concentration and the average protein copy number.	47
3.3.6	Image Analysis.....	50

3.3.7	Data Analysis and Fitting of Fluorescence Intensity Distributions	54
3.4	Results	56
3.4.1	Calculating the Average Number of Seven Membrane Proteins in Brain Synaptic Vesicles	56
3.4.2	Variance in Vesicle Protein Number — How Accurately are Vesicle Proteins Sorted?	59
3.5	Discussion	63
3.5.1	Quantitative Single Vesicle Imaging Provides Information on the Variance in Vesicle Composition.....	64
3.5.2	Functional Implications of Vesicle Protein Number and Variability	64
3.6	Chapter References	66
Chapter 4:	Single-Molecule Fluorescence Quantification with a Photobleached Internal Standard	70
4.1	Introduction	70
4.2	Materials and Methods	71
4.2.1	Materials	71
4.2.2	SynaptopHluorin Vesicle Isolation	71
4.2.3	Sample Imaging and Photobleaching.....	72
4.2.4	Extraction of Initial and Final Intensity Distributions	73

4.2.5	Data Analysis	75
4.3	Results and Discussion.....	75
4.3.1	Optimization of Intensity Extraction from Photobleaching Track	75
4.3.2	Quantifying Fluorophores in Alexa Labeled Antibodies and SpH Vesicles	78
4.4	Conclusion.....	80
4.5	Chapter References	80
Chapter 5:	Probing the Interior of Synaptic Vesicles with Internalized Nanoparticles.....	82
5.1	Introduction	82
5.2	pH Sensing Semiconducting Polymer Dots	83
5.2.1	Materials	83
5.2.2	Generation of pH Sensing Pdot.....	84
5.2.3	Characterization of pH Sensitivity.....	85
5.3	Synaptosomes as a Loading Platform for Nanoparticles into Synaptic Vesicles.....	87
5.3.1	Materials	87
5.3.2	Loading Nanoparticles into Synaptic Vesicles	87
5.3.3	Verifying Loading of Nanoparticles into Synaptic Vesicles	90
5.4	Considerations when Loading Polymer Dots into Synaptic Vesicles	91
5.5	Conclusion.....	93
5.6	Chapter References	94

List of References 96

List of Figures

Figure Number	Page
Figure 1-1: Steps in the synaptic transmission process.....	2
Figure 1-2: Potential synaptic vesicle endocytosis pathways.....	3
Figure 2-1: Experimental set-up for particle sizing.....	10
Figure 2-2: Array of shell beads for approximations of diffusion coefficient.....	12
Figure 2-3: Distributions of position displacements from particle tracking.....	19
Figure 2-4: Fluorescence correlation curves of synaptic vesicles.....	20
Figure 2-5: f/f_0 for beads encapsulated within droplets.....	23
Figure 2-6: Actual vs. apparent diameter from FCS measurements in droplets.....	27
Figure 3-1: Steps to synaptic vesicle protein quantification.....	36
Figure 3-2: Imaging chip design and optical set-up schematic.....	42
Figure 3-3: Labeled synaptic vesicle photostability.....	44
Figure 3-4: Schematic of antibody labeling.....	46
Figure 3-5: Antibody binding stability.....	47
Figure 3-6: Synaptic vesicle labeling verification.....	48
Figure 3-7: Antibody dilution curves.....	49
Figure 3-8: Generation of calibration distributions.....	55
Figure 3-9: Quantification of monodispersed synaptic vesicle proteins.....	60
Figure 3-10: Quantification of polydispersed synaptic vesicle proteins.....	62
Figure 4-1: Photobleaching of GFP in synaptopHluorin vesicles.....	74

Figure 4-2:	Number of GFP distribution in synaptopHluorin vesicles.....	79
Figure 5-1:	Preparation schematic of pH Pdots.....	84
Figure 5-2:	Calibrations of pH Pdots.....	85
Figure 5-3:	pH Pdots in live HeLa cells.....	86
Figure 5-4:	Schematic of uptake of Qdots and FM4-64 into synaptic vesicles.....	89
Figure 5-5:	Images of synaptic vesicles loaded with Qdots and FM4-64.....	90
Figure 5-6:	Images of synaptic vesicles loaded with Qdots and FM4-64 treated with BHQ...	91
Figure 5-7:	Size distributions of Qdots and Pdots.....	92

List of Tables

Table Number	Page
Table 3-1: List of antibody dilutions.....	40
Table 3-2: Average number of synaptic vesicle proteins.....	58
Table 3-3: SV2 and VAMP2 Western analysis.....	58

Acknowledgments

I wish to thank my advisor, Dr. Daniel T. Chiu, for giving me the opportunity to pursue an area of chemistry that I initially knew little about. Thanks to your guidance I learned to take on tough problems and see it from a variety of directions to pursue all possible solutions. I greatly appreciate your encouragement and support when some of those tough problems almost got the best of me.

Dr. Sandra M. Bajjalieh deserves a huge thank you. Many times over the years you served as a second advisor to me. Your door was always open for discussions on science and provided extra support and encouragement that I am grateful for.

I would like to thank the people who worked on the vesicle project with me. Thanks Sarah Mutch for letting me join her and the group of amazing people tackling this tough problem. Patricia Kensel-Hammes, thanks for all the amazing samples you made over the years. The past years would be much harder without all the great help and advice from Bryant Fujimoto.

A big shout out goes to all the Chiu group members (past and present). You all provided a great atmosphere to work in and the willingness of each member to help each other when needed was appreciated. Thanks to Kady Gregersen, Gloria Yen, and Max Zeigler for being more than just my lab mates. The friendships we have developed over the years will stick with me. Thanks to all my friends throughout the Chemistry Department. You all saved me from the insanity of being stuck in the Bagely basement.

Finally, I need to thank my whole family. Thanks to my sister, Jamie, and brother-in-law, Will. It has been a life saver having family in town during this process. You introduced me to an excellent group of friends outside of the University that have served to keep me from becoming an introverted scientist. Thanks to my brother, Jason, for demonstrating a courage in his life decisions over the years that I have found inspirational. Thanks to all the Eckman's and Gadd's spread across the state of California and the country for being my cheerleaders.

Most importantly, thanks to my parents, Eric and Patrice. No words can describe how important you were to me over these past years. You were always there for me no matter what I needed, whether it was just a weekly phone call or an amazing trip to just get away together to help clear my mind. I would not be where I am or the person I am without you. Thank you!

Dedication

To my parents, thanks to the strength you give me I can do anything. I love you!

Chapter 1: Introduction to Synaptic Vesicles

1.1 Synaptic Transmission and the Synaptic Vesicle Cycle

Synaptic vesicles, neurotransmitter-containing vesicles, are responsible for the propagation of signals between neurons through synaptic transmission. Synaptic vesicles are subcellular organelles, 40 to 60nm in diameter,^{1,2} found in neurons localized near synapses in presynaptic terminals, or synaptic boutons. During synaptic transmission (Figure 1-1), the arrival of an action potential in a presynaptic terminal triggers an influx of local Ca^{2+} through activation of voltage-dependent Ca^{2+} channels. The localized increase of Ca^{2+} triggers exocytosis of synaptic vesicles located at the active zone opposite the synaptic cleft. Fusion of synaptic vesicles with the synaptic membrane releases neurotransmitters into the synaptic cleft. The neurotransmitters diffuse across the synaptic cleft towards the dendritic spine and activate the postsynaptic receptors.³ The arrival of an action potential at a presynaptic terminal does not guarantee release of neurotransmitters through synaptic vesicle fusion. Studies have shown that that only 10% - 20% of action potentials actually trigger a release.^{4,5} Both intracellular messengers and extracellular modulators contribute to the relationship between action potentials and neurotransmitter release.

When release occurs, exocytosis of the synaptic vesicle releasing neurotransmitters into the synaptic cleft takes place in under 1 msec.⁶ The synaptic vesicle cycle (SV cycle) primes synaptic vesicles for rapid exocytosis and recycles empty vesicles. There are 4 main parts to the

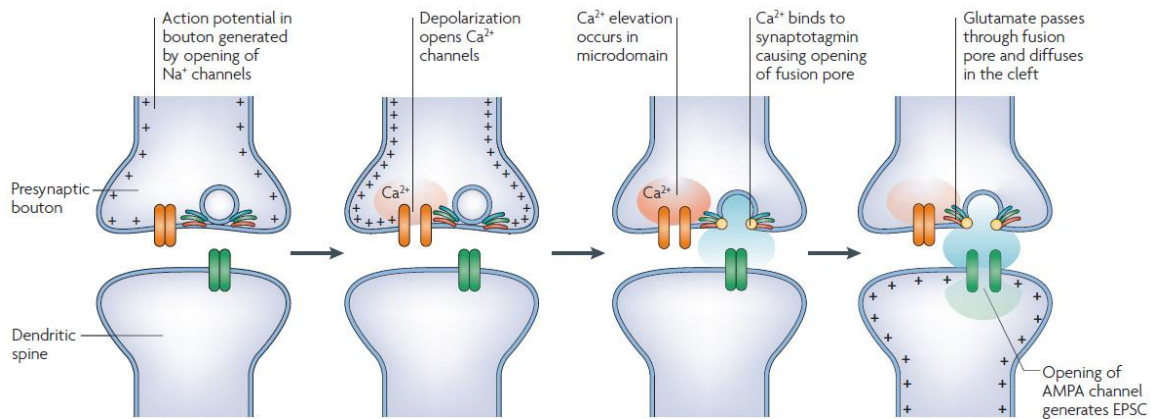


Figure 1-1. Basic steps in the process of synaptic transmission for glutamatergic synapses.³

SV cycle: (1) docking, (2) priming, (3) fusion/exocytosis, and (4) endocytosis/recycling. During the docking stage, synaptic vesicles filled with neurotransmitters translocate to the active zone and make initial contact with the synaptic membrane. Docked vesicles make up what is known as the readily releasable pool.^{7,8} Synaptic vesicles that are simply docked to the membrane do not undergo Ca²⁺ triggered fusion⁹ suggesting a priming step. During priming a partial fusion of the synaptic vesicle with the membrane may take place preparing the vesicle for exocytosis upon detection of a Ca²⁺ signal.⁶ Once primed, influx of Ca²⁺ from an action potential causes synaptic vesicles to undergo rapid exocytosis through partial or full fusion with the synaptic membrane.

After releasing neurotransmitters, synaptic vesicles endocytosis and recycling in 3 main purposed pathways (Figure 1-2): (1) kiss-and-stay, (2) kiss-and-run, and (3) clathrin-dependent endocytosis. For synaptic vesicles undergoing both kiss-and-stay and kiss-and-run, neurotransmitters are released through a narrow pore formed by partial fusion of the vesicle with the synaptic membrane.¹⁰ Upon closer of the narrow pore, synaptic vesicles undergoing kiss-and-stay remain docked during reacidification and neurotransmitter uptake allowing the vesicle

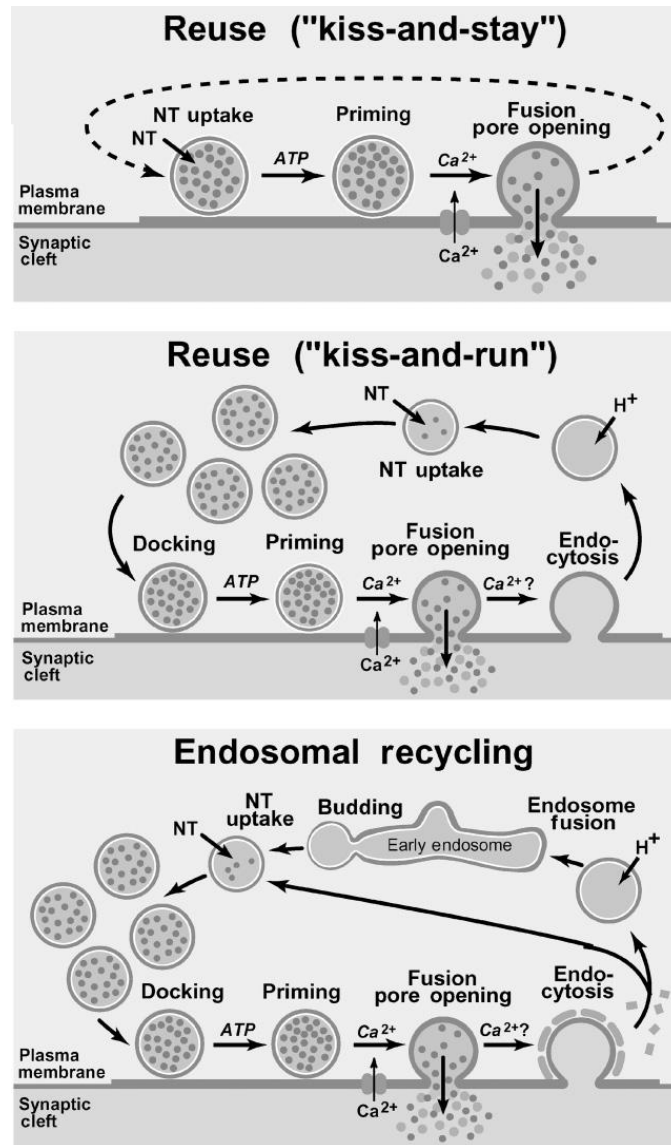


Figure 1-2. Three proposed pathways for synaptic vesicle endocytosis and recycling. First where the vesicle remains docked at the synaptic membrane surface during neurotransmission uptake. The second pathway the vesicle detaches from the membrane but remain localized near the active zone. Finally, vesicle formation during a clathrin dependent endocytosis after full fusion of vesicle with the membrane surface.⁵

to remain in the ready releasable pool. During kiss-and run, the empty synaptic vesicle releases from the membrane then reacidifies and refills with neurotransmitters while remaining localized near the active zone.^{5,10} The final pathway, clathrin-dependent endocytosis, occurs during the

recycling of synaptic vesicles that have fully fused with the synaptic membrane. Recycling of vesicles from the synaptic membrane is important to prevent the expansion of the presynaptic bouton membrane. Clathrin-dependent endocytosis involves the assembly of a complex structure, known as a coated pit, which concentrates surface proteins for internalization.¹¹ Vesicles resulting from clathrin-mediated endocytosis may bud directly from the synaptic membrane or during a bulk endocytosis from a large membrane infolding.¹² The resulting vesicles directly reacidify and refill with neurotransmitters or first pass through an endosomal intermediate.⁵ The entire SV cycle takes approximately 1 min to recycle synaptic vesicles for continued synaptic transmission.⁶

There are hundreds of billions of neurons in the in the central nervous system alone and each neuron forms thousands of synapses.¹³ In turn each of these synapses are independently regulated to effectively control neuronal cell to cell communication. It is important to develop sensitive quantitative techniques to elucidate the molecular events and physical properties of synaptic vesicles that regulate vesicle function in order to develop accurate and predictive models. Many current studies focus on bulk techniques to probe the physical properties of synaptic vesicles. This thesis will discuss the development and application of techniques for the analysis of synaptic vesicles on the single molecule/particle level which will be beneficial in future studies of these and other subcellular organelles. Chapter 2 will describe the spatial confinements of single particles/synaptic vesicles in aqueous droplets for the measurement of the diffusion coefficient and size in free solution. The development of a quantitative microscopy technique for quantifying proteins at the single vesicle level will be discussed in chapter 3 and 4.

Finally, chapter 5 will describe the steps towards loading nanoparticles into the lumen of synaptic vesicles in order to probe the intravesicular region.

1.2 Chapter References

- (1) Sudhof, T. C.; Jahn, R. *Neuron* **1991**, *6*, 665-677.
- (2) Zhang, Q.; Cao, Y.-Q.; Tsien, R. W. *Pro. Natl. Acad. Sci. U.S.A.* **2007**, *104*, 17843-17848.
- (3) Lisman, J. E.; Raghavachari, S.; Tsien, R. W. *Nat. Rev. Neurosci.* **2007**, *8*, 597-609.
- (4) Goda, Y.; Sudhof, T. C. *Curr. Opin. Cell Biol.* **1997**, *9*, 513-518.
- (5) Sudhof, T. C. *Annu. Rev. Neurosci.* **2004**, *27*, 509-547.
- (6) Sudhof, T. C. *Nature* **1995**, *375*, 645-653.
- (7) Stevens, C. F.; Tsujimoto, T. *Neurobiol.* **1995**, *92*, 846-849.
- (8) Rizzoli, S. O.; Betz, W. J. *Nat. Rev. Neurosci.* **2005**, *6*, 57-69.
- (9) Rosenmund, C.; Clements, J. D.; Westbrook, G. L. *Science* **1993**, *262*, 754-757.
- (10) Matthews, G. *Neuron* **2004**, *44*, 223-226.
- (11) Mousavi, S. A.; Malerod, L.; Berg, T.; Kjekken, R. *Biochem. J.* **2044**, *377*, 1-16.
- (12) Jung, N.; Haucke, V. *Traffic* **2007**, *8*, 1129-1136.

(13) Jahn, R.; Sudhof, T. C. *J. Neurochem.* **1993**, *61*, 12-21.

Chapter 2: Sizing Subcellular Organelles and Nanoparticles Confined within Aqueous Droplets

2.1 Introduction

Few methods exist currently to size single sub-diffraction-limited particles in free solution. Scanning probe microscopies (e.g., atomic force microscopy) and electron microscopies require immobilization of the particle on a surface or in a matrix. This requirement makes subsequent solution-phase analysis or transport difficult to perform. Light scattering measurements can size particles in solution but lack sufficient sensitivity to size single or a small group of particles and typically require high concentrations of particles for accurate measurement.¹ Correlation spectroscopy^{2,3} and particle tracking⁴ have the potential to size single particles in free solution, but currently it is difficult to achieve this feat because the particle can diffuse away from the interrogation region before its diffusion coefficient can be accurately measured, especially for small nanoparticles or macromolecules. To address this issue, this chapter describes the use of single aqueous droplets to spatially confine single or a small group of nanoparticles so their diffusion coefficient and size can be measured.

Droplet microfluidics has emerged in recent years as an attractive platform for conducting small-scale chemistries and for parallel assays.⁵⁻¹⁷ For example, we have developed techniques for the selective encapsulation of single subcellular organelles into a single femtoliter - picoliter volume droplet,⁷ methods for the transport and fusion of two droplets to initiate a chemical reaction,^{8,11} and single-molecule capillary electrophoresis techniques to separate and

detect the contents of single droplets.^{9,18} Here, we describe the use of aqueous droplets to confine the diffusion of single or a small group of nanoparticles so their diffusion coefficient and thus hydrodynamic size can be measured. We are particularly interested in the ability to size sub-diffraction-limited subcellular organelles prior to the analysis and quantification of their molecular contents.

This chapter describes two methods that offer complementary advantages for accurately measuring diameters of nanoscale particles in aqueous droplets. The first method is based on imaging and particle tracking,¹⁹⁻²² where the diffusive trajectories of a droplet-confined particle are first imaged, then analyzed to extract the diffusion coefficient and size. This method is easy to apply and can be adapted for the parallel tracking and measurement on particles confined in an array of droplets. The second method is based on confocal correlation spectroscopy (CCS)^{2,3} and fluorescence correlation spectroscopy (FCS),²³⁻²⁵ which are capable of accurately sizing both fluorescent and nonfluorescent particles in small sample volumes. FCS is particularly suited for measuring “dim” biological particles or ones that are easily photodamaged, because the confocal detection geometry illuminates only a small region of the droplet, and thus the particle is illuminated only for short periods of time (versus continuous excitation in particle tracking).

With either method, it is important to be aware of issues unique to confined volumes and droplets that may affect accurate diffusion measurements. We categorize these potential issues into two categories: ones that are hydrodynamic in origin and those that arise from interfacial/surface interactions. Once these variables are accounted for, it is a relatively simple process to size biological particles such as synaptic vesicles or polymer nanoparticles accurately in droplets. In combination with recent advancements in droplet microfluidics, we anticipate

these sizing techniques will offer new ways to probe single nanoparticles and biological molecules in solution.

2.2 Materials and Methods

2.2.1 Materials

AR20, AS4, Span 80, and poly(ethylene glycol) (av MW 8000 Da) were obtained from Sigma Aldrich (St. Louis, MO). Light mineral oil was purchased from Fischer Scientific (Hampton, NH). Sulfate-modified and amine-modified beads were 290nm and 200nm in diameter, respectively, and were acquired from Invitrogen Corporation (Carlsbad, CA).

2.2.2 Synaptic Vesicle Preparation

Synaptic vesicles were isolated from rat brains with a modified procedure from Hell et al.²⁶ Frozen rat brains (Pel-Freeze, Rogers, AR) were blended with liquid nitrogen until a fine powder formed and then suspended in 85 ml of homogenization buffer (2 mM EGTA, 50 mM HEPES, pH 7.2, 0.3 M sucrose). A Teflon-glass homogenizer was used to homogenize the solution. A synaptic vesicle rich supernatant was obtained by centrifuging the homogenate in an MLA-80 rotor (Beckman Coulter, Fullerton, CA) at 100 000g for 28 min at 4 °C. The supernatant was suspended on a 1.5 M/0.6 M sucrose step gradient before centrifuging at 250 000g for 72 min at 4°C. The isolated synaptic vesicles were collected from the 1.5 M/0.6 M sucrose interface then frozen and stored at -80°C for up to 4 months.

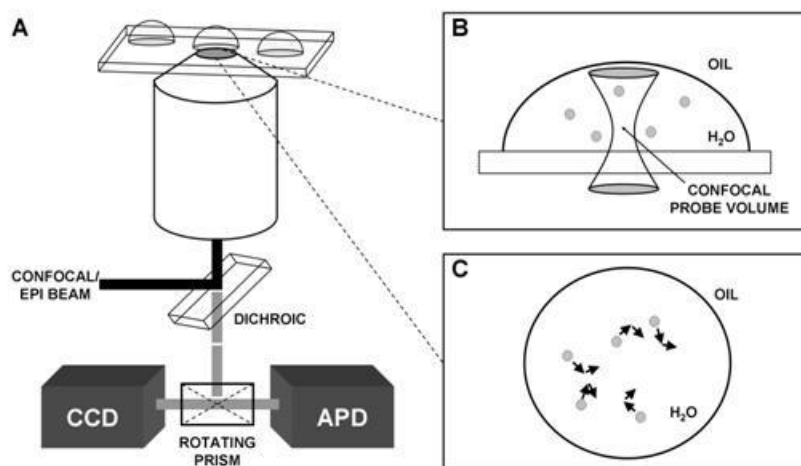


Figure 2-1. A) Schematic of the experimental setup used to excite and collect signals from particles encapsulated within microdroplets. B) With fluorescence correlation spectroscopy, which used point detection with an avalanche photodiode (APD), the confocal probe volume was placed at the center of the water droplet to detect burst events from the contained particles, thus measuring the diffusion time and size of the particles. C) For particle tracking, which used imaging with a sensitive CCD camera, each particle was tracked individually and the associated Δx and Δy values were recorded and used to calculate the diffusion time for each particle in the droplet.

2.2.3 Droplet Preparation

Droplets were generated by vigorously mixing 200 μL of a 10^{-10} – 10^{-12} M bead/synaptic vesicle aqueous solution with 800 μL of oil. The vigorous mixing provided a relatively heterogeneous population of droplet sizes and number of particles contained within. A pipet was used to transfer ~ 100 μL of oil/water mixture onto the glass substrate. After ~ 3 min, all of the droplets settled and adsorbed to the coverslip leaving a droplet container as shown in Figure 2-1 B. To measure the diffusion of particles, we searched the substrate to find a suitable droplet containing 1–5 particles for measurement. To minimize any hydrodynamic biasing due to the small size of

a droplet, droplets used for measurement were typically greater than $10\mu\text{m}$ in diameter. Furthermore, we focused at a plane near the middle of the droplet so that surface effects would also be minimized.

2.2.4 Experimental Setup for FCS and Particle Tracking

Excitation and collection of the fluorescence from particles encapsulated in droplets was performed on a Nikon TE2000 microscope using a high numerical aperture objective (NA 1.45). A laser emitting at 488nm (Coherent Sapphire, Santa Clara, CA) or 633nm (Coherent HeNe laser, Santa Clara, CA) was split into two independent beams and recombined to provide both confocal and epifluorescence illumination. Shutters were placed in front of either beam depending on which mode was being used. For confocal, the beam was expanded to fill the back aperture and collimated before being directed off a dichroic mirror (Chroma Tech. Corp., Rockingham, VT), which was designed to reflect both 488nm and 633nm into the objective. For epifluorescence, the beam was focused at the back aperture of the objective, so the beam exited at the object plane in a collimated form offering even illumination throughout the sample. Fluorescence from the encapsulated particles was collected using the same objective and filtered with the dichroic and band-pass filters (Chroma Tech. Corp., Rockingham, VT), which were specific whether 488nm or 633nm excitation light was employed, before the detectors to remove any excess laser radiation. A rotating prism, stock in the microscope assembly, was used to select the mode of imaging. For particle tracking, we used a highly sensitive CCD camera

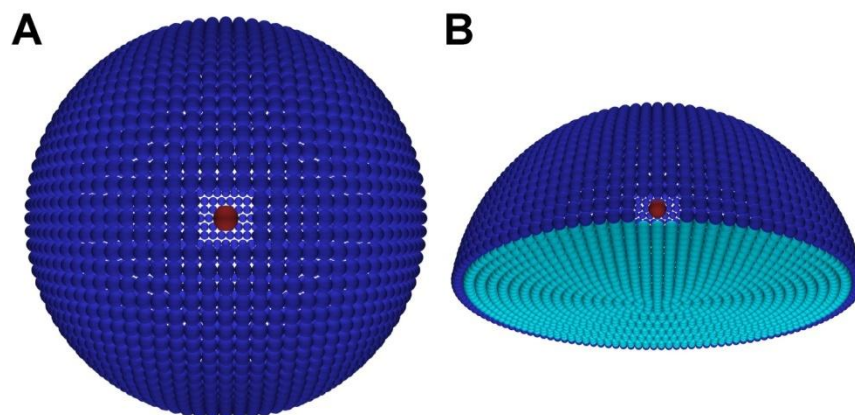


Figure 2-2. Two examples of the array of shell beads used to approximate the droplet wall for the diffusion-coefficient calculations. (A) $3\mu\text{m}$ diameter spherical droplet. (B) hemispherical droplet with a $4\mu\text{m}$ diameter base (viewed from underneath). For each shape and size of droplet, a series of calculations were performed using progressively more and smaller shell beads. For the two examples in the figure, the array of shell beads with the smallest size is shown and 9 of the shell beads have been removed to show a 200nm diameter red particle near the center of the droplet. The dark blue shell beads are positioned on a series of circles, which are located on the spherical portion of the droplet and separated by twice the radius of the shell beads. For the hemisphere, the shell beads used to fill in the base (shown in light blue) are located on a series of concentric circles where the spacing was chosen to allow the use of shell beads approximately equal in size to those on the spherical portion of the droplet. For the purposes of a friction-factor calculation, the open spaces between the shell beads are too small to allow a significant amount of leakage of the solution inside the droplet. This was confirmed by calculating the friction factor of the entire droplet (as opposed to the sphere inside the droplet). For the spherical droplets, where an analytical expression for the friction factor is available, the calculated friction factors for the array of shell beads agreed with the exact value of the friction factor to slightly better than 1%. This should be a reasonable estimate of any error introduced into the calculations due to the fact that we could not use infinitely small (and infinitely many) shell beads.

(Cascade 512B, Roper Scientific, Tuscon, AZ). For FCS, the fluorescence from the confocal probe volume was spatially filtered through a $50\text{-}\mu\text{m}$ pinhole and then focused onto an avalanche photodiode (AQR-14, Perkin-Elmer, CA), after which the signal was correlated using a Flex02-12D multiple-tau autocorrelator from correlator.com (Bridgewater, NJ). For particle tracking, the recorded trajectories were analyzed using the MetaMorph software from Molecular Devices (Sunnyvale, CA).

2.2.5 Simulations of Particle Diffusion in a Confined Volume

The calculation of the friction factor of a bead inside a spherical droplet has been discussed previously. Cunningham²⁷ derived an expression for the special case of a bead at the center of the droplet. Allison²⁸ performed calculations similar to what is performed here for a small bead (4nm diameter) inside a small spherical vesicle (100nm diameter) using well-established procedures.^{29,30} In this work, as in Allison's, the translational friction factor of a spherical bead inside a droplet is modeled by replacing the droplet interface by a rigid array of N spheres (shell beads) whose centers lie on the interface (Figure 2-2). Including the sphere for the bead inside yields a set of $N + 1$ spheres. The hydrodynamic properties of these spheres can be calculated using the procedures described by Garcia de la Torre and Bloomfield³⁰ and Allison.²⁸ In particular, it is possible to calculate the force necessary to maintain the bead inside at a constant velocity while the shell beads are stationary, and from that to obtain the average friction factor, f , for the bead inside the droplet. The diffusion factor of the bead, D , is related to the friction factor by

$$D = \frac{kT}{f} \quad (2-1)$$

where k is Boltzmann's constant and T is the temperature. In general the friction factor for a bead inside of a droplet will be larger than the unperturbed friction factor, f_0 , for the same particle in bulk solution. In bulk solution

$$f_0 = 3\pi\eta d \quad (2-2)$$

where η is the viscosity of the solution and d is the diameter of the spherical particle. In this work, the hydrodynamic interactions are modeled using the Rotne-Prager tensor³¹ for

nonoverlapping spheres of different sizes as was done by Allison.²⁸ Due to the increase in computing power since 1988, the approximations used by Allison to reduce the computer time required for the calculation were not necessary.

For each position of a bead inside a droplet, the calculation of the bead's friction factor is performed several times using successively more and smaller shell beads to model the droplet surface. For nearly all of the calculations, the friction factor converges in the sense that the difference between the values calculated using the smallest and next smallest shell bead sizes is less than 0.1%. For the smallest spherical droplet the differences were all less than 0.5%. In the results below, only the value calculated using the smallest sizes of shell beads to model the droplet interface are reported.

For each droplet it was necessary to calculate the coordinates of the N different shell beads used to model the droplet surface. For the spherical droplets, the center of a single shell bead is placed at each of the two points where the droplet surface intersects the z -axis. The coordinates of a series of circles on the surface of the droplet are then calculated. The circles are positioned so that the closest distance between adjacent circles and the distance between the intersection of the droplet with the z -axis and the circle closest to it are all identical. A radius for the shell beads is chosen that will fill in as much of the droplet surface as possible without allowing shell beads on adjacent circles to overlap. The coordinates of the shell beads, evenly spaced on each circle, are calculated and the entire set of coordinates constitutes the array of spheres used to represent the droplet wall. The size of the droplet and the number of circles determine the size of the shell bead used. The calculation was repeated with 11, 19, 29, 39, and 49 circles. The number of shell beads used to represent the droplet was 124, 502, 1129, 2016,

and 3153, respectively. Since the number of circles used is odd, one of the circles lies in the equator (xy -plane) of the droplet. The coordinates of one more sphere, which represents the particle inside the droplet, are added to the set of coordinates, which is then used to calculate the friction factor of the particle inside the spherical droplet.

For the hemispherical droplet, the procedure is similar to that for the spherical droplet. For the curved portion of the surface, the procedure is the same as for the spherical droplet, except that only those shell beads whose z -coordinate is greater than or equal to zero are used. The base is formed by the circle of shell beads in the xy -plane (corresponding to the equator of the spherical droplet), a shell bead placed at the center of the base, and a set of concentric circles. The spacing between the concentric circles is chosen to allow the use of shell beads whose size is as close as possible to the ones in the curved wall of the droplet while still filling in as much as possible of the hemisphere's base (Figure 2-2 B). The calculation was repeated using 5, 10, 15, 20, 25, 28, and 30 circles on the curved surface of the hemisphere. The corresponding numbers of concentric circles added to fill out the base of the hemispheres were 2, 5, 8, 10, 13, 16, and 18, respectively. The total number of shell beads was 92, 370, 831, 1483, 2322, 2925, and 3408, respectively. As before, these are the coordinates of the shell beads used to represent the droplet wall. One more sphere, used to represent the particle inside the droplet, is added to the set of coordinates, which is then used to calculate the friction factor of the particle inside the hemispherical droplet.

2.3 Results and Discussion

We have explored two complementary methods for measuring the diffusion times of nanoparticles confined in an aqueous droplet. The first method is to use single-particle tracking, and the second technique is based on CCS.^{2,3} Single-particle tracking works well with large (e.g., >100nm) and bright particles, because these particles diffuse slowly, which facilitates tracking, and are less prone to photobleaching or photodamage as they are continuously illuminated during tracking. The advantage of single-particle tracking is the ability to use imaging to sample most of the trajectories of the particle in the droplet as well as the ability to monitor many droplets simultaneously for parallel measurements. Single-particle tracking, however, tends to work less well with small particles (e.g., <100nm) that diffuse rapidly or fragile particles that are easily photodamaged. For these small and fragile particles, confocal or FCS is more suitable. In fact, rapid diffusion of small particles facilitates correlation measurements because of the higher rate of sampling of the trajectories of the particle per unit time. Furthermore, the sensitivity of confocal fluorescence measurements in free solution is orders of magnitude higher than epi-fluorescence imaging. We have demonstrated these two approaches to sizing particles using fluorescence measurements, owing to the widespread use of fluorescence labeling in biological samples, but these approaches may be extended to nonfluorescent particles, such as with the use of backscattering² or dark-field imaging for metallic particles.³²

2.3.1 Measuring Diffusion Coefficient in a Droplet with Single-Particle Tracking

During particle tracking, the probability of the displacement, $P(\Delta x)$, of a particle during Brownian motion is

$$P(\Delta x) = \frac{1}{\sqrt{2\pi\sigma^2}} e^{\frac{-\Delta x^2}{2\sigma^2}} \quad (2-3)$$

and

$$\sigma^2 = 2D\Delta t \quad (2-4)$$

where D is the diffusion coefficient and Δt is the time between frames. The displacement of a particle was determined using one of two tracking algorithms, template matching or threshold. Both algorithms identify the particle in the current image by comparing it to a preceding image, typically the initial frame of the video. The template-matching algorithm filters the current image using a convolution mask generated from the initial frame. An object is defined as the particle if the peak intensity in the current convolved image is greater than a minimum percentage of the peak intensity in the initial frame. The displacement, Δx and Δy , is the distance between the intensity maximum in the preceding convolved image and the intensity maximum in the current convolved image. This algorithm is ideal for particles where the centroid is best represented by the brightest pixel in the image. However, contamination, such as dust, causes image artifacts that can interfere with tracking when using this algorithm.

Alternatively, with the threshold algorithm a detected object is identified as the particle if the object's size is greater than a defined percentage of the total size of the particle in the initial frame. The displacement is then defined as the Δx and Δy from the center of the object in the preceding frame to the center of the object in the current frame. This threshold algorithm is not easily affected by contamination as is the template-matching algorithm. The major limitation to this algorithm is its inability to accurately determine the centroid of a particle that is not symmetric in appearance, but this limitation can be overcome. After experimental investigation

of both algorithms, we found the threshold algorithm to be the most applicable to our system due to its tolerance for dust particles or other imperfections in our images.

With either tracking algorithm, the Δx and Δy obtained were binned into histograms and the probability was fit with eq 3. We found the diffusion coefficient extracted from the probability-displacement curve is greatly affected by two factors: (1) the appearance of the particle in the image (particle symmetry), which affects the threshold tracking algorithm, and (2) the exposure time, frame rate, and lag time of the CCD camera used for imaging.

2.3.1.1 Particle-Image Symmetry

Over the exposure time, the particle is continually moving. As a result, for longer exposure times and faster diffusing particles, the image of the particle will represent the entire path taken by the particle during the exposure time instead of an instant representation of the position of the particle. The resulting image then becomes a nonresolved, asymmetric representation of the particle. This problem can be addressed by increasing the viscosity of the aqueous solution or by decreasing the exposure time. By increasing the viscosity with sucrose in our experiments, a reduced diffusion coefficient was observed. The reduced diffusion coefficient minimized blurring of the particle over the exposure time. This approach, however, increases the complexity of the experiment and can place undesirable constraints on the system under study. Decreasing the exposure time provided a sharper image and a better representation of the instant position of the particle in our experiments. There are, however, two considerations when implementing this approach: (1) to ensure sufficient displacement of the particle between successive frames, a delay time between frames is usually needed; and (2) the use of an overly

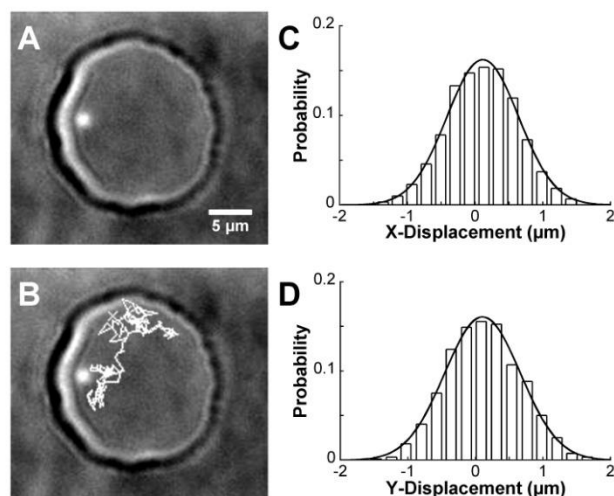


Figure 2-3. A) Single, 290nm-diameter fluorescent bead encapsulated within a hemispherical, water droplet ($\sim 20\mu\text{m}$ diameter). B) Particle tracking (gray lines) showed the diffusion path of the bead inside the droplet over 200 frames. For each displacement, the displacement corresponding to Δx (C) and Δy (D) were recorded, binned into histograms, and fit with equation 3 to determine the diffusion coefficient in each dimension. In this example, integration time for the camera was 100 msec, frame rate was 155 msec, and 800 images were acquired.

short exposure time will decrease the signal integration time of a given CCD pixel and, thus, the sensitivity of detection. Therefore, there is an optimal exposure time that both preserves detection sensitivity and minimizes blurring of the particle.

2.3.1.2 Exposure Time and Frame Rate

It has been shown that the measured diffusion of particles in a confined space will decrease as the exposure time increases.³³ An analytical expression relating the exposure time and frame rate to the apparent diffusion coefficient was presented by Montiel et al.⁴ It was shown that the true diffusion coefficient could be approximated with

$$\frac{D_{\text{app}}}{D} \approx 1 - \frac{1}{3} \left(\frac{T_{\text{exposure}}}{T_{\text{frame}}} \right) \quad (2-5)$$

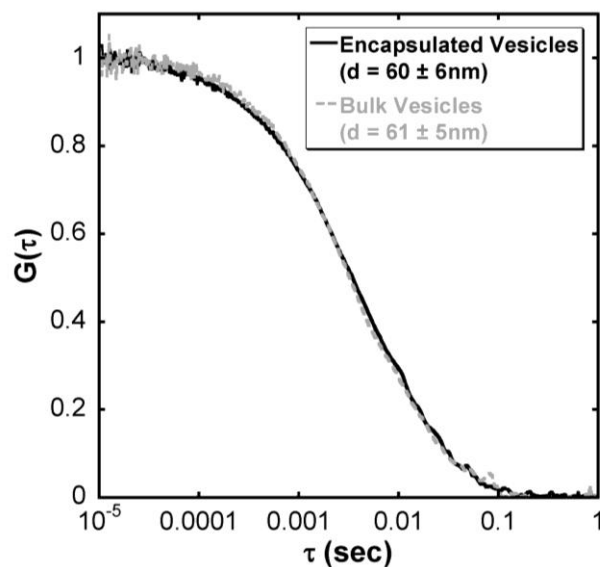


Figure 2-4. Normalized fluorescence correlation curves of synaptic vesicles encapsulated within a droplet (solid dark grey) and in the bulk solution (dashed light grey). Measured diameters of the synaptic vesicles in each sample agreed well within error (encapsulated, $d = 60 \pm 6\text{nm}$ and bulk, $d = 61 \pm 5\text{nm}$).

where D_{app} is the apparent diffusion coefficient, T_{exposure} is the exposure time, and T_{frame} is the frame rate. By taking the above factors into consideration, we have measured the diffusion coefficient and the particle size for single 290nm diameter (from manufacturer) beads confined in aqueous droplets (Figure 2-3); at 21°C with an exposure time of 100 ms, 155 ms frame rate, and 800 acquired frames, the average measured diffusion coefficient was $1.68 \pm 0.55 \mu\text{m}^2/\text{s}$. This corresponds to an average bead diameter of $\sim 272\text{nm}$ which compares well to the measured bulk diffusion coefficient of $1.69 \pm 0.22 \mu\text{m}^2/\text{s}$ at 22°C, which is equivalent to $\sim 279\text{nm}$ average diameter.

2.3.2 Accurate Sizing of Synaptic Vesicles in Droplets with Fluorescence Correlation Spectroscopy.

It has been hypothesized that the concentration of neurotransmitters contained within synaptic vesicles remains relatively constant and the sizes of synaptic vesicles vary depending on the number of contained neurotransmitters.³⁴ Therefore, we are particularly interested in the ability to size synaptic vesicles in free solution, followed by quantification of the neurotransmitter contents of the vesicles. Figure 2-4 shows the sizing of synaptic vesicles confined to an aqueous droplet with FCS; the measured size of synaptic vesicles in a droplet compares well with bulk measurements. A number of factors can affect the ability of FCS to accurately measure the size of nanoparticles,^{2,35-37} which we have described and analyzed in a previous publication.³ In this experiment, we first coated the glass surface with 1 mg/mL solution of dried milk, which contained mostly casein protein to prevent adsorption of the synaptic vesicles to the glass surface. The coating was highly hydrophilic and thus the water droplets wetted the surface much more than compared to unmodified glass substrate. The shape of the droplet then became much more pancake like instead of the hemispherical shape exhibited on the unmodified surface. This shape change, however, will not affect the diffusion coefficient of the synaptic vesicles within the droplet, as will be discussed later.

With the use of electron microscopy, the average diameter of synaptic vesicles is typically reported to be 40-50nm.³⁸ In free solution, however, few examples exist that describe the hydrodynamic radius of these organelles. With dynamic light scattering, the size of the synaptic vesicles is larger than that reported using electron microscopy and has been shown to be between 50 and 60nm in diameter.³⁹ Here, we recorded with FCS the size of the synaptic

vesicles in unconfined, bulk solution and found a similar diameter of 61 ± 5 nm. The recorded diameter from vesicles within the droplet is 60 ± 6 nm (Figure 2-4), which matches both the reported diameters from light scattering measurements and our FCS measurement on bulk samples. With the convenient incorporation of droplets into separations on chip,⁹ the ability to size single particles is an important step toward determining concentrations within nanometer-scale subcellular organelles.

2.3.3 Factors That Affect Accurate Sizing in Droplets

In comparison to bulk measurements in free solution, a number of factors unique to confined volumes can influence the ability to conduct accurate measurements of diffusion coefficients and sizing of nanoparticles. We divide these factors into two groups: those that are hydrodynamic in origin and those caused by interfacial/surface interactions.

2.3.3.1 Hydrodynamic Factors

The accurate sizing of particles in droplets requires accounting for the hydrodynamic interactions between the particle and droplet wall. The magnitude of the hydrodynamic interactions is a function of size of the particle and the droplet as well as the droplet's shape. As the particle moves inside the droplet, it creates a fluid flow field, or wake, around it. The fluid flow field transfers momentum between the moving particle and the stationary droplet wall which increases the friction factor of the particle above what it would have been if the particle was in a dilute bulk solution. To investigate this effect further, we performed calculations to investigate how

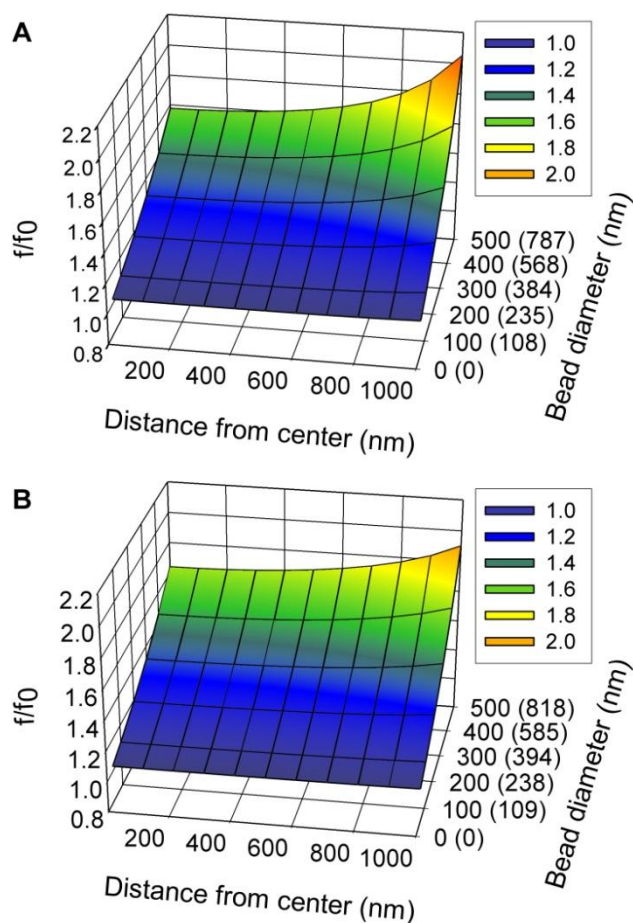


Figure 2-5. f/f_0 for a spherical bead inside of a droplet as a function of droplet shape, distance from the droplet center, and the actual and apparent bead diameters. The unparenthesized tic labels on the Bead diameter axis are the actual bead diameters. The numbers in parentheses are the apparent bead diameters which were calculated from the actual bead diameters using equation (6) and the value of f/f_0 at the center of the droplet. (A) f/f_0 for a bead inside of a $3\mu\text{m}$ -diameter spherical droplet. (B) f/f_0 for a bead inside of a hemispherical droplet whose base has a diameter of $4\mu\text{m}$. For the hemispherical droplet, the bead is always positioned $1\mu\text{m}$ above the hemisphere's base, and the distance is the horizontal distance to the symmetry axis of the droplet.

size and shape affected the measured diffusion coefficient of the particle within the droplet.

Figure 2-5 shows a comparison between spherical and hemispherical droplets by plotting the ratio f/f_0 , where f is the calculated friction factor and f_0 is the friction factor of the particle in bulk solution. The relationship between the actual diameter of the particle and the value measured in the droplet (the apparent diameter) is

$$\frac{f}{f_0} = \frac{d_{\text{apparent}}}{d_{\text{actual}}} \quad (2-6)$$

Figure 2-5 shows the ratio (f/f_0) as a function of position from the center of the droplet and particle size. Similar surfaces calculated for larger droplets showed that as the droplet size was increased, the f/f_0 surface flattened out and tended toward $f/f_0=1$ as the droplet became large. The magnitude of hydrodynamic interactions increases as the distance between objects in fluids decreases. Therefore, as expected, the ratio f/f_0 increases as the bead moves closer to the droplet wall. Furthermore, the effect of the hydrodynamic interactions increases as the size of the particle in the droplet increases. Both of these effects can be seen in Figure 2-5.

The apparent particle diameter is a weak function of the droplet's shape. For instance, the $3\mu\text{m}$ diameter spherical droplet in Figure 2-5 A has a volume which is approximately 15% smaller than the $4\mu\text{m}$ diameter hemispherical droplet in Figure 2-5 B. When the particle is close to the center of the droplet, the smallest distance from the particle's center to the droplet wall is $1\mu\text{m}$ for the hemisphere versus $1.5\mu\text{m}$ for the sphere. As expected, the f/f_0 ratio is slightly larger for the hemisphere, with the largest differences occurring for the largest particle (500nm diameter). The horizontal distance to the nearest droplet wall is larger in the hemisphere than the sphere, but this does not become a factor until the particle is more than 700nm away from the center. Beyond that point, the f/f_0 ratio is slightly larger (less than 7%) for the spherical droplet than the hemispherical droplet. A similarly modest shape dependence is observed when comparing the f/f_0 ratios in a $5\mu\text{m}$ spherical droplet with those in a $6\mu\text{m}$ hemispherical droplet. In this second case, the hemisphere is approximately 15% larger than the sphere, and the f/f_0 ratio in the hemisphere is always slightly larger (less than 6% for the 500nm particle, results not shown).

As a result, accurate modeling of the friction factor in a small droplet does not appear to require an extremely accurate description of the droplet's shape. Although any small errors introduced by an approximate description of the droplets shape would be systematic, they would be swamped by the random measurement errors. The results of the calculations show that for large droplets, such as the $20\mu\text{m}$ droplet in Figure 2, f/f_0 is nearly equal to 1 over a fairly substantial region of the droplet's interior. As a result, for such large droplets, any errors introduced into the analysis by ignoring the hydrodynamic interactions will be small compared to other experimental errors and can be ignored.

For smaller droplets, a figure similar to those in Figure 2-5 can be used to account for the effect of hydrodynamic interactions and to correct the experimentally determined particle diameter. The figure can be used to define a region within the droplet where f/f_0 is relatively constant to be used for particle tracking. For all of the displacements included in the analysis, f/f_0 is approximately equal to its value at the center of the droplet because the region where f/f_0 is least sensitive to position will include the center of the droplet. In Figure 2-5 the bead diameter axis is labeled both with the actual diameter of the particle for which the friction factor was calculated, but also (in parentheses) the apparent diameter, obtained by multiplying the actual diameter by the ratio f/f_0 . If the droplet is small enough that f/f_0 is not approximately equal to 1, then the diameter obtained by the particle tracking analysis is the apparent diameter. The appropriate value of f/f_0 can be obtained from the apparent diameter and the ratio can then be used to convert the apparent diameter into an actual diameter. So even for small droplets where the effect of the droplet wall on the particle diffusion is significant, it is possible to correct for the droplet size and shape and accurately size particles in small droplets.

Correcting for the effect of the droplet on the diffusion of a particle becomes easier as the droplet becomes larger. The magnitude of the effect becomes smaller, which means the required accuracy to which the shape and size of the droplet must be described is relaxed. Furthermore, the region over which the ratio f/f_0 is relatively constant becomes larger, which might allow for more of the particle's trajectory to be used. There is, however, one difficulty encountered with particle tracking as the droplet becomes larger, namely, that the particle will spend more time out of the plane of focus as the droplet becomes taller, which will reduce the amount of the particle's trajectory that is visible.

In the FCS measurement of the diffusion coefficient, the particle's fluorescence is measured as it crosses an approximately ellipsoidal volume defined by the focusing of the laser and the confocal pinhole in front of the detector. The effect of the droplet wall on the diffusion can be approximated by averaging the calculated f/f_0 ratio over a cylindrical volume which is $2.2\mu\text{m}$ tall and 490nm in diameter. This volume, which is the same size as the volume defined by the typical height and width of the probe volume in our FCS measurements,³ is aligned with the symmetry axis of the droplet and has its center at the center of the droplet. The results of this averaging for different sizes of droplets and particles are shown in Figure 2-6.

The results in Figure 2-6 are averages over the FCS volume, so the apparent diameter (as measured by FCS) can be directly converted to the actual diameter using Figure 2-6. Due to the height of the FCS probe volume, a somewhat larger dependence on droplet shape is observed in Figure 2-6, but only for the smallest droplet sizes. As the droplet become larger, the overall

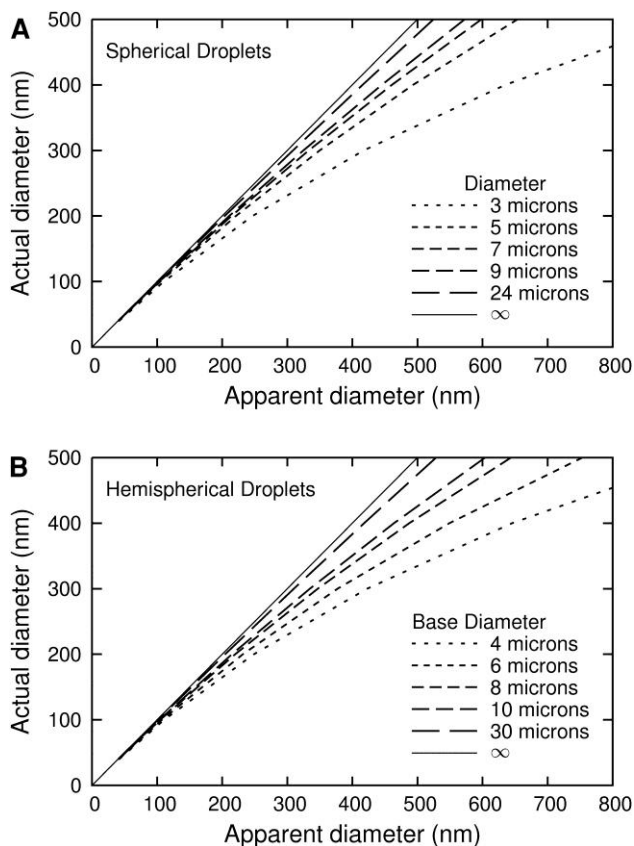


Figure 2-6. Actual diameter vs. Apparent diameter from FCS measurements for spherical particles in droplets. In both panels, the thin solid line is for equal actual and apparent FCS diameter (infinite size droplet). The relationship was calculated by averaging the ratio f/f_0 over a cylinder with a diameter of 490nm and a length of $2.2\mu\text{m}$, which is aligned with the symmetry axis of the droplet and whose center is at the center of the droplet. (A) Results for a spherical droplet. The five dashed lines represent the effect on the diameter as measured by FCS of (left to right) 24, 9, 7, 5 and $3\mu\text{m}$ -diameter spherical droplets. (B) Results for a hemispherical droplet. The five dashed lines represent the effect on the radius as measured by FCS of (left to right) 30, 10, 8, 6 and $4\mu\text{m}$ -diameter hemispherical droplet. For the $4\mu\text{m}$ hemisphere, f/f_0 is averaged over a cylinder with a diameter of 490nm and a length of $1.4\mu\text{m}$. The results for the $4\mu\text{m}$ hemisphere are presented only for comparison with the results for a $3\mu\text{m}$ spherical droplet, as its short height ($2\mu\text{m}$) would cause problems with an FCS experiment, which would have a sample volume exceeding $2\mu\text{m}$ in height.

effect of the droplet as well as the shape dependence becomes small. From Figure 2-6 it appears that once the droplet size is increased over $20\mu\text{m}$ in diameter, the effect of hydrodynamic interactions with the droplet wall has a very small effect on the measured friction factor of the

particle. It is also important to note that as the particle becomes smaller (e.g., <150nm), this hydrodynamic interaction becomes negligible, even for the smallest droplet (e.g., 3 μ m).

During our FCS measurements of the synaptic vesicles, the droplets were not the spherical or hemispherical shape we typically observe. Instead a pancake-shaped droplet is observed due to the hydrophilic surface used during the measurements. A model of a pancake droplet can be obtained from a model of a hemispherical droplet of the same height by expanding its base while keeping the height fixed. For any given location in the droplet, this increase in size results in an f/f_0 ratio which is closer to 1 for a pancake droplet than for a hemispherical droplet of the same height. Therefore, a shape change from a hemispherical to a pancake droplet of the same height will not affect the diffusion of a particle in regions where f/f_0 is already close to 1, as is the case for our measurements of synaptic vesicles encapsulated in a droplet.

2.3.3.2 Interfacial/Surface Interactions

In addition to hydrodynamic effects that depend on the size and shape of the aqueous droplet, there are other physical factors that can impact the measurements of the diffusion of particles in droplets. These factors include the surface charge of the particle, ionic/buffer strength of the solution, surface property of the glass substrate (if it were a hemispherical droplet), property of the immiscible phase, and whether any surfactants are used to coat the beads or the oil/water interface. We have studied the effects these factors can have on diffusion measurements in droplets; for example, a variety of oils (AS4 and AR20 silicone oil, and mineral oil), particles (sulfate-modified beads, amine-modified beads, and synaptic vesicles), aqueous solutions (DI water and phosphate-buffered saline), and surfactants (1 wt% Span 80 and 16 mg/mL PEG [MW

8000 Da] were examined while we developed a model system for sizing particles in droplets. In these experiments, we found it was important to prevent permanent absorption of the particles to the droplet interface or glass surface, but it was not critical to eliminate biasing of the particle's diffusion near such interfaces as long as only the particle's trajectories in the center of the droplet were used. We satisfied these criteria in FCS by "parking" the probe volume in the center of the droplet and in particle tracking by only using trajectories localized to the middle two-thirds of the droplet. Even if the particle eventually becomes attached to droplet interface/glass surface, we were still able to make accurate diffusion measurements if there was sufficient time (typically a few minutes) to record enough trajectories of the particle near the center of the droplet before the particle becomes irreversibly absorbed to the interface/surface.

2.4 Conclusion

We demonstrated here the ability of single-particle tracking and correlation spectroscopy to measure the diffusion coefficient and to determine the size of nanoparticles encapsulated within femtoliter to picoliter volume aqueous droplets. These two techniques are complementary. Particle tracking works best with bright particles that diffuse slowly, but has the advantage of imaging and can measure multiple single nanoparticles confined in multiple droplets in parallel. Correlation spectroscopy, such as FCS, is a point-detection technique, but it offers high sensitivity (e.g., diffusion coefficients of single dye molecules have been measured using FCS) and works best with small, dim, and rapidly diffusing particles. Currently, few techniques are capable of sizing single nanoparticles in free solution, and we anticipate our

approach to sizing single particles and molecules in droplets complements existing methods, such as light scattering, scanning probe methodologies, and electron microscopy imaging. We are particularly interested in combining this capability to size biological nanoscale objects and subcellular organelles with our droplet manipulation and analysis techniques for addressing a wide range of biological questions, such as the concentration of neurotransmitters contained within single synaptic vesicles or the level of metabolites and proteins contained in single mitochondria.

2.5 Chapter References

- (1) Pamme, N.; Koyama, R.; Manz, A. *Lab Chip* **2003**, *3*, 187-192.
- (2) Kuyper, C. L.; Budzinski, K. L.; Lorenz, R. M.; Chiu, D. T. *J. Am. Chem. Soc.* **2006**, *128*, 730-731.
- (3) Kuyper, C. L.; Fujimoto, B. S.; Zhao, Y.; Schiro, P. G.; Chiu, D. T. *J. Phys. Chem. B* **2006**, *110*, 24433-24441.
- (4) Montiel, D.; Cang, H.; Yang, H. *J. Phys. Chem. B* **2006**, *110*, 19763-19770.
- (5) Song, H.; Chen, D. L.; Ismagilov, R. F. *Angew. Chem., Int. Ed. Engl.* **2006**, *45*, 7336-7356.
- (6) He, M.; Sun, C.; Chiu, D. T. *Anal. Chem.* **2004**, *76*, 1222-1227.
- (7) He, M.; Edgar, J. S.; Jeffries, G. D.; Lorenz, R. M.; Shelby, J. P.; Chiu, D. T. *Anal. Chem.* **2005**, *77*, 1539-1544.
- (8) Lorenz, R. M.; Edgar, J. S.; Jeffries, G. D.; Chiu, D. T. *Anal. Chem.* **2006**, *78*, 6433-6439.

- (9) Edgar, J. S.; Pabbati, C. P.; Lorenz, R. M.; He, M.; Fiorini, G. S.; Chiu, D. T. *Anal. Chem.* **2006**, *78*, 6948-6954.
- (10) Tan, Y. C.; Hettiarachchi, K.; Siu, M.; Pan, Y. R.; Lee, A. P. *J. Am. Chem. Soc.* **2006**, *128*, 5656-5658.
- (11) Lorenz, R. M.; Edgar, J. S.; Jeffries, G. D.; Zhao, Y.; McGloin, D.; Chiu, D. T. *Anal. Chem.* **2007**, *79*, 224-228.
- (12) Jeffries, G. D.; Kuo, J. S.; Chiu, D. T. *Angew. Chem., Int. Ed. Engl.* **2007**, *46*, 1326-1328.
- (13) Rastogi, V.; Velev, O. D. *Biomicrofluidics* **2007**, *1*.
- (14) Li, L.; Boedicker, J. Q.; Ismagilov, R. F. *Anal. Chem.* **2007**, *79*, 2756-2761.
- (15) Sgro, A. E.; Allen, P. B.; Chiu, D. T. *Anal. Chem.* **2007**, *79*, 4845-4851.
- (16) Zhang, H.; Tumarkin, E.; Sullan, R. M. A.; Walker, G. C.; Kumacheva, E. *Macromol. Rapid Commun.* **2007**, *28*, 527-538.
- (17) Beer, N. R.; Hindson, B. J.; Wheeler, E. K.; Hall, S. B.; Rose, K. A.; Kennedy, I. M.; Colston, B. W. *Anal. Chem.* **2007**, *79*, 8471-8475.
- (18) Schiro, P. G.; Kuyper, C. L.; Chiu, D. T. *Electrophoresis* **2007**, *28*, 2430-2438.
- (19) Cheezum, M. K.; Walker, W. F.; Guilford, W. H. *Biophys. J.* **2001**, *81*, 2378-2388.
- (20) Goulian, M.; Simon, S. M. *Biophys. J.* **2000**, *79*, 2188-2198.
- (21) Moschakis, T.; Murray, B. S.; Dickinson, E. *Langmuir* **2006**, *22*, 4710-4719.
- (22) Chen, Y.; Lagerholm, B. C.; Yang, B.; Jacobson, K. *Methods* **2006**, *39*, 147-153.

- (23) Magde, D.; Elson, E.; Webb, W. W. *Phys. Rev. Lett.* **1972**, *29*, 705-708.
- (24) Saffarian, S.; Elson, E. L. *Biophys. J.* **2003**, *84*, 2030-2042.
- (25) Wohland, T.; Rigler, R.; Vogel, H. *Biophys. J.* **2001**, *80*, 2987-2999.
- (26) Hell, J. W.; Maycox, P. R.; Stadler, H.; Jahn, R. *EMBO J.* **1988**, *7*, 3023-3029.
- (27) Cunningham, E. *Proc. R. Soc. A* **1910**, *83*, 357-365.
- (28) Allison, S. A. *Biopolymers* **1988**, *27*, 97-111.
- (29) McCammon, J. A.; Deutch, J. M. *Biopolymers* **1976**, *15*, 1397-1408.
- (30) Garcia de la Torre, J. G.; Bloomfield, V. A. *Q. Rev. Biophys.* **1981**, *14*, 81-139.
- (31) Rotne, J.; Prager, S. *J. Chem. Phys.* **1969**, *50*, 4831-4837.
- (32) Xu, X. H.; Brownlow, W. J.; Kyriacou, S. V.; Wan, Q.; Viola, J. J. *Biochemistry* **2004**, *43*, 10400-10413.
- (33) Ritchie, K.; Shan, X. Y.; Kondo, J.; Iwasawa, K.; Fujiwara, T.; Kusumi, A. *Biophys. J.* **2005**, *88*, 2266-2277.
- (34) Colliver, T. L.; Pyott, S. J.; Achalabun, M.; Ewing, A. G. *J. Neurosci.* **2000**, *20*, 5276-5282.
- (35) Chiu, D. T.; Zare, R. N. *J. Am. Chem. Soc.* **1996**, *118*, 6512-6513.
- (36) Chirico, G.; Fumagalli, C.; Baldini, G. *J. Phys. Chem. B* **2002**, *106*, 2508-2519.
- (37) Osborne, M. A.; Balasubramanian, S.; Furey, W. S.; Klenerman, D. *J. Phys. Chem. B* **1998**, *102*, 3160-3167.

(38) Sudhof, T. C.; Jahn, R. *Neuron* **1991**, *6*, 665-677.

(39) Gracz, L. M.; Parsons, S. M. *Biochim. Biophys. Acta* **1996**, *1292*, 293-302.

Chapter 3: Synaptic Vesicle Protein Quantification at the Single Vesicle Level by Quantitative Microscopy

3.1 Introduction

Neurotransmitters are released at synapses via the fusion of transmitter-containing (synaptic) vesicles with the presynaptic plasma membrane. Formed during endocytosis, synaptic vesicles contain all the machinery they need to fill with neurotransmitter, associate with synaptic sites at the plasma membrane, and fuse in response to elevated calcium. Most of the protein constituents of synaptic vesicles have been identified and their contribution to vesicle functioning has been analyzed by genetic approaches. The copy number of the majority of vesicle proteins was recently estimated using biochemical approaches.¹⁻³

What is not known is the extent to which vesicles vary in protein composition and thus the consistency with which proteins are sorted to vesicles. Studies tracking the location of fluorescent vesicle proteins suggest that they freely exchange with excess protein on the plasma membrane.^{4,5} This exchange is consistent with the dynamic modulation of vesicle protein number in response to changing synaptic conditions. Indeed, functional differences consistent with variance in protein number have been reported,⁶ including differences in synaptic vesicle fusion within single synapses.^{7,8} Likewise, differences in endocytotic machinery suggest that protein content may vary between vesicles.⁹ In contrast, other studies support the conclusion that vesicles are either recycled intact,¹⁰⁻¹⁷ or that subsets of proteins remain clustered after

exocytosis.¹⁸ This suggests little change in vesicle protein composition and is consistent with protein interactions producing a precise protein stoichiometry in vesicles.

To address this question we developed an approach to quantify low-copy number proteins in isolated, single synaptic vesicles utilizing total internal reflection fluorescence (TIRF) microscopy. Proteins in isolated synaptic vesicles are labeled with fluorescent antibodies by incubating the vesicles with a primary antibody that targets the protein of interest and a fluorescent secondary antibody. Fluorescently labeled vesicles deposited on a glass surface are then imaged with TIRF microscopy. Images are processed to obtain a fluorescence intensity distribution. Proteins are counted from the average intensity and the variation in protein number is found by deconvolving¹⁹ the intensity distributions. A summary of the steps is provided in Figure 3-1.

Techniques currently available for quantifying protein number are limited to bulk approaches and single-molecule detection, which are either unable to provide information on the distribution around the average protein number or unable to count proteins present in the few to tens of copies. Bulk biochemical approaches, such as quantitative Western blot³, can only offer information about average values and not about the distribution of copy number. Fluorescence-based techniques that measure proteins present in high copy number (≥ 100) work by comparing the measured fluorescence intensity of biological samples to the average intensity estimated for a known number of proteins.^{20,21} These techniques can be applied to determine the distribution of protein copy number but it has been difficult to extend these methods to low-copy-number biomolecules, that is, those that range from a few to tens of copies. This is due to the fact that variability in the environment surrounding fluorophores can influence their measured intensity

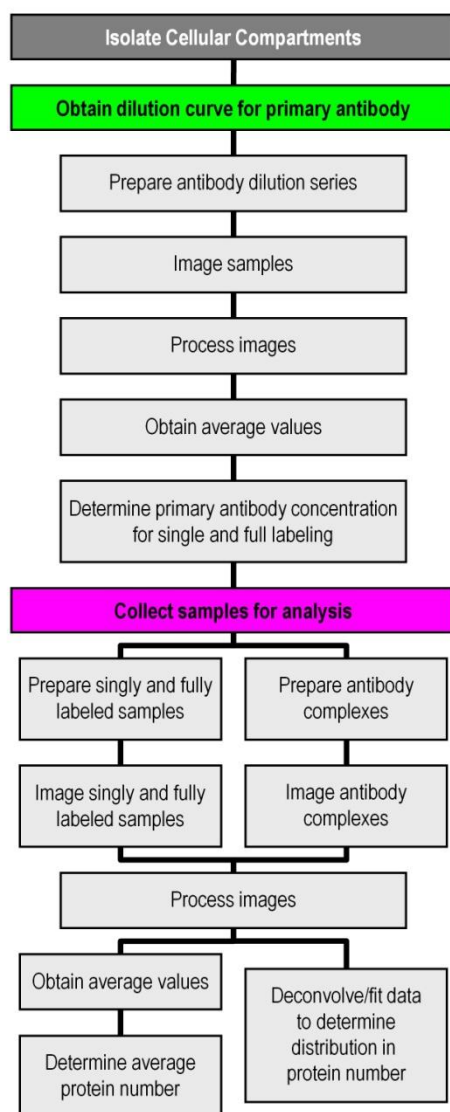


Figure 3-1. Flow chart outlining the analysis of isolated cellular compartments. A dilution curve is first carried out to determine limits for obtaining fully and singly labeled cellular compartments. Once the limits are determined, singly labeled and fully labeled samples are prepared and analyzed.

distribution, thus resulting in an observed intensity distribution that reflects more than just the distribution of copy number.¹⁹ Currently, these fluorescence-based techniques have been applied to samples with large copy numbers inside cells,^{20,21} in which case the variability in the environment has on the observed intensity is averaged out and does not affect the results.

However, for small copy numbers this is not necessarily true and the relationship between the width of the measured fluorescence intensity distribution and the width of the distribution of protein copy number is more complicated. If these techniques were to be applied to count smaller copy numbers without accounting for the fluorescence variability, the determined copy number distribution will be broader than the actual copy number distribution. The technique presented in this chapter takes into consideration the environmental effect on the fluorescence intensity distribution during the fitting process providing a more precise determination of the copy number distribution.

The potential for environmental effects also makes it difficult to use sequential single-molecule photobleaching to reliably count molecules that are present in more than a few copies.¹⁹ As the copy number increases, it becomes difficult to distinguish a step corresponding to bleaching of a single molecule because the potential for multiple molecules bleaching simultaneously increases. Though the technique discussed in this protocol can be applied to counting less than a few copies, it provides no advantage over sequential single-molecule photobleaching when less than a few copies of dyes are present. Also, application of this technique to large copy numbers (≥ 100) is unreasonable because an overwhelming number of data points would be needed to successfully apply the statistical analysis.

Beyond merely counting proteins at low-copy numbers, this technique can also assess the variability in the number of proteins, which provides insight into the regulation of cellular processes. An additional benefit of this technique is the ability to count the proteins *in situ* but this leads to the greatest limitation as well. Often a protein is found in complexes with other proteins potentially altering that protein's conformation and possibly hindering antibody binding.

In such cases as this, an absolute protein count may not be determined; however, observations relating to how distributions of protein number change can still be made. Changes to the apparent protein numbers caused by an environmental change can signify a change in the conformation/interaction state of that protein. Therefore, in such situations, this technique can still be a valuable tool for observing changes in the conformation of the protein complexes.

In this chapter, this method has been applied to count protein copy number in synaptic vesicles. However, this technique is suitable for counting proteins present in the few to tens of copies for most sub-cellular organelles or protein complexes. Procedures have been developed for the isolation and purification of many organelles and protein complexes,²² including immuno-isolation,^{23,24} sub-cellular fractionation,²⁵ and fluorescence-activated particle sorting.^{26,27} This approach is most applicable for sub-cellular organelles and protein complexes that can be imaged within the TIRF layer (~300nm), but alterations to the technique for use with epi-fluorescence would allow imaging of larger complexes. Additionally, instead of counting proteins via fluorescent antibodies, this method could be extended to counting endogenously labeled proteins in sub-cellular compartments. In such cases, photobleaching the endogenously labeled proteins to a single copy will provide the necessary intensity distribution for calibration (See Chapter 4).

Although it is possible to employ this technique to determine protein copy number in intact cells, there are several advantages to using isolated sub-cellular compartments rather than intact cells: (1) The use of isolated compartments circumvents problems with auto-fluorescence that often plague imaging in situ. Thus it provides a high signal-to-noise ratio. (2) The ability to concentrate the cellular compartment of interest means that one can obtain large data sets with a

limited number of images. (3) The use of isolated sub-cellular compartments facilitates antibody labeling, minimizing the potential for incomplete labeling. In addition, because we exogenously label protein, our technique avoids the potential for altered protein trafficking, which can occur when fluorescent proteins are expressed in cells.

3.2 Materials and Preparation of Synaptic Vesicle Samples

3.2.1 Antibodies

Agarose beads conjugated with goat anti-mouse (GAM), goat anti-rabbit (GAR), mouse IgG, or rabbit IgG were obtained from Sigma-Aldrich. Anti-synaptic vesicle protein 2 monoclonal antibody (SV2 mAb)²⁸ and anti-synaptotagmin polyclonal antibody (SYT pAb)²⁹ recognize epitopes in the cytoplasmic domains of these proteins. Anti-synaptophysin mAb (SYP mAb) and anti-VAMP2/synaptobrevin 2 mAb (VAMP2 mAb) were obtained from Lifespan Biosciences. The polyclonal antibody directed against the vesicular proton pump and SYG mAb (anti-synaptogyrin mAb) were obtained from Synaptic Systems. The monoclonal antibody directed against vesicular glutamate transporter 1 (Vglut1) was developed by and/or obtained from the University of California, Davis/National Institutes of Health NeuroMab Facility. SYT1 mAb was obtained from Millipore Bioscience Research Reagents/Millipore. Fluorescently labeled secondary antibodies (GAM Alexa-488, GAMAlexa-635, GAR Alexa-488, and GAR Alexa-635) were from Invitrogen/Invitrogen. Table 3-1 lists the combinations and concentrations of antibodies used.

Table 3-1. List of antibody dilutions used. Antigens marked with an asterisk were probed with a polyclonal antibody. All others were mouse monoclonal antibodies. Fluorescent secondary antibodies were used at a dilution of 1/1000.

Target Antigen	Antibody Dilution Used	Confirmatory Antigen
pan SV2	1/500	Synaptotagmin 1*
Synaptobrevin – VAMP2	1/250	SV2A*
Synaptogyrin 1	1/1000	SV2A*
synaptophysin – p38	1/250	SV2A*
Synaptotagmin 1 – p65	1/500	SV2A*
V-ATPase*	1/500	SV2A
VGlut 1	1/500	SV2A*

3.2.2 Isolation of vesicles from brain homogenates

Ten frozen Sprague Dawley rats, 7–8 weeks old, mixed gender brains (Pellfreeze) were pulverized into a fine powder by blending in liquid nitrogen. The powder was resuspended in 85 ml of homogenization buffer (0.3 M sucrose, 50mM HEPES, pH 7.4, 2 mM EGTA) and homogenized using a Teflon-glass homogenizer. The homogenate was centrifuged at 100 000g for 1 hr at 4°C. The resulting supernatant was loaded onto a 10 ml 0.6 M/1.5 M sucrose step gradient, then centrifuged at 260 000g for 2 hr at 4°C. Synaptic vesicles were collected from the interface of the 0.6 M/1.5 M sucrose steps. Isolated synaptic vesicles were diluted to 3 mg/ml as determined using a Bio-Rad protein assay kit with bovine serum albumin as a standard. Vesicles were frozen and stored at -80°C for up to 6 months.

3.2.3 Preparation of vesicles for fluorescence imaging

Synaptic vesicles were exchanged into PBS by gel filtration using a 3 ml BioGel P10 (Bio-Rad) column. Fifty micrograms of vesicle protein was incubated for 5 hr at 4°C with the antibody used for quantification (usually a monoclonal antibody). The sample was then incubated with anti-IgG-agarose (Sigma) to remove excess primary antibody. The supernatant containing

synaptic vesicles was transferred to a new tube and incubated overnight at 4°C with Alexa-488-conjugated secondary antibody (Invitrogen). Vesicles were then incubated with a second confirmatory antibody (all vesicles co-labeled with SV2 polyclonal Ab, except for SV2 primary labeled vesicles that were labeled with synaptotagmin polyclonal Ab, and the Vesicular Proton Pump primary labeled vesicles that were co-labeled with SV2 monoclonal Ab) and the corresponding Alexa-635-conjugated secondary antibody. We allowed a minimum of 1 hr at 4°C for each step. Synaptic vesicles were then incubated with anti-goat-IgG-agarose (Sigma) to remove excess secondary antibody from the solution.

3.3 Experimental Design and Equipment Setup

3.3.1 Design and fabrication of microfluidic chips

We used microchannels to deliver samples onto the surface of a coverslip for imaging using TIRF microscopy. We chose the microfluidic design depicted in Figure 3-2 A because it minimized the channel-to-channel variability in the measurement. The microfluidic channels were fabricated in poly (dimethylsiloxane) (PDMS) with rapid prototyping.³⁰ Briefly, our high-resolution mask was generated from a computer-aided drawing file and imprinted with the channel design. A high quality print of the master design was commercially printed (<http://www.fine-line-imaging.com/>). The mask was used in contact photolithography with SU-8 photoresist (MicroChem, Newton, MA) to create a positive relief pattern on a silicon wafer, which became our silicon master in subsequent steps of replica molding to form microchannels in PDMS. From the master, PDMS channels were molded and then sealed irreversibly to a

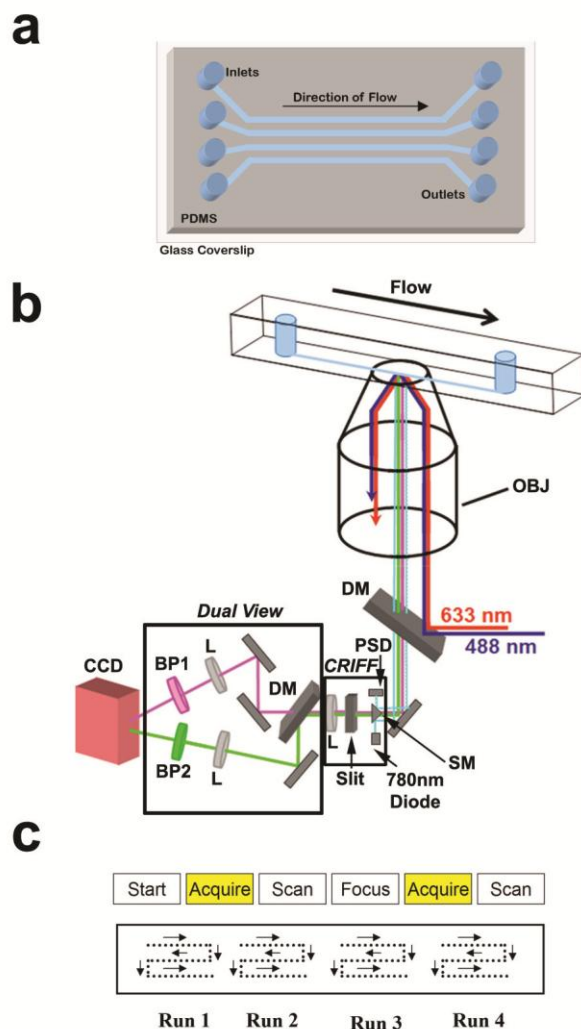


Figure 3-2. Imaging isolated cellular compartments. (a) We use a microfluidic chip fabricated in PDMS and sealed to a glass coverslip with four large ($800\ \mu\text{m}$ (w) \times $200\ \mu\text{m}$ (h) \times 2 cm (l)) channels to image samples. (b) Schematic showing the optical path for the TIRF microscope coupled with the CRIFF and dual view. Abbreviations: Lens (L), Dichroic Mirror (DM), Continuous Reflective-Interface Feedback Focus System (CRIFF), Charged Coupled Device (CCD), Position Sensitive Diode (PSD), Scanning Mirror (SM), Band Pass Filter (BP). (c) Diagram showing the scanning and acquisition pattern we used to collect images along the channel.

borosilicate glass coverslip by oxidizing the PDMS surface in oxygen plasma. We found that when the PDMS was sealed to a glass coverslip (described below) it causes a slight warping of the coverslip. Warping of the coverslip was minimized in the center of the chip, and therefore

the imaging environment of the sample was more uniform there. Also, it was essential that each channel has enough surface area ($800\ \mu\text{m} \times 200\ \mu\text{m} \times 2\ \text{cm}$, $w \times h \times l$) so that hundreds of images can be acquired in the same channel. Gravity driven flow was induced by placing $100\ \mu\text{L}$ of ultrapure water into the inlet reservoir within minutes of sealing. The use of microchannels to deliver samples for TIRF imaging was convenient because the samples non-specifically adsorb onto the surface of the coverslip as they flowed through the channel, thus the channel allowed for facile solution exchange and a controllable way to deposit samples to an acceptable confluence on the surface. It also offered an additional step of purification of the antibody labeled samples, as free antibodies only adhered to the glass surface in deionized water, but not in PBS buffer. As a result, only labeled samples were deposited onto the glass surface in the presence of buffer, which is important because we could not have any free-antibody intensities present in the intensity distribution of our fully labeled samples. When collecting a single antibody distribution, freshly collected ultrapure water was used to allow free antibodies to adhere to the surface of the glass.

3.3.2 Microscope Setup

The data in this chapter was collected using a total-internal-reflection-fluorescence (TIRF) microscope. Figure 3-2 B depicts a schematic of our optical setup, which was equipped with an objective-type TIRF, a continuous reflective-interface feedback focus system (CRIFF), a motorized stage, and a dual-view. The CRIFF automatically maintained the microscope focus as the sample was scanned and the dual view allowed simultaneous two color imaging. Our statistical analysis requires a high signal-to-noise ratio, low background fluorescence, and a way

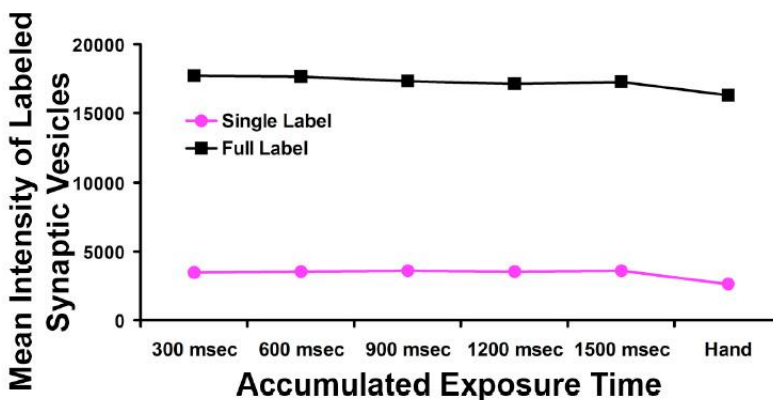


Figure 3-3. Photostability and photobleaching of synaptic vesicles. A fully labeled and a minimally labeled vesicle sample were exposed to the indicated durations of laser illumination before a final 300 msec exposure to acquire the image. We do not see measurable photobleaching even after exposing the vesicle samples to a duration that is 5 times longer (1500 msec) than the one we used (300 msec) in our actual experiments. We also test the effect of manually focusing the samples versus using the CRIF; the use of the CRIF is advantageous over manual focusing with slightly less photobleaching.

to collect reproducibly hundreds of two-color fluorescence images. The use of TIRF greatly reduced background fluorescence by illuminating only ~300 nm above the coverslip, thereby increasing the signal-to-noise ratio of the image.³¹ Simultaneously excitation with a 488nm light from a 20 mW solid-state laser (Coherent) and with a 633nm light from a 10 mW HeNe laser (Coherent) was done. The CRIF combined with a motorized stage allowed for the complete automation of focusing, scanning, and image acquisition along the channel.

Before image acquisition, the intensities of the lasers and the settings of the CCD were optimized to maximize the signal while maintaining the minimal amount of noise. Lasers were set at the minimum intensity needed to visualize 1-2 fluorescent antibodies. If the intensity was set too high, saturation of the CCD occurred or the fluorescent antibody photobleached during the exposure time resulting in the inability to successfully determine copy number. We found that the Alexa dye series antibodies provided optimum signal-to-noise over an exposure time of

300 msec even though there was minimal photobleaching over ~900 msec (Figure 3-3). Finally, the gain setting for the CCD was set so that signal from fully labeled synaptic vesicles fell in approximately the middle of the CCD range.

3.3.3 Image Acquisition

It was necessary to have hundreds to thousands of fluorescent spots for statistical analysis. The number of images needed was dependent on the concentration of spots in the imaging area. Using a motorized stage with a continuous focusing module to automate data collection greatly sped up this process. The timing of the stage movement was synchronized with the focusing of the CRIFF and the image acquisition. Figure 3-2 C shows a schematic of the method of data collection in order to optimally use the area of the microfluidic channel. Once an image was acquired the stage was translated a $200\mu\text{m}$ and the CRIFF adjusted the focus before another image was acquired. It was pertinent during the stage translation that each new imaging area was well outside of the width of the previously illuminated area. This avoided any possibility of imaging samples that may have been partially photobleached during the previous acquisition. This cycle was repeated until the desired number of images is collected.

3.3.4 Two-color labeling and selection of antibody

We developed a two-color labeling and imaging scheme where the synaptic vesicles were labeled with two different primary-secondary antibody pairs of two different colors (Figure 3-4). The first antibody pair targeted the protein of interest and the second antibody pair targeted a protein that is abundant on the synaptic vesicle but different from the protein of interest. Images

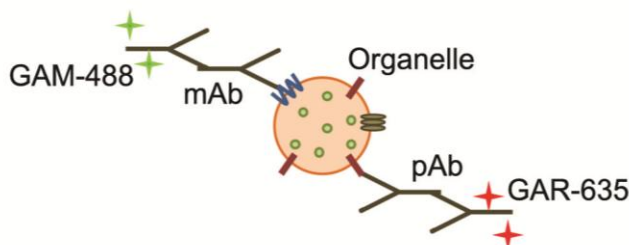


Figure 3-4. Antibody labeling of proteins of interest in cellular compartments. Two-color labeling of cellular compartments, which in this case are synaptic vesicles. The mAb labels the protein of interest while the pAb labels a protein that is highly abundant on the cellular compartment and serves as verification that the fluorescent spot is a cellular compartment. Abbreviations: monoclonal antibody (mAb), Alexa-488 goat anti-mouse antibody (GAM-488), polyclonal antibody (pAb), Alexa-635 goat anti-rabbit antibody.

were collected in both colors and the analysis compared the images for two-color overlay, and only spots with both colors co-localized were utilized in down-stream statistical analysis. Although two-color labeling may not be necessary in all situations, its use increased the robustness of the technique by ensuring that only labeled vesicles were studied.

For this technique to be accurate, the first primary antibody must label the protein of interest in a one-to-one fashion and must label all such proteins present on the synaptic vesicle. Therefore, we used monoclonal antibodies or peptide polyclonal antibodies that had been tested for specificity and which had a low dissociation constant (tight binding). To ensure tight binding, the labeled samples were checked for degradation (e.g. by monitoring changes in the average fluorescence intensity) over the course a few of days (Figure 3-3).

The second primary antibody was distinct from the first primary antibody in either type or in subclass to ensure that each primary antibody was labeled with a distinct fluorescent secondary antibody of a different color. This provided a distinction between labeled synaptic vesicles (two-colors) and excess unbound antibody (one-color) and ensured that only labeled

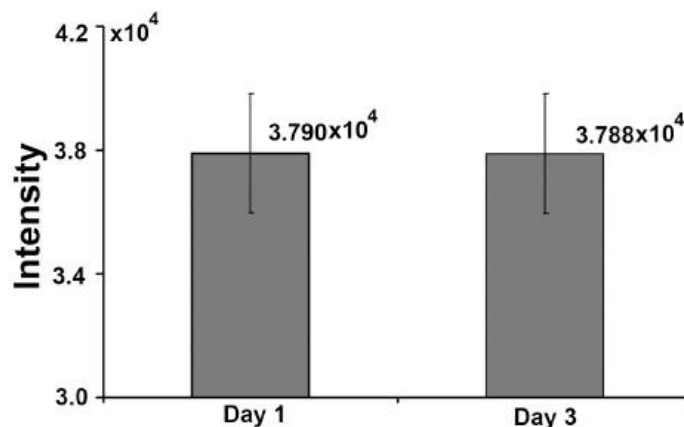


Figure 3-5. To determine whether antibodies remained attached to the vesicles during the course of our experiment, we tested the stability of our labeled vesicles over three days. We found the mean intensity obtained from single vesicles stayed constant over the course of three days. Since all studies were completed within the first day after vesicle labeling, sample degradation did not affect our results.

vesicles were studied. No quantification of the protein targeted by the second primary antibody was done; so, the second primary antibody did not need to label all of the targeted proteins on the cellular compartment.

Proper secondary antibodies to pair with each primary antibody were selected. Here, a highly cross-absorbed secondary antibody was used to minimize non-specific labeling. Samples of the synaptic vesicles were labeled with the secondary antibodies in the absence of the primary antibodies to verify that non-specific binding did not occur (Figure 3-6). The two different color fluorophores on the two antibodies had non-overlapping emission spectra and they were checked for photostability to ensure no bleaching occurred (Figure 3-3).

3.3.5 Determining antibody concentration and the average protein copy number.

Initially antibody dilution analyses using serial dilutions of the amount of the first primary antibody added to the synaptic vesicles in order to determine the concentration of antibodies that

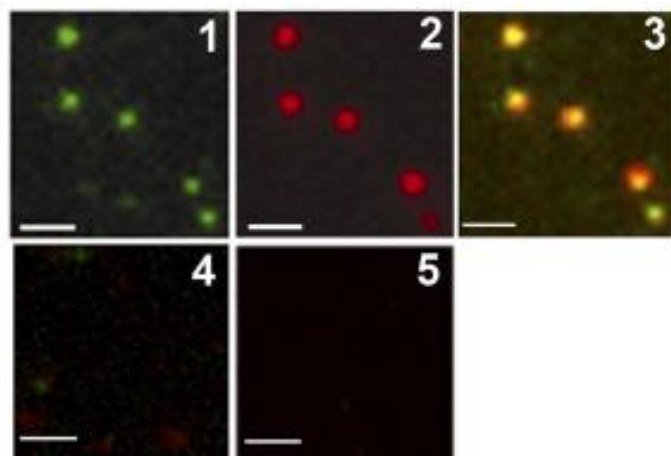


Figure 3-6. Verification of vesicle labeling. (1) Sample image of synaptic vesicles labeled with anti-SV2 and goat-anti-mouse-488. (2) Sample image of synaptic vesicles labeled with anti-synaptotagmin and goat-anti-rabbit Alexa 635. (3) Two-color overlay in which co-localization of the two probes appear yellow. (4) Sample in which primary antibodies were excluded from the labeling protocol. (5) Sample in which vesicles were excluded from the labeling protocol. Scale bars, 1 μm .

label to saturation the protein of interest on the vesicle, as well as establishing the antibody concentration where labeled vesicles only contain one primary antibody (most vesicles will not be labeled) were carried out (Figure 3-7). Saturated labeling was required to obtain information on the protein number on the cellular compartment, while minimally labeling vesicles were essential for generating calibration distributions used for deconvolution. The concentration of fluorescently labeled secondary antibody remained constant and any excess was removed. The average intensity per labeled synaptic vesicle was obtained by averaging the intensities of the labeled spots in the TIRF microscopy images. The synaptic vesicles were deemed fully labeled when the average intensity per labeled cellular compartment reached a stable high value (typically two consecutive high values), and singly labeled when the average intensity per labeled vesicle reached a stable low value (Figure 3-7). The concentration of antibody needed to create an appropriate dilution series was optimized for each protein quantified. Once the

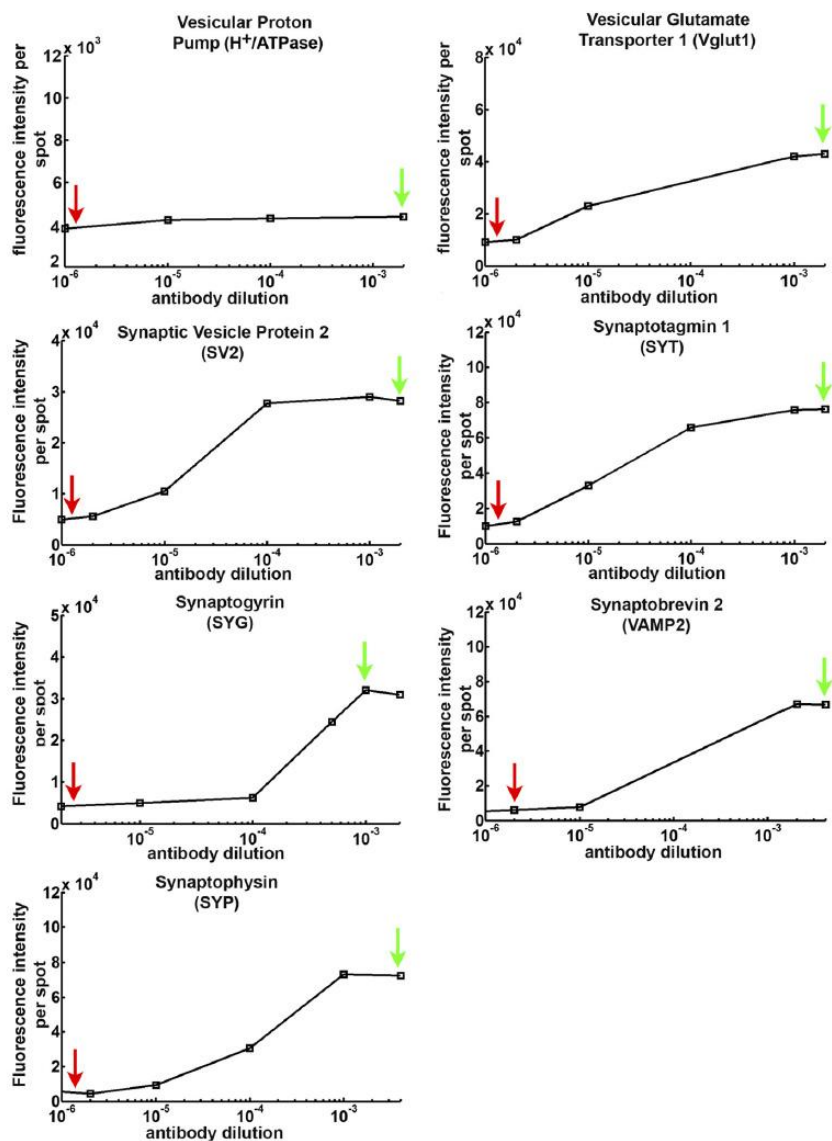


Figure 3-7. Determining the concentration of antibody required to produce fully and minimally labeled vesicles. Vesicles were labeled with the indicated antibody dilutions (from a stock concentration of ~ 2 mg/ml). Vesicles were judged to be fully labeled at antibody concentrations that produced no further increase in measured intensity per fluorescent spot (i.e., vesicle, green arrows), and to be minimally labeled at antibody concentrations that produced no further decrease in measured intensity per fluorescent spot (i.e., vesicle, red arrows).

antibody dilution analysis was finished, we used appropriate concentrations of antibody to prepare and analyze sets of synaptic vesicles for each protein quantified.

3.3.6 Image Analysis

A nearly fully automated analysis of the images was accomplished by development of an image processing program. We developed our image processing program in Matlab (Mathworks) utilizing the image processing toolbox available in Matlab. The following algorithm was used in our image processing program:

3.3.6.1 Estimate Background

The program read in the image and the coordinates of the regions of interest (ROIs) containing the fluorescent spots to be analyzed and estimated an approximate background (B_{apprx}) and standard deviation of the background (S_{apprx}) for that region. The values of B_{apprx} and S_{apprx} estimated here were not used in calculating the integrated intensities later. They were only used to identify regions of interest (ROIs) to be examined. Because the majority of the image was background, B_{apprx} was set to the 48th percentile of the pixel intensities, and S_{apprx} was set to half the difference between the 48th and 1st percentiles of the pixel intensities.

3.3.6.2 Identify ROIs

Used thresholds to identify ROIs to examine. For a given threshold, the program identified groups of connected pixels that were above the threshold and marked them as ROIs. Some of the spots may be so close together that they may not separate cleanly into two ROIs in the image if only a single, small threshold was used. To separate these, the thresholding was repeated several times, starting with a large value for the threshold and then repeating the process for successively

smaller thresholds. The rationale for this procedure was that the large thresholds increase the probability that fluorescent spots that are close together in the pixel will be identified as separate regions, while the small threshold defined the smallest-possible-intensity ROIs that the program will find. Typically, seven different thresholds were used, ranging from $60 \times S_{\text{apprx}} + B_{\text{apprx}}$ to $2.5 \times S_{\text{apprx}} + B_{\text{apprx}}$. This process created duplicate ROIs, since a pixel which has the peak intensity in a ROI for a large threshold will also be a pixel with the peak in a ROI for all smaller thresholds. The program removed these duplicate ROIs to create a set of distinct ROIs to examine.

3.3.6.3 Calculate Average Background

The background intensity for the image was calculated by dilating (expanding) all the ROIs by 12 pixels. Any pixel not in one of the dilated ROIs was considered to be part of the background and those pixels were used to calculate an average background (B) and standard deviation of the background (S) for that image. In our system, each pixel corresponded to a 160×160 nm region in the sample, so a band almost 2 microns wide (in the sample) around each ROI was excluded from the calculation of the background.

3.3.6.4 Preliminary checks of ROI

A ROI was considered unacceptable if the peak intensity exceeded 60000 (to avoid saturation of the CCD), if the area of the ROI before dilation exceeded 100 pixels (likely more than one vesicle in the ROI), or if the pixel of peak intensity was less than three pixels away from the edge

of the image (if the peak intensity pixel is too close to the edge, it is difficult to determine its width). ROIs whose peak intensity above the background (B) is less than $3 \times S$ were considered to be noise and were rejected.

3.3.6.5 Fit Each ROI to Obtain Width of the Fluorescent Spot

After subtracting B from the intensities of all the pixels in a particular ROI, the intensities were fit to a Gaussian. The background subtracted intensity of pixels in the ROI was fit to the equation

$$I(x, y) = A \exp\left(\frac{(x - x_0)^2 + (y - y_0)^2}{2\sigma^2}\right) \quad (3-1)$$

where the four adjustable parameters are x_0 and y_0 , the coordinates of the center of the Gaussian (which was allowed to be in fractions of a pixel), the width of the Gaussian (σ) and its amplitude (A). (Note that since the fit was to background subtracted intensities, no baseline was used in the fit). ROIs whose widths were larger than the width threshold were rejected since they likely contained multiple vesicles. The width threshold was typically ~ 2.3 pixels. A minimum width requirement of 1 pixel was also imposed on the ROI, since anything with a width that narrow is likely noise. ROIs that passed all of these tests were accepted, the remainder were rejected.

3.3.6.6 Image Focus Check

During the scanning, the CRIFF system did not always get the sample refocused before the image was taken. These images can be excluded automatically because either too few fluorescent spots can be identified, or in those cases where spots can be identified in an image,

they were out of focus (too broad). In this work, to pass the focus checks an image was required to have a minimum of 20 fluorescent spots and the average width of all spots (accepted and rejected) in an image had to be less than the measured diffraction limit of our setup (~2.3 pixels). For the singly labeled vesicles, there were typically so few spots per image that only the average width requirement was used.

3.3.6.7 Single-Antibody Images

After the focus check, the intensity distribution for the single antibodies was composed of the integrated intensities of accepted spots from images that passed the focus checks.

3.3.6.8 Vesicle Images (Two-Color Images)

For two-color imaging, a dichroic beam splitter was used to separate the green and red fluorescence from the sample and image them simultaneously onto two separate regions of the camera. The resulting image was divided into two sections, one for the green fluorescence and one for the red fluorescence, which corresponded to the same area in the sample. Each section was analyzed separately as described above, and lists of fluorescent spots and their coordinates for their peak intensity (x_0 and y_0 in equation 3-1) were made for both the green and red sections. Sometime, it was difficult to get both the green and red fluorescent images in perfect focus simultaneously (because of chromatic effects). Therefore, because quantification is performed using the green fluorescence, the green region of the image was focused while the width thresholds are greatly relaxed for the red ROIs. Furthermore, the focus check was only performed on the green region of the image. The coordinates of the green and red puncta were

compared and any green/red pair whose separation was less than the acceptance distance of ~ 2.3 pixels was considered to be matched. A red puncta is not permitted to be matched to more than one green puncta. If such a possibility arises, the red puncta was matched to the closest green puncta. The acceptance distance should not be set too small, since any offset in the alignment between the red and green sections might not be an integral number of pixels, and may involve a slight rotation of one section relative to the other. The intensity distribution of the two-color labeled synaptic vesicles was then composed of the integrated intensities of those green spots that were matched to red spots.

3.3.7 Data Analysis and Fitting of Fluorescence Intensity Distributions

The average number of proteins per vesicle was measured by dividing the average intensity value of the fully labeled vesicles by the average intensity value of singly labeled vesicles. The range in number of proteins per vesicle, in principle, can be found with a statistical analyses and deconvolution of the intensity distribution of the fully labeled and singly labeled samples. In practice, however, singly labeled samples typically provided < 1000 data points due to the extreme dilution needed to generate the sample. This number of data points was sufficient to determine an accurate average value, but not enough for our statistical analysis and deconvolution to obtain the distribution in copy number. A single primary-secondary antibody complex should be representative of a single labeled protein. We found that single primary-secondary antibody complexes provided thousands to tens of thousands of data points and the shape of the fluorescence intensity distribution is the same compared to the singly labeled sample; however, we found that the mean intensities differ between the two samples

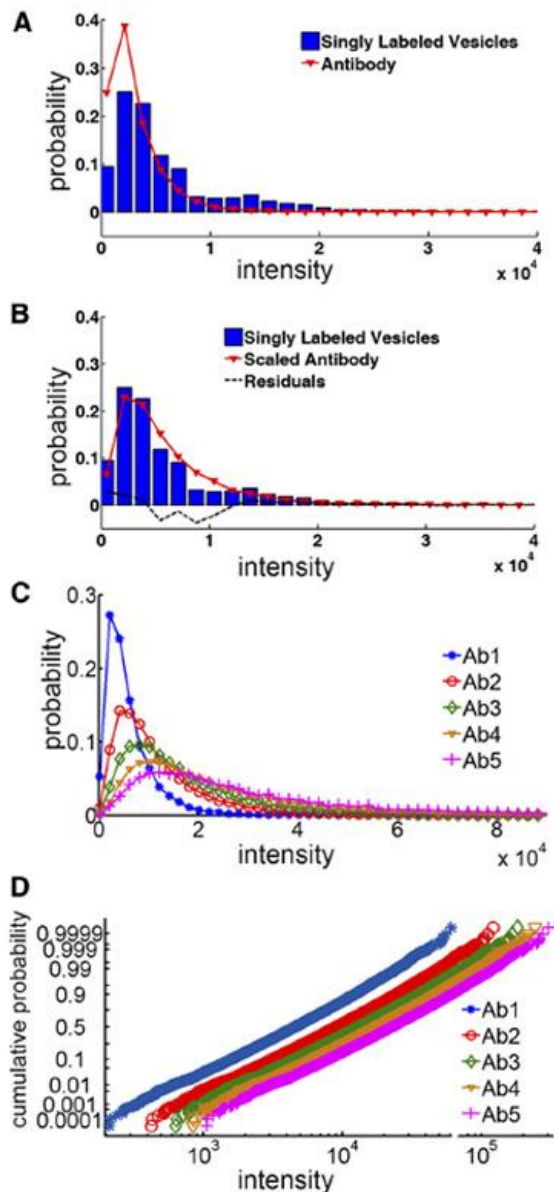


Figure 3-8. Procedure used to generate calibration distributions (A) Intensity distributions of single antibody complexes (red) compared with minimally labeled synaptic vesicles (blue). (B) Intensity distribution of single- antibody complexes after it has been scaled to the same mean intensity as the minimally labeled vesicles. The goodness of fit is indicated by a reduced χ^2 value of 1.10. The residual of the fit (the difference between the scaled antibody and the minimally labeled vesicles) is plotted as a black dotted line. (C) The scaled distribution of the single-antibody complexes was multiplied by integers to generate theoretical (calibration) distributions. Ab1 denotes the scaled distribution of the single-antibody complexes; Ab2 through Ab5 were obtained by multiplying the Ab1 distribution by the corresponding integers 2 through 5. (D) Calibration distributions displayed as semilog cumulative probability plots. This panel illustrates that multiplication of the calibration distribution does not change the multiplicative standard deviation or shape of the distribution.

(Figure 3-8 A). The difference in mean intensity was likely caused by the fact that single primary-secondary antibody complexes were directly in contact with the surface of the coverslip while the antibody on singly labeled synaptic vesicles often were not. To address these issues, we developed a procedure where we used the mean intensity obtained from the singly labeled samples to scale the single primary-secondary antibody distribution (Figure 3-8 B). Note that this scaling is possible and justified statistically because the shapes of the two distributions are the same.

Once we obtained the scaled single-antibody calibration distribution, we proceeded with the deconvolution of the fluorescence intensity distributions. For fitting the intensity distributions, the scaled single-antibody intensities were first multiplied by integer values (1 through x) to create theoretical distributions (calibration curves) for x number of antibodies attached to the synaptic vesicle (Figure 3-8 C and D). The best fit of a linear combination of the theoretical distributions to the measured intensity distribution of the fully labeled cellular compartments was obtained using least squares minimization. From the fit, we obtained both the average number and variation in the number of antibodies bound to the cellular compartments.

3.4 Results

3.4.1 Calculating the Average Number of Seven Membrane Proteins in Brain Synaptic Vesicles

We measured the average number of seven integral membrane proteins in rat brain synaptic vesicles: synaptophysin, synaptotagmin 1, SV2, VAMP2/synaptobrevin 2, Vglut1, synaptogyrin

1, and Voa of the proton ATPase.³² Integral membrane proteins are most amenable to this type of measurement, because, unlike extrinsic membrane proteins, the process of vesicle purification will not lead to changes in their association with vesicles. Each vesicle protein was independently measured at least three times in studies run in duplicate. In addition, VAMP2/synaptobrevin 2 was measured using two different antibodies. The average number of vesicle protein was determined by 2 methods: (1) by dividing the average intensity of fully labeled vesicles by the average intensity of singly labeled vesicles and (2) the average protein number found from the protein number distribution after deconvolving the intensity distributions of the fully labeled vesicles with the scale antibody-complex. The two approaches produced nearly identical values (± 0.1), with the exception of synaptophysin for which the fitting program produced an average value that differed by 1. The average number of the proteins varied from 1 to 13 (Table 3-2), suggesting that, on average, vesicles contain fewer than 20 copies of each of these proteins. In general the values agreed well (within a factor of 2) with those obtained by Takamori et al.,³ who used quantitative Western analyses calibrated to purified protein standards to quantify proteins in bulk preparations of synaptic vesicles. The exception was VAMP2/synaptobrevin 2, for which we obtained an average of 10 VAMP2 proteins per vesicle. This sevenfold lower value was obtained using two different monoclonal antibodies against VAMP2, suggesting that the measure was valid.

The lower average copy number of VAMP2/synaptobrevin 2 measured in intact versus solubilized vesicles could reflect the fact that a significant proportion of VAMP2/synaptobrevin 2 exists in protein complexes³³ and thus may not be accessible to antibody labeling. To test this possibility, we measured the ratio of VAMP2/SV2 in

Table 3-2. Average number of seven integral membrane proteins in synaptic vesicles. The average was determined by dividing the average total intensity of fully labeled vesicles by the average total intensity of minimally labeled vesicles for each sample. When the average was calculated using the fitting, the same values were obtained for all proteins except Synaptophysin for which the average was 14.0. The distribution width is the SD of each distribution averaged over all samples for each protein. The SE of the distribution width is the SEM for five separate measurements for VGlut1 and Synaptotagmin and six separate measurements for the remainder of the proteins. The coefficient of variation is the distribution width divided by the average protein number per vesicle.

Protein	Average number per vesicle	SEM	Samples analyzed	Total number of vesicles analyzed	Average number of vesicles per sample	Distribution width	SE of distribution width	Coefficient of variation for distribution
Proton ATPase	1.27	0.19	6	8826	1765	0.49	0.17	0.38
SV2	5.04	0.09	6	15,906	2651	0.23	0.21	0.057
VGlut1	4.09	0.12	5	20,989	4197	0.29	0.18	0.057
Synaptotagmin 1	7.16	0.07	5	9757	1951	0.86	0.08	0.12
Synaptogyrin 1	6.80	0.36	6	9026	1504	1.55	0.71	0.23
VAMP2	10.53	0.37	6	18,954	3159	5.13	0.84	0.49
Synaptophysin	13.06	0.83	6	10,462	1743	3.60	2.17	0.28

Table 3-3. Quantitative Western analyses of SV2 and VAMP2.

Protein	moles protein/ μ g synaptic vesicle	number of separate assays
SV2	30 ± 4 fmol	4
VAMP2 Synaptic Systems mAb	414 ± 80 fmol	7
VAMP2 Lifespan mAb	89 ± 12 fmol	4

immunoblots of solubilized, denatured vesicles. The amount of each protein was determined using recombinant protein standards run at the same time. Surprisingly, we found the results varied with the anti-VAMP2 antibody used, yielding VAMP2/SV2 ratios that ranged from 3:1 to 10:1 in the same vesicle preparations (Table 3-3). These results suggest that measures of the average number of VAMP2/ synaptobrevin 2 per vesicle may be imprecise. We note, however, that all measures indicate that VAMP2/synaptobrevin 2 is one of the more abundant vesicle proteins.

3.4.2 Variance in Vesicle Protein Number — How Accurately are Vesicle Proteins Sorted?

Factors that could influence the observed shape of calibration distributions and thus lead to spurious results include variability in the number of fluorophores per secondary antibody and variability in the number of secondary antibodies bound to each primary antibody. To address these possibilities, we compared the multiplicative standard deviation (σ^*), which reflects the shape of lognormal distributions,³⁴ between fluorescence intensity distributions obtained with labeled primary–secondary antibody complexes, isolated single secondary antibodies, and single fluorophores (as measured by sequential photobleaching; see Chapter 4). The resulting σ^* values and their SEs were 0.63 ± 0.05 for the antibody complexes, 0.61 ± 0.02 for the isolated secondary antibodies, and 0.62 ± 0.02 for the single fluorophores. The similarity in σ^* indicates that neither variation in fluorophore number per antibody nor in number of secondary antibodies per complex contributes significantly to the width of the intensity distributions. While the number of fluorophores per secondary antibody is presumably not identical, the results indicate that any variation therein has a small effect on our results. Therefore, multiplication of calibration distributions provides an adequate representation of the intensity distributions for $n > 1$ proteins per vesicle.

Fluorescence intensity distributions obtained from each sample of fully labeled vesicles were independently fit to calibration distributions and fitting results were averaged. Representative fits for each protein are shown in Figures 3-9 and 3-10. Data from at least five separate runs were averaged and depicted as histograms that plot the percentage of vesicles containing n number of each protein. We found that vesicle proteins fell into two classes, those

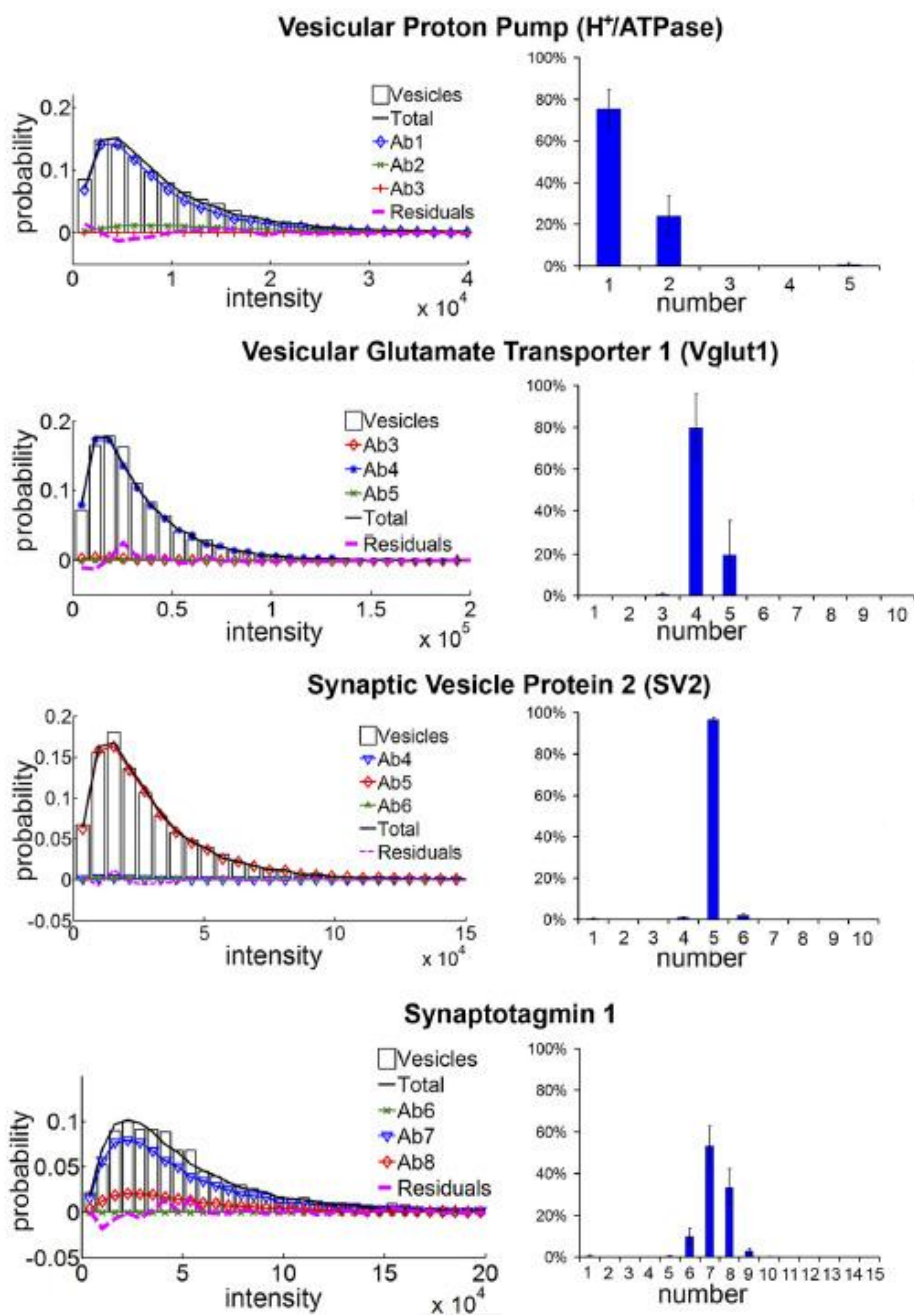


Figure 3-9. Quantification of monodispersed synaptic vesicle proteins. Plots of representative fits for each protein is shown on the left, and histograms showing the percentage of vesicles containing n number of the indicated vesicle protein averaged across $\sim 10,000 - 20,000$ vesicles (see Table 3-2) is shown on the right. Error bars, SE between different datasets.

whose intensity distributions were fit by three or fewer calibration distributions and those that required more than three calibration distributions to obtain a good fit. We term proteins for which fewer than three distributions describe $> 90\%$ of the vesicles as being “monodispersed” and those for which > 3 distributions are required to account for 90% of the vesicles as “polydispersed.”

An example of a monodispersed protein is SV2. For intensity distributions obtained from synaptic vesicles labeled with anti- SV2 the program was allowed 10 calibration distributions ($n = 1$ through $n = 10$) to fit the data. The vesicle data were fit best by a hybrid distribution that was $1\% n = 4$, $97\% n = 5$, and $2\% n = 6$. An example of a polydispersed protein is synaptogyrin. Distribution obtained from anti-synaptogyrin labeled vesicles required more than five calibration distributions to account for 95% of the distribution. In this case, the vesicle data were fit best by a hybrid distribution that was $11 \pm 8\% n = 5$, $29 \pm 10\% n = 6$, $30 \pm 8\% n = 7$, $7 \pm 4\% n = 8$, and $18 \pm 11\% n = 9$. Four of the seven proteins analyzed were relatively monodispersed (Figure 3-9). This included the proton ATPase for which $n = 1$ fit $75 \pm 9\%$ of the vesicle data, Vglut1 for which $n = 4$ fit $80 \pm 16\%$, and synaptotagmin 1 for which $n = 7$ and $n = 8$ fit $\sim 90\%$ of the vesicle data. The most monodispersed protein was SV2 for which on average $97 \pm 2\%$ of the vesicle data were fit by $n = 5$. We note that the low variability observed for these proteins is consistent with complete labeling by primary antibodies, because incomplete labeling would give rise to greater variability in apparent number. Thus it appears that a cohort of vesicle proteins varies little between vesicles.

Three of the seven vesicle proteins we analyzed were polydispersed: synaptogyrin, VAMP2/synaptobrevin 2, and synaptophysin (Figure 3-10). VAMP2/synaptobrevin 2 required

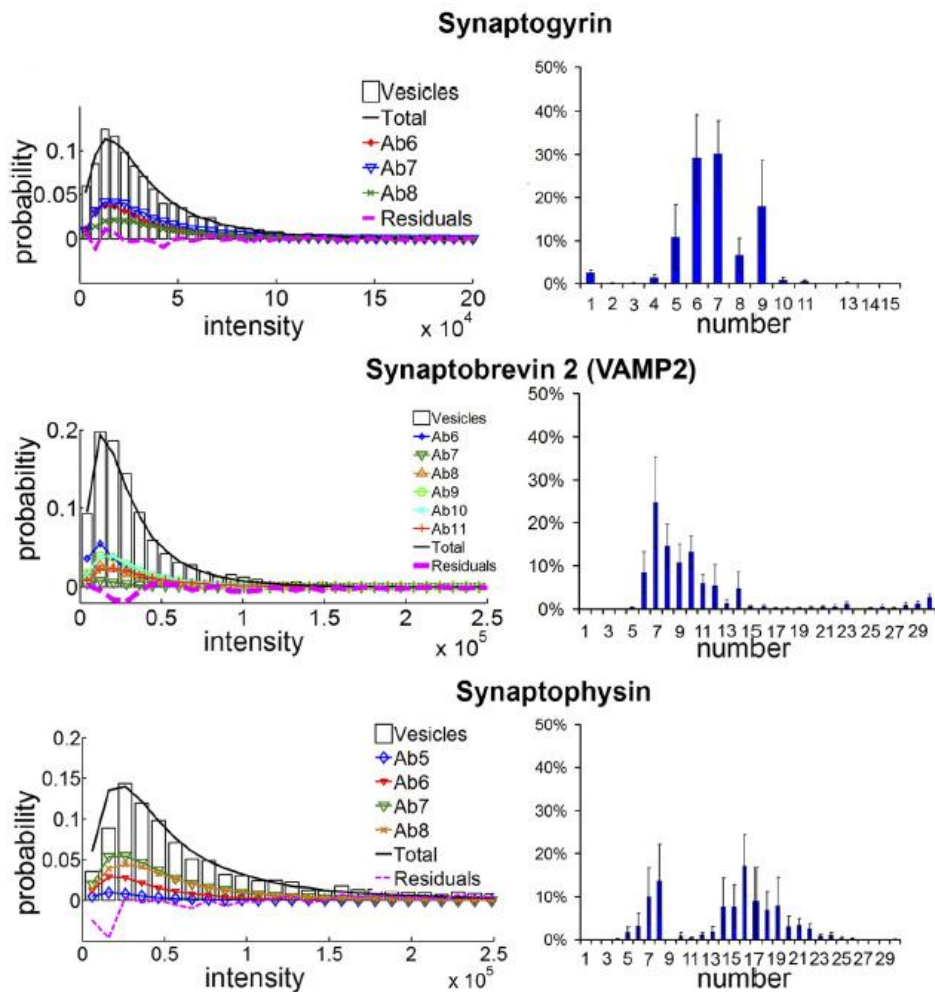


Figure 3-10. Quantification of polydispersed synaptic vesicle proteins. Plots of representative fits for each protein is shown on the left, and histograms showing the percentage of vesicles containing n number of the indicated vesicle protein averaged across ~10,000–20,000 vesicles (see Table 3-2) is shown on the right. Error bars, SE between different datasets.

> 9 calibration distributions to obtain the best fit ($8 \pm 5\%$ $n = 6$, $25 \pm 11\%$ $n = 7$, $15 \pm 5\%$ $n = 8$, $11 \pm 4\%$ $n = 9$, $13 \pm 4\%$ $n = 10$, and $6 \pm 2\%$ $n = 11$). Synaptogyrin required > 5 calibration distributions to obtain a good fit. Synaptophysin was the most polydispersed protein, requiring > 14 calibration distributions to obtain a good fit. We note that the bimodality of the combined data was not seen in individual experiments. This indicates greater variability between runs, which suggests that antigen accessibility was significantly more variable for synaptophysin than

for other proteins. The absolute monodispersity or polydispersity of proteins is reflected in the SD in protein number (Table 3-2). When viewed in this way, it becomes apparent that synaptophysin and VAMP2/synaptobrevin 2 are the most polydispersed of the vesicle proteins we measured. We note with interest that these two proteins are reported to form a complex *in vivo*.³³ This raises the possibility that the apparent variability in protein number measured for these proteins actually reflects changes in antibody accessibility because of variance in protein complex formation. Thus, for this subset of vesicle proteins, single vesicle quantification may measure a combination of number and conformation/interaction state.

To assess the possibility that proteins with smaller average numbers simply appear more monodisperse than proteins with larger average numbers because of the precision with which we can fit the distributions, we calculated the coefficient of variation for each of the protein distributions (Table 3-2). If the observed polydispersity for proteins with larger average numbers was primarily attributable to an increasing difficulty in fitting their distributions, we would expect that using the coefficient of variation would eliminate most of the differences between different proteins. This is not observed. Based on the coefficient of variation, the three most monodispersed proteins are VGlut 1, SV2, and SYT. This indicates that monodispersity is not masked when proteins are present in higher numbers.

3.5 Discussion

3.5.1 Quantitative Single Vesicle Imaging Provides Information on the Variance in Vesicle Composition

A major advantage of quantifying native protein in isolated vesicles is that it provides information on the distribution of protein number, and with it information on the consistency of vesicle assembly. Thus the approach we describe provides a way to measure disruptions in protein sorting that may accompany neuropathological conditions. Changes in vesicle protein expression have been noted in several nervous system pathologies, including schizophrenia,³⁵ epilepsy,³⁶⁻³⁸ and Alzheimer's disease, where changes in vesicle protein expression precede loss of synapses and changes in cognitive functioning.^{39,40} The technique described here will provide a means for identifying changes in the precision of protein sorting in animal models of disease and with changes in protein expression.

3.5.2 Functional Implications of Vesicle Protein Number and Variability

The number and variability of each protein in synaptic vesicles has implications for hypotheses of protein action at the synapse. Four of the seven proteins analyzed, SV2, H⁺/ATPase, Vglut1, and synaptotagmin, varied little in number of copies per vesicles. This was seen despite the fact that the vesicles analyzed represented all neurotransmitter classes. This finding supports a model in which protein complexes with a fixed stoichiometry interact with clathrin adaptor proteins in a stereotypical manner. In this way, vesicle protein content could be encoded into protein interactions that result in the self-assembly of vesicles with uniform protein content. This model is consistent with the report that SV2, the most monodispersed of the vesicle proteins, regulates the amount of synaptotagmin in synaptic vesicles.⁴¹

Our finding that the glutamate transporter Vglut1 is relatively monodispersed suggests that variation in the number of transporters per vesicle is not common. Thus the observation that variation in transporter expression alters the amount of neurotransmitter packaged into vesicles^{42,43} is not likely to be a widespread source of regulation *in vivo*.

Because we analyzed vesicles of all transmitter classes, we cannot tell whether polydispersity reflects variability across all vesicle classes or arises from the relative abundance of vesicle classes with different, monodispersed numbers of these proteins. Therefore, one exciting possibility is that polydispersity reflects variability between neurotransmitter classes of vesicles, and that this underlies differences in release probability across different classes of synapses.

Although the tetraspan proteins synaptophysin and synaptogyrin are both polydispersed, they differed significantly in their average number per vesicle (6.8 ± 0.36 for synaptogyrin and 13.06 ± 0.83 for synaptophysin). Because loss of both synaptophysin and synaptogyrin is required to observe deficits in synaptic functioning,⁴⁴ it has been assumed that they provide a redundant function. The discrepancy in their average number suggests that this may not be true and that these proteins may perform unique actions in vesicles.

In summary, knowing the number and variance of vesicle proteins provides a basis for vetting models of exocytosis and endocytosis and screening alterations in vesicle composition in animal models of neurological disorders. We anticipate that this approach will find wide use in future studies of synaptic regulation.

3.6 Chapter References

- (1) Morciano, M.; Burre, J.; Corvey, C.; Karas, M.; Zimmermann, H.; Volkandt, W. *J. Neurochem.* **2005**, *95*, 1732-1745.
- (2) Burre, J.; Beckhaus, T.; Schaeffer, H.; Corvey, C.; Hofmann, S.; Karas, M.; Zimmermann, H.; Volkandt, W. *Proteomics* **2006**, *6*, 6250-6262.
- (3) Takamori, S.; Holt, M.; Stenius, K.; Lemke, E. A.; Gronborg, M.; Riedel, D.; Urlaub, H.; Schenck, S.; Bruegger, B.; Ringler, P.; Mueller, S. A.; Rammner, B.; Graeter, F.; Hub, J. S.; De, G. B. L.; Mieskes, G.; Moriyama, Y.; Klingauf, J.; Grubmueller, H.; Heuser, J.; Wieland, F.; Jahn, R. *Cell (Cambridge, MA, U. S.)* **2006**, *127*, 831-846.
- (4) Fernandez-Alfonso, T.; Kwan, R.; Ryan, T. A. *Neuron* **2006**, *51*, 179-186.
- (5) Wienisch, M.; Klingauf, J. *Nat. Neurosci.* **2006**, *9*, 1019-1027.
- (6) Gracz, L. M.; Wang, W. C.; Parsons, S. M. *Biochemistry* **1988**, *27*, 5268-5274.
- (7) Trommershauser, J.; Schneggenburger, R.; Zippelius, A.; Neher, E. *Biophys. J.* **2003**, *84*, 1563-1579.
- (8) Muller, M.; Goutman, J. D.; Kochubey, O.; Schneggenburger, R. *J. Neurosci.* **2010**, *30*, 2007-2016.
- (9) Hayashi, M.; Raimondi, A.; O'Toole, E.; Paradise, S.; Collesi, C.; Cremona, O.; Ferguson, S. M.; De, C. P. *Proc. Natl. Acad. Sci. U. S. A.* **2008**, *105*, 2175-2180.
- (10) Ceccarelli, B.; Hurlbut, W. P.; Mauro, A. *J. Cell Biol.* **1973**, *57*, 499-524.
- (11) Murthy, V. N.; Stevens, C. F. *Nature* **1998**, *392*, 497-501.

- (12) Ales, E.; Tabares, L.; Poyato, J. M.; Valero, V.; Lindau, M.; De, T. G. A. *Nat. Cell Biol.* **1999**, *1*, 40-44.
- (13) Klyachko, V. A.; Jackson, M. B. *Nature (London, U. K.)* **2002**, *418*, 89-92.
- (14) Aravanis, A. M.; Pyle, J. L.; Tsien, R. W. *Nature* **2003**, *423*, 643-647.
- (15) Richards, D. A.; Bai, J.; Chapman, E. R. *J. Cell Biol.* **2005**, *168*, 929-939.
- (16) Wu, W.; Xu, J.; Wu, X.-S.; Wu, L.-G. *J. Neurosci.* **2005**, *25*, 11676-11683.
- (17) He, L.; Wu, L.-G. *Trends Neurosci.* **2007**, *30*, 447-455.
- (18) Willig, K. I.; Rizzoli, S. O.; Westphal, V.; Jahn, R.; Hell, S. W. *Nature (London, U. K.)* **2006**, *440*, 935-939.
- (19) Mutch, S. A.; Fujimoto, B. S.; Kuyper, C. L.; Kuo, J. S.; Bajjalieh, S. M.; Chiu, D. T. *Biophys. J.* **2007**, *92*, 2926-2943.
- (20) Wu, J. Q.; Pollard, T. D. *Science* **2005**, *310*, 310-314.
- (21) Sugiyama, Y.; Kawabata, I.; Sobue, K.; Okabe, S. *Nat. Methods* **2005**, *2*, 677-684.
- (22) Pasquali, C.; Fialka, I.; Huber, L. A. *J. Chromatogr. B* **1999**, *722*, 89-102.
- (23) Howell, K. E.; Gruenberg, J.; Ito, A.; Palade, G. E. *Prog. Clin. Biol. Res.* **1988**, *270*, 77-90.
- (24) Burger, P. M.; Mehl, E.; Cameron, P. L.; Maycox, P. R.; Baumert, M.; Lottspeich, F.; De Camilli, P.; Jahn, R. *Neuron* **1989**, *3*, 715-720.
- (25) Hell, J. W.; Maycox, P. R.; Stadler, H.; Jahn, R. *EMBO J.* **1988**, *7*, 3023-3029.

- (26) Bock, G.; Steinlein, P.; Huber, L. A. *Tr. Cell Biol.* **1997**, *7*, 499-503.
- (27) Gauthier, D. J.; Sobota, J. A.; Ferraro, F.; Mains, R. E.; Lazure, C. *Proteomics* **2008**, *8*, 3848-3861.
- (28) Buckley, K.; Kelly, R. B. *J. Cell Biol.* **1985**, *100*, 1284-1294.
- (29) Schivell, A. E.; Batchelor, R. H.; Bajjalieh, S. M. *J. Biol. Chem.* **1996**, *271*, 27770-27775.
- (30) Fiorini, G. S.; Chiu, D. T. *Biotechniques* **2005**, *38*, 429-446.
- (31) Axelrod, D. *Methods Cell. Biol.* **1989**, *30*, 245-270.
- (32) Jahn, R.; Suedhof, T. C. *Annu. Rev. Neurosci.* **1994**, *17*, 219-246.
- (33) Calakos, N.; Scheller, R. H. *J. Biol. Chem.* **1994**, *269*, 24534-24537.
- (34) Limpert, E.; Stahel, W. A.; Abbt, M. *BioScience* **2001**, *51*, 341-352.
- (35) Mirnics, K.; Middleton, F. A.; Marquez, A.; Lewis, D. A.; Levitt, P. *Neuron* **2000**, *28*, 53-67.
- (36) Matveeva, E. A.; Whiteheart, S. W.; Slevin, J. T. *J. Neurochem.* **2003**, *84*, 621-624.
- (37) Matveeva, E. A.; Vanaman, T. C.; Whiteheart, S. W.; Slevin, J. T. *Epilepsy Res.* **2007**, *73*, 266-274.
- (38) Matveeva, E. A.; Vanaman, T. C.; Whiteheart, S. W.; Slevin, J. T. *Epilepsia* **2008**, *49*, 1749-1758.
- (39) Yao, P. J.; Zhu, M.; Pyun, E. I.; Brooks, A. I.; Therianos, S.; Meyers, V. E.; Coleman, P. D. *Neurobiol. Dis.* **2003**, *12*, 97-109.

- (40) Yao, P. J. *Trends Neurosci.* **2004**, *27*, 24-29.
- (41) Yao, J.; Nowack, A.; Kensel-Hammes, P.; Gardner, R. G.; Bajjalieh, S. M. *J. Neurosci.* **2010**, *30*, 5569-5578.
- (42) Wojcik, S. M.; Rhee, J. S.; Herzog, E.; Sigler, A.; Jahn, R.; Takamori, S.; Brose, N.; Rosenmund, C. *Proc. Natl. Acad. Sci. U. S. A.* **2004**, *101*, 7158-7163.
- (43) Daniels, R. W.; Collins, C. A.; Chen, K.; Gelfand, M. V.; Featherstone, D. E.; DiAntonio, A. *Neuron* **2006**, *49*, 11-16.
- (44) Thiele, C.; Hannah, M. J.; Fahrenholz, F.; Huttner, W. B. *Nat. Cell Biol.* **2000**, *2*, 42-49.

Chapter 4: Single-Molecule Fluorescence Quantification with a Photobleached Internal Standard

4.1 Introduction

Often bio-analytical studies employ fluorescent probes, such as dyes or fluorescent proteins, to observe and quantify bio-molecules that are essential to cellular function and physiological processes. The photophysical properties, like emission intensity, of fluorophores can be affected by a variety of environmental factors such as solvent polarity,^{1,2} pH,³⁻⁵ or temperature.^{6,7} To further the understanding of cellular dynamics, studies have employed environmentally sensitive fluorophores as biosensors within cellular systems. For instance, measurements of the acidification kinetics within the lumen of individual synaptic vesicles have been studied in synaptobrevin (spH) vesicles which are synaptic vesicles that have been modified to express pH sensitive green fluorescent proteins (GFPs) on the luminal portion of the synaptobrevin 2 (VAMP 2) proteins.⁴

In our efforts to aid the development of an accurate and predictive model of cellular function, we developed a sensitive quantitative microscopy technique to determine the average number of proteins within sub-cellular compartments and to provide a distribution of the protein number over the entire population.⁸⁻¹⁰ To accurately quantify the protein number, it is essential to obtain an intensity distribution that is representative of a single fluorescent entity that is being used for quantification. However, the environment that some fluorophores are in, such as the GFP in spH vesicles, is not entirely known and it is difficult to generate a calibration sample that

accurately represents a single fluorophore. In cases like this any differences in environmental factors between the calibration sample and the sample of interest could alter the count, especially in a sensitive single-molecule technique. To overcome this potential drawback, we demonstrate how photobleaching can be used to obtain an intensity distribution representative of a single fluorophore directly from the sample of interest while maintaining the original environment. To demonstrate the counting capability of this technique we counted the number of Alexa Fluor 488, an environmentally insensitive fluorophore, on goat-anti mouse IgG antibodies and the number of GFP, an environmentally sensitive fluorophore, in spH vesicles.

4.2 Materials and Methods

4.2.1 Materials

All chemicals were purchased from Sigma-Aldrich unless noted otherwise. Goat anti-mouse Alexa-488 (GAM-488) was obtained from Invitrogen.

4.2.2 SynaptopHluorin Vesicle Isolation

Whole brains were extracted from transgenic mice at 20-25 days old then frozen and stored at -80°C before use. SynaptopHluorin (spH) vesicles were isolated using a modified procedure from Hell *et. al.* as discussed in previous work. Briefly, 5-10 frozen brains were blended with liquid nitrogen to a fine powder. The fine powder was re-suspended with homogenization buffer (2mM EGTA, 0.3M sucrose, 50mM HEPES, pH 7.4) and then homogenized with a Teflon-glass homogenizer. A spH vesicle rich supernatant was acquired by centrifuging the homogenate at

100,000 g for 28 min at 4°C with a MLA-80 rotor (Beckman Coulter, Fullerton, CA) in a Beckman-Coulter tabletop ultracentrifuge. The supernatant was loaded onto a 1.5 M/0.6 M sucrose gradient and centrifuged at 250,000 g for 72 min at 4°C to isolate the spH vesicles. Isolated spH vesicles were extracted from the 1.5 M/0.6 M sucrose interface then frozen and stored at -80°C for up to 4 months. Before imaging, spH vesicles were exchanged into fresh phosphate buffered saline (PBS) using a P10 size exclusion column (Bio-Rad).

4.2.3 Sample Imaging and Photobleaching

Total internal reflection fluorescence (TIRF) microscopy was used to simultaneously image and photobleach the sample. For ease of imaging, an imaging chip consisting of 4-straight channels 1mm-wide and 300µm-high were fabricated in polydimethylsiloxane (PDMS) and sealed irreversible to a borosilicate glass coverslip as previously discussed.¹⁰ The sample was introduced to an imaging channel through gravity driven flow and allowed to adsorb to the glass surface before flowing through clean PBS buffer to remove excess, non-adsorbed sample. Using a home-built TIRF microscope the sample was continually illuminated for 5 min to ensure complete photobleaching with a 488nm light from a 20 mW solid-state laser (Coherent). A stream acquisition of images was acquired with a Photon-Max EMCCD camera (Princeton Instruments) with an exposure time of 300 msec per image. We used a 100×, NA 1.45 Nikon objective and each 16 micron pixel of the EMCCD corresponds to 160nm in the sample.

4.2.4 Extraction of Initial and Final Intensity Distributions

The fluorescent images were analyzed with an image-processing program generated in Matlab.^{9,10} Briefly, the program applies a series of thresholds to identify the fluorescent puncta to be analyzed within each image. Potential puncta that can be attributed to noise or sample aggregates are eliminated through a series of tests. The amplitude of the puncta must exceed a signal-to-noise cutoff and their width must not be significantly larger than the resolution of the microscope system. The exact values of these thresholds are adjustable parameters. Finally, the integrated intensities of acceptable puncta are used to generate an intensity distribution ($\{F\}$). In order to quantify the fluorophores in the sample, initially the image-processing program was applied to the first image of the photobleaching series to identify all acceptable puncta and generate an initial intensity distribution ($\{F_i\}$). The image processing program was then used on all the images in the photobleaching series with all the criteria thresholds set to ensure that no potential puncta were rejected prematurely due to things such as a decrease in signal-to-noise during bleaching.

A second program was used to extract the final fluorescent intensities (F_f) corresponding to a single fluorophore in the sample from photobleaching tracks (Fig. 1) for each punctum found in the first frame. The program generates photobleaching tracks for each punctum by comparing the centroid of the initial punctum to those found within the subsequent images. If a punctum is found with a centroid within a designated acceptance distance (d_{ac}), the track is assumed to be continuing. Once a punctum is no longer observed for a specified number of consecutive frames (frame cutoff, n_{co}) the photobleaching track is terminated and F_f is outputted. The program requires a designated number of blinks (n_b) (Figure 4-1 B) to occur during the photobleaching

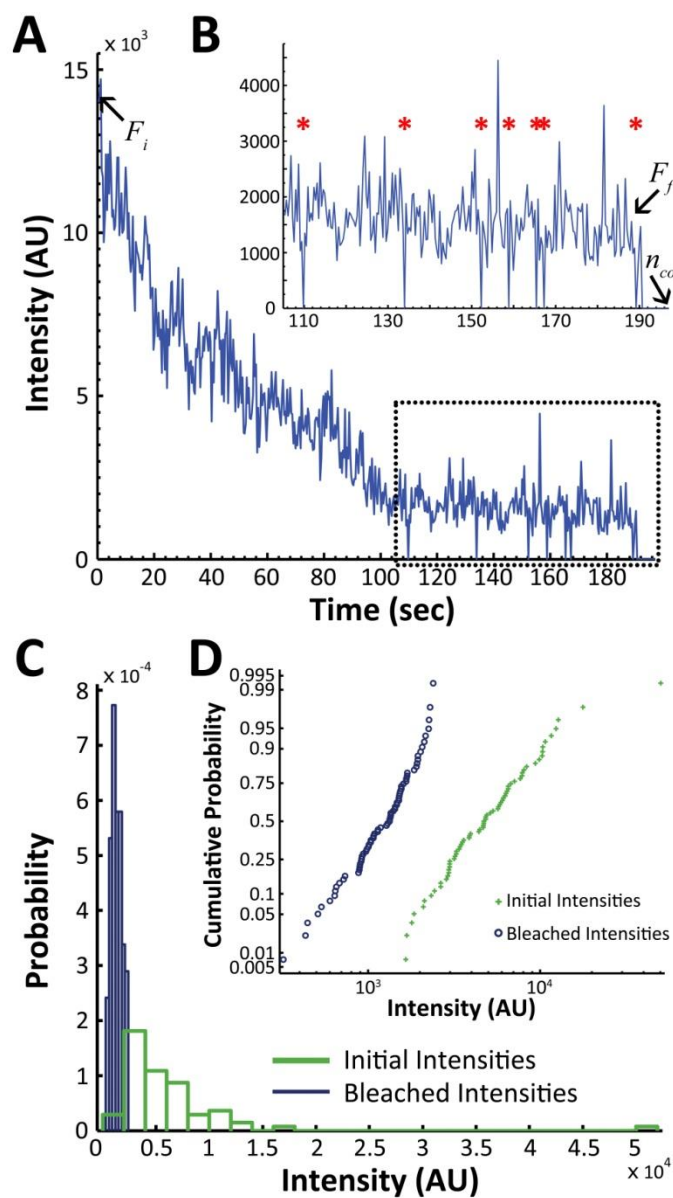


Figure 4-1. (A) Photobleaching track of GFP in a single synaptotHluorin vesicle. The initial intensity, F_i , is from the first frame of the photobleaching track. (B) Photobleaching track tail enlargement. Blinks are denoted by (*). The photobleaching track is terminated after the vesicle is no longer observed for a designated number of frames ($n_{co} = 10$ frames). Once the track is terminated, the final intensity, F_f , is extracted from the photobleaching track. (C) Initial and final intensity distributions ($\{F_i\}$ and $\{F_f\}$) for all acceptable vesicles in a single photobleaching series. (D) Semi-log cumulative probability plots of $\{F_i\}$ and $\{F_f\}$ showing the conservation of the distribution shape during bleaching.

track and the frame from which F_f is obtained must be preceded and followed by a frame in which the punctum is observed to ensure that F_f represents a single fluorophore emitting during the entire exposure of the frame.

4.2.5 Data Analysis

The average number is simply determined by dividing the average intensity of the unbleached sample (\bar{F}_i) by the average final intensity (\bar{F}_f). Previously we have shown that single fluorophores exhibit an intrinsic lognormal distribution in fluorescence intensity when imaged in TIRF microscopy.⁸ By fitting the histogram of the intensities with a lognormal distribution and comparing the multiplicative standard deviations,¹¹ or relative widths (σ^*), of the initial intensity distribution (σ_i^*) and final intensity distribution (σ_f^*) we can determine if the variability in the number of fluorophores over the sample population is significant. When σ_i^* and σ_f^* are not equal, a distribution of fluorophores within the sample is found using a previously demonstrated deconvolution technique.⁸⁻¹⁰ To determine the distribution in the number of fluorophores, $\{F_i\}$ is fit with a series of calibration distributions generated from the final intensity distribution ($\{F_f\}$).

4.3 Results and Discussion

4.3.1 Optimization of Intensity Extraction from Photobleaching Track

To verify that F_f obtained from the photobleaching track correlated to the fluorescence of a single fluorophore there are two types of user controlled parameters had to be optimized in the

photobleach tracking program: (1) those that help to ensure that the fluorescence is not from multiple fluorophores that bleach simultaneously or the sample did not leave the imaging region before complete bleaching occurred and (2) those that ensure that the fluorescence is from a punctum that correlates to the original punctum. The parameters that contribute to accurately extracting F_f are the frame cutoff (n_{co}), the number of blinks (n_b), and the required number of frames with a usable punctum (n_{up}). If n_{co} is set too low the track may be terminated early and the corresponding intensity has a higher risk of correlating to two fluorophores blinking resulting in a seemingly lower final average fluorophore count. For our samples we found that n_{co} of 10 frames was sufficient. We found that varying n_{co} between 6 and 18 frames showed variations in the final average fluorophore count that all fell within two times the standard deviation of the mean found for n_{co} of 10 frames suggesting that there is no significant difference over this cutoff range. However, we did find that n_{co} set below 6 frames showed a dramatic difference (outside the recommended standard deviation of the mean) in the average number of fluorophores.

The required number of frames (n_{up}) is the number of frames in which the punctum is considered part of the tail of the photobleaching track and is a suitable punctum in which to extract F_f from (i.e. has a frame preceding and following in which the puncta is present). The larger n_{up} is set the longer the resulting tail lengths are of acceptable photobleaching tracks therefore increasing the potential of extracting the proper single intensity. Additionally, the potential for an intensity corresponding to two fluorophores blinking simultaneously is decreased the larger n_b is set. We found that we only required 1 blink and 1 acceptable frame for our samples. The average number of fluorophores found when increasing the n_b and n_{up} was all

within a single standard deviation of the mean number of fluorophores found with only a single blink and a single acceptable frame.

To verify that the final punctum correlates to the original punctum there are two parameters, acceptance distance (d_{ac}) and maximum distance (d_{max}), which both compare the position of the center of the final punctum to the center of the original punctum. Our samples were allowed to adsorb to the glass surface and no further amount of immobilization was done. Small variations in the samples location between frames may occur due to drift in the microscope and diffusion on the surface and these two parameters account for these potential changes during the course of the photobleaching process. Acceptance distance (d_{ac}) is used when generating the photobleaching track and can be set larger than d_{max} , which compares the position one last time before outputting F_f , to ensure that the photobleaching track is not prematurely terminated due to excessive movement over the time course of the photobleaching process. We found that when d_{ac} and d_{max} are set too low the observed average fluorophore count will be lower than the actual average count due to movement of the sample over the length of time needed to bleach the larger number of fluorophores. As d_{ac} and d_{max} get larger, we found that the final average count does not change but the number of final puncta decreases because the program finds multiple potential puncta during the tracking process and rejects the original punctum. For our samples, we found that d_{ac} of 2 pixels and d_{max} of 1 pixel were optimum.

4.3.2 Quantifying Fluorophores in Alexa Labeled Antibodies and SpH Vesicles

To demonstrate the capability of using photobleaching to complement our previously developed quantitative microscopy technique, we counted the fluorophores in two types of samples: (1) single Alexa Fluor 488 (Alexa-488) on labeled goat anti-mouse (GAM-488) antibodies and (2) GFP in synaptic vesicles from transgenic mice expressing synaptotHluorin (spH). The fluorescence of Alexa-488 dye is environmentally insensitive and the average number of fluorophores per GAM-488 is previously determined by Invitrogen making it suitable to verify that F_f extracted from the photobleaching track properly represents a single fluorophore. The reported degree of labeling for the particular lot of GAM-488 was an average of 5 fluorophores. We found that average fluorescence of the labeled antibodies was the equivalent of 4.6 ± 0.3 (stand. err.) single Alexa-488s (n=12 data sets). The difference between the observed average number of fluorophores and the reported number of fluorophores may be due to quenching. Comparison of σ^* for $\{F_i\}$ and $\{F_f\}$ showed a similarity¹⁰ suggesting that the distribution in fluorescence intensity from the antibodies due to variability in the number of Alexa-488 over the antibody population is negligible. This result is important since it indicates that these antibodies can be used to obtain not just the average, but also the distribution of the number of bound antibodies in quantitative fluorescence experiments.¹⁰

Often, green fluorescent protein (GFP) is used as a reporter of expression in cellular and molecular biology and, unlike Alexa Fluor 488, GFP is sensitive to the surrounding environments, specifically to pH. In the case of spH vesicles, the GFP are expressed within the lumen of the synaptic vesicle where the exact nature of the environment that GFP is expressed is unknown making spH vesicles an excellent example of the types of samples where this technique

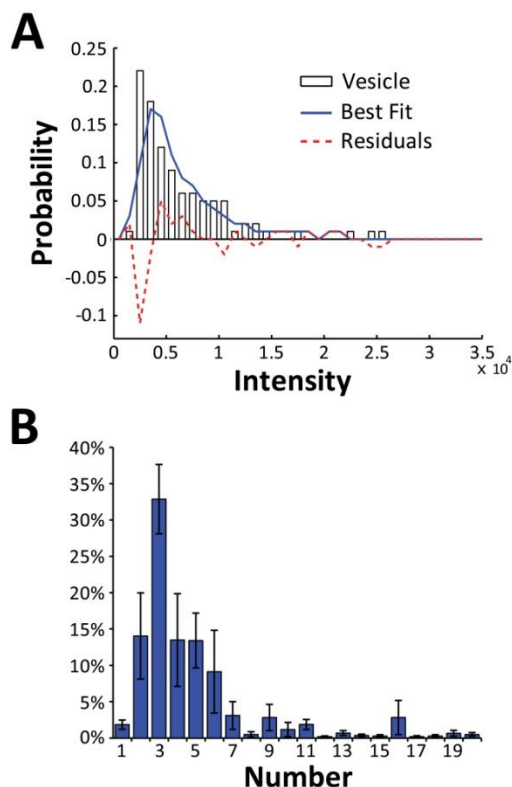


Figure 4-2. (A) Intensity distribution of GAM-488 with the best fit of single Alexa Fluoro 488 found from photobleaching. (B) Variation in number of Alexa Fluor 488 bound to GAM antibody. (C) Intensity distribution of spH vesicles with the best fit of single GFP found from photobleaching. (D) Variation in the number of GFP expressed in spH vesicles.

will be beneficial. Differences between σ_i^* (0.62 ± 0.03) and σ_f^* (0.46 ± 0.03) suggests that the variability in the number of GFP over the population of spH vesicles is a significant contributor to $\{F_i\}$. Figure 4-2 B shows the variation in the number of GFP over the population of single spH vesicles found from the deconvolution of $\{F_i\}$ with $\{F_f\}$. The distribution demonstrates a similar polydispersed nature that we observed previously when quantifying the number of synaptobrevin 2 (VAMP 2) proteins in synaptic vesicles isolated from rat brains.¹⁰ However, the average number of GFPs we found in spH vesicles is 4.4 ± 0.4 which is approximately 60% lower than the average number of VAMP 2 found in rat wild type synaptic vesicles. Previous

characterization of this spH vesicles showed that the expression of VAMP 2 was found to be nearly the same concentration between mouse wild type synapses and synapses containing spH vesicles.¹² Therefore, there are two potential possibilities that could contribute to the difference in the number of GFPs (assuming a single GFP is expressed per VAMP 2): (1) the difference in the level of VAMP 2 expressed between rats and mice vary or (2) not every VAMP 2 within a single synaptic vesicle expresses a GFP.

4.4 Conclusion

Using photobleaching to extract single fluorophore intensities, we were able to demonstrate how quantitative microscopy could be used to determine the average number of fluorophores and the variation in that number for samples where environmental effects on the photophysical properties of the fluorophore make it difficult to obtain an accurate single intensity for calibration. In cellular and molecular biology, an increasing number of fluorophores are being expressed in a variety of biological systems as biosensors to help develop a better understanding of the biological processes. We feel this technique will help in the characterization of biological systems expressing a wide variety of environmental sensitive fluorophores that before could not easily be characterized.

4.5 Chapter References

- (1) Wang, X.; Wang, S.; Ma, H. *Analyst* **2008**, *133*, 478-484.

- (2) Ghosh, S.; Guchhait, N. *Photochem. Photobiol.* **2009**, *86*, 290-296.
- (3) Wang, R.; Yu, C.; Yu, F.; chen, L. *Trends Anal. Chem.* **2010**, *29*, 1004-1013.
- (4) Budzinski, K. L.; Zeigler, M.; Fujimoto, B. S.; Bajjalieh, S. M.; Chiu, D. T. *Biophys. J.* **2011**, *101*, 1580-1589.
- (5) Chan, Y.-H.; Wu, C.; Ye, F.; Jin, Y.; Smith, P. B.; Chiu, D. T. *Anal. Chem.* **2011**, *83*, 1448-1455.
- (6) Li, F.; Westphal, A. H.; Marcelis, A. T. M.; Sudholter, E. J. R.; Stuart, M. A. C.; Leermakers, F. A. M. *Soft Matter* **2011**, *7*, 11211-11215.
- (7) Ye, F.; Wu, C.; Chan, Y.-H.; Zhang, X.; Chiu, D. T. *J. Am. Chem. Soc.* **2011**, *133*, 8146-8149.
- (8) Mutch, S. A.; Fujimoto, B. S.; Kuyper, C. L.; Kuo, J. S.; Bajjalieh, S. M.; Chiu, D. T. *Biophys. J.* **2007**, *92*, 2962-2943.
- (9) Mutch, S. A.; Gadd, J. C.; Fujimoto, B. S.; Kensel-Hammes, P.; Schiro, P. G.; Bajjalieh, S. M.; Chiu, D. T. *Nat. Protoc.* **2011**, *6*, 1953-1968.
- (10) Mutch, S. A.; Kensel-Hammes, P.; Gadd, J. C.; Fujimoto, B. S.; Allen, R. W.; Schiro, P. G.; Lorenz, R. M.; Kuyper, C. L.; Kuo, J. S.; Bajjalieh, S. M.; Chiu, D. T. *J. Neurosci.* **2011**, *31*, 1461-1470.
- (11) Limpert, E.; Stahel, W. A.; Abbt, M. *BioScience* **2001**, *51*, 341-352.
- (12) Li, Z.; Burrone, J.; Tyler, W. J.; Hartman, K. N.; Albeanu, D. F.; Murthy, V. N. *Proc. Natl. Acad. Sci. U.S.A.* **2005**, *102*, 6131-6136.

Chapter 5: Probing the Interior of Synaptic Vesicles with Internalized Nanoparticles

5.1 Introduction

Studies have shown links between intravesicular concentrations of small molecules, such as protons¹ and chloride², and the uptake of neurotransmitters into synaptic vesicles. Current methods for probing the intravesicular region include the use of dyes that can cross the synaptic vesicle membrane, such as acridine orange³ and Oregon green,⁴ but the non-specificity of the dyes and self-quenching at high dye concentrations⁵ make them unreliable for real-time measurements within the synaptic-vesicle lumen. Similarly, genetic transfections of fluorescent proteins, such as pH sensitive green-fluorescent protein, have been used as probes within synaptic vesicles,⁶ but genetic modifications potentially alter composition and function of synaptic vesicles. We have sought to develop a technique in which nanoparticles incorporating fluorescent based sensors are loaded into synaptic vesicles for real-time monitoring of the intravesicular concentration of important molecules with minimal interference to synaptic-vesicle function.

Semiconducting polymer dots (Pdots) have emerged as an ideal platform for nanoparticle fluorescent-based sensors for a variety of reasons: (1) Pdots have a broad size range (tens of nanometers to hundreds of nanometers) providing the ability to tune the size of the nanoparticle for various applications.^{7,8} (2) The surface of a Pdot is easily functionalized to improve biocompatibility and to allow further bioconjugation.⁹⁻¹¹ (3) Finally, Pdots show improved

brightness and high photostability compared to other nanoparticles.^{12,13} By conjugating a pH-sensitive dye with a pH-insensitive Pdot, we were able to develop a sensitive and robust pH sensing probe that can be used to measure the pH in a range of biological applications.¹⁴

We are particularly interested in using the pH sensing Pdots to monitor the fluctuation of pH within the lumen region of synaptic vesicles at a single-vesicle level. Though Pdots are small enough to fit inside a synaptic vesicle, they are too large to diffuse through the membrane or be transported into the vesicle and a technique in which synaptic vesicles uptake nanoparticles is needed. To address this, we explored loading nanoparticles into synaptic vesicles using synaptosomes, which are isolated nerve terminals that allow synaptic vesicles to still undergo endo- and exocytosis. Utilizing synaptosomes, we were able to stimulate synaptic vesicles to uptake nanoparticles through endocytosis and then further isolate the synaptic vesicles for single-vesicle studies.¹⁵ This loading capability in conjunction with our pH-sensing Pdots will enable us to develop a better understanding of the transporters that play an essential role in the loading of neurotransmitters into synaptic vesicles.

5.2 pH Sensing Semiconducting Polymer Dots

5.2.1 Materials

The following materials were purchased from Sigma-Aldrich: poly-(2,5-di(3',7'-dimethyloctyl)phenylene-1,4-ethynylene (PPE) and tetrahydrofuran (THF; anhydrous, $\geq 99.9\%$, inhibitor free). Amino-terminated polystyrene (PS-NH₂) was purchased from ADS Dyes, Inc.

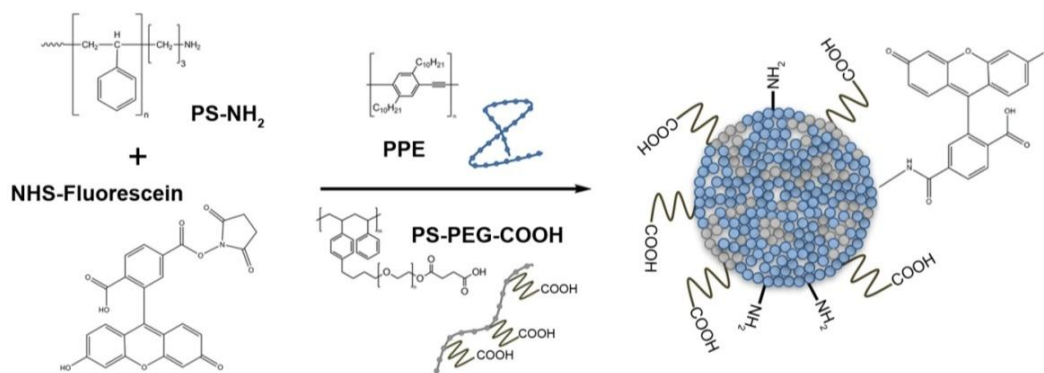


Figure 5-1. Schematic showing route for the preparation of pH-sensitive Pdot.

(Quebec, Canada) and all other chemicals were purchased from Invitrogen (Carlsbad, CA). All chemicals were used as received without further purification.

5.2.2 Generation of pH Sensing Pdot

To prepare Pdot pH-sensors, initially, 13mg of NHS-fluorescein and 20 mg of PS-NH₂ was dissolved in 4ml of anhydrous dimethylformamide. The solution was stirred and allowed to react overnight. Then 100 μ l of PPE at 1 mg/ml in THF, 15 μ l of polystyrene polyethylene glycol carboxylic acid (PS-PEG-COOH) at 2 mg/ml in THF, and 40 μ l of the PS-NH₂-Fluorescein conjugate were added to 5 ml of THF. The Pdots were formed by quickly injecting this solution into 10ml of ultrapure water under vigorous sonication. Nitrogen was bubbled through the solution of Pdots while on a hotplate set at 125°C for 30 min to purge the THF from the solution. The resulting Pdots were filtered through a 0.2 μ m cellulose acetate membrane filter to remove aggregates that may have formed during the preparation. The Pdot solution was further concentrated by adding 80 μ l of Triton X-100 at 2.5 wt% in ultrapure water and

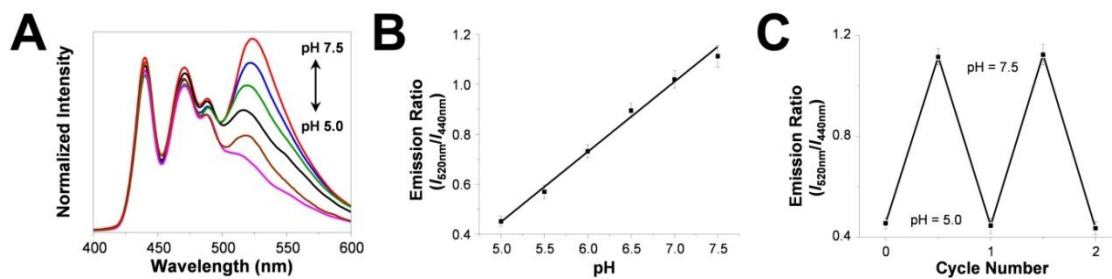


Figure 5-2. (A) Fluorescence spectra of pH-sensing Pdot at different pH (red line: pH = 7.5, blue line: pH = 7, green line: pH = 6.5, black line: pH = 6, brown line: pH = 5.5, and pink line: pH = 5). 390nm excitation wavelength. (B) Ratiometric pH calibration plot of the emission ratio (I_{513nm}/I_{440nm}). (C) Emission ratio (I_{513nm}/I_{440nm}) when pH is toggled between 5.0 and 7.5 to demonstrate the reversibility and reproducibility of pH-sensing Pdots.

centrifuging in a centrifugal ultrafiltration tube (Amicon Ultra-4, MWCO: 100kDa) at $2,750\times g$ for 3 min.

5.2.3 Characterization of pH Sensitivity

When developing the pH-sensing Pdot, it was important to maximize their sensitivity. Previously, fluorescent pH-sensitive dyes were covalently linked to quantum dots (Qdots) in which Förster resonance energy transfer (FRET) occurred to monitor the pH.^{16,17} In this instance, the ratio between the emission intensities from the Qdot and the fluorescent dye was used to measure the pH. Ratiometric measurements are less susceptible to environmental effects providing an advantage over measuring pH based on the fluorescence from the dye alone. To take advantage of this property, PPE was chosen as the semiconducting polymer core due to the overlap of the emission of PPE and the excitation of the pH sensitive dye, fluorescein. In addition, PPE is insensitive to changes in pH serving as an internal standard when measuring the pH of the surrounding environment. Figure 5-2 A shows how the emission of fluorescein ($\lambda =$

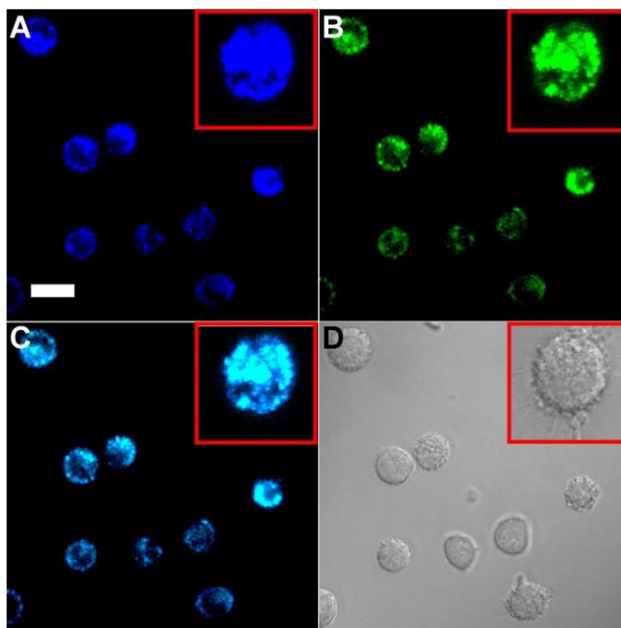


Figure 5-3. Confocal microscopy images of pH-sensitive Pdots inside live HeLa cells at $\lambda_{exc} = 405\text{nm}$. (A) Emission from PPE (integrated from 433 to 444nm). (B) Emission of fluorescein (integrated from 507 to 518nm). (C) Overlay of the emissions from PPE and fluorescein. (D) Brightfield image of the HeLa cells. The insets show a magnified version of a single HeLa cell and the scale bar is $20\mu\text{m}$.

513nm) increases in response to an increase in pH while the emission of PPE ($\lambda = 440\text{nm}$) remains relatively unchanged.

The pH-sensing Pdots were further characterized by examining the sensitivity and robustness of the pH measurements with fluorescence spectroscopy. The correlation between pH and the emission ratio ($I_{513\text{nm}}/I_{440\text{nm}}$) was found to be linear in the range of pH = 5 to 7.5 (Figure 5-2 B). A 0.27 per unit change of pH was found over this range. The Pdot pH sensors demonstrated excellent reversibility and reproducibility when measuring the pH of a solution that was continually toggled between 5 and 7.5 (Figure 5-2 C).

To demonstrate the capabilities of the Pdot pH sensors in a biological sample, the Pdots were loaded into live HeLa cells to measure the intracellular pH. These live cell experiments

were performed with Pdots generated as described above but with no PS-PEG-COOH. The HeLa cells were incubated in the presence of the Pdot pH sensors and the Pdots were taken up via endocytosis. After rinsing the cells with fresh phosphate buffered saline to remove excess Pdots, confocal images of the HeLa cells were acquired (Figure 5-3). The intracellular pH was measured by calculating the ratio of the average intensity of the fluorescein emission (507 to 518nm) to the average intensity of the PPE emission (433 to 444nm). The intracellular pH was found to be 4.8 ± 0.9 which is in agreement with previously reported pH ranges.¹⁴

5.3 Synaptosomes as a Loading Platform for Nanoparticles into Synaptic Vesicles

5.3.1 Materials

Mice were wild type strain C57black6 courtesy of Sandra Bajjalieh. The mice were used in accordance to University of Washington animal practices. Q605 quantum dots and FM4-64 dye were obtained from Invitrogen. All other chemicals were purchased from Sigma-Aldrich.

5.3.2 Loading Nanoparticles into Synaptic Vesicles

5.3.2.1 Synaptosome Isolation

Freshly isolated mouse brains were placed in a chilled Teflon-glass tissue grinder and homogenized in ice cold homogenization buffer (10 mM 4-(2-hydroxyethyl)-1-piperazineethanesulfonic acid (HEPES), 300 mM sucrose, pH 7.4) with 10 strokes. The homogenate was centrifuged at 1 000g for 10 min at 4°C to remove cellular debris. The resulting

supernatant was centrifuged again at 24 500g for 13 min at 4°C resulting in a crude mitochondrial pellet containing the synaptosomes and additional cellular organelles. The synaptosomes were further purified by re-suspending the crude mitochondrial pellet in ice cold homogenization buffer and placing on a Percoll gradient consisting of a layer of 23%, 10%, and 3% percoll in sucrose/EDTA buffer (5 mM HEPES, 300 mM sucrose, 1 mM EDTA, pH 7.4). The gradients were centrifuged at 23 000g for 20 min at 4°C with slow acceleration and no braking during deceleration. Isolated synaptosomes were collected from the interface between the 10% and 23% percoll layers. To remove excess percoll from the synaptosomes, isolated synaptosomes were diluted into Krebs-like buffer (118.5 mM sodium chloride, 4.7 mM potassium chloride, 1.2 mM calcium chloride, 1.18 mM magnesium chloride, 10 mM glucose, 20 mM HEPES, 0.1 mM disodium hydrogen phosphate, pH 7.4) and pelleted by centrifuging at 18 970g for 10 min at 4°C. The final synaptosome pellet was re-suspended and the final protein concentration was adjusted to 0.3 mg/ml using Krebs-like buffer.

5.3.2.2 Nanoparticle Loading

Isolated synaptosomes were incubated in the presence of 200 nM Qdot and 20 μ M of FM4-64 for 10 min while in a 37°C water bath. The synaptosomes were stimulated for 2 min with 30 mM K⁺ Krebs-like buffer (63.2 mM sodium chloride, 60 mM potassium chloride, 1.2 mM calcium chloride, 1.18 mM magnesium chloride, 10 mM glucose, 20 mM HEPES, 0.1 mM disodium hydrogen phosphate, pH 7.4). The stimulation induced the endo- and exocytosis of the synaptic vesicles causing the vesicles to take up any Qdots and FM4-64 located at the surface of the synaptosome (Figure 5-4). After stimulation, the synaptosomes were centrifuged at 8 400g

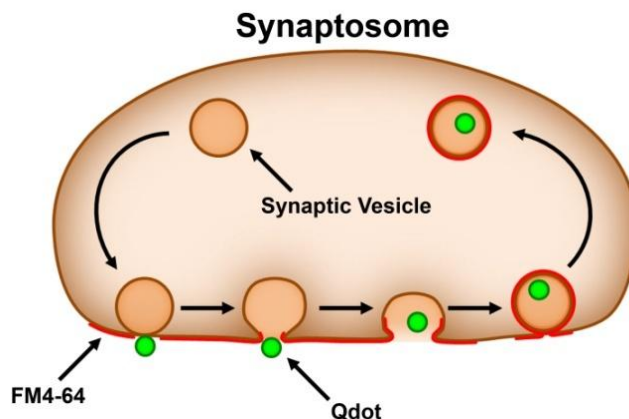


Figure 5-4. Schematic of the uptake of FM4-64 and Qdots into synaptic vesicles via synaptosomes.

for 3 min at 4°C and washed twice, once with Krebs-like buffer containing 1 mg/ml bovine serum albumin (BSA) and once with Krebs-like buffer without BSA, to remove excess Qdots and FM4-64. Then synaptosomes were re-suspended in ice-cold homogenization buffer.

5.3.2.3 Synaptic Vesicle Isolation

Synaptic vesicles were isolated from the synaptosomes by adding nine volumes of cold ultrapure water to the re-suspended synaptosomes and then homogenized with 3 strokes in a chilled Teflon-glass tissue grinder. The synaptosomes were left on ice for 30 min to allow for full rupture. Cellular debris was removed by centrifuging at 22 460g for 9 min at 4°C. The supernatant was removed and centrifuged one final time at 217 410g for 1.5 hours at 4°C to pellet the synaptic vesicles. Finally, the pellet of synaptic vesicles was re-suspended into potassium acetate buffer (20 mM HEPES, 110 mM potassium acetate, 4 mM magnesium sulfate, 4 mM potassium chloride, pH 7.4).

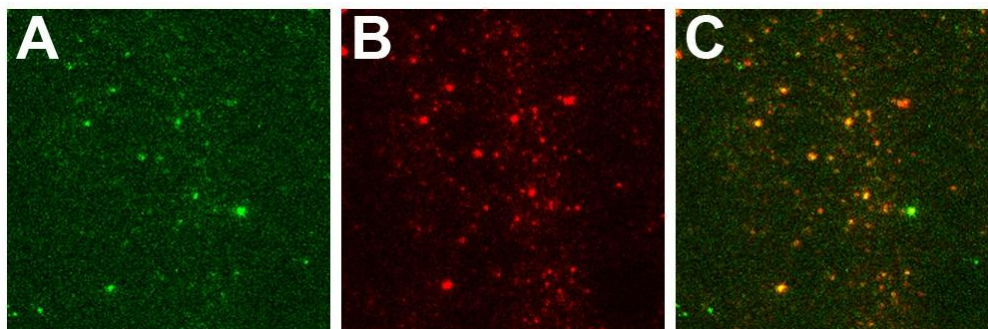


Figure 5-5. Images of isolated synaptic vesicles loaded with Qdot and FM4-64. (A) Qdots in synaptic vesicles. (B) Synaptic vesicles labeled with FM4-64. (C) Overlay showing successful loading of Qdot into synaptic vesicles.

5.3.3 Verifying Loading of Nanoparticles into Synaptic Vesicles

Previous studies have shown that Qdots can be taken up by synaptic boutons in neuronal cultures.¹⁸ Quantum dots are well-characterized nanoparticles that can be easily acquired in a size (~15nm) that is small enough to fit within a synaptic vesicle (~50nm). Also, Qdots can be obtained with a carboxyl functionalized surface to improve the non-specific interaction of the Qdot to neuronal membranes. Therefore, Qdots were the ideal model fluorescent sensor to use when developing the technique for loading nanoparticles into synaptic vesicles via synaptosomes. A membrane selective dye, FM4-64, was simultaneously loaded into the synaptic vesicles as an additional label to verify the loading of Qdots. Total internal reflection fluorescence (TIRF) microscopy was used to image the synaptic vesicles (Figure 5-5). Overlaid images of Qdots and FM4-64 showed that $25.8 \pm 11.1\%$ of vesicles appeared to contain a nanoparticle.¹⁵

Due to the preference of Qdots to neuronal membranes, it is possible that excess Qdots may not have been removed during the washing steps in the procedure. A black hole quencher (BHQ) was utilized to distinguish Qdots encapsulated in synaptic vesicles from those that were

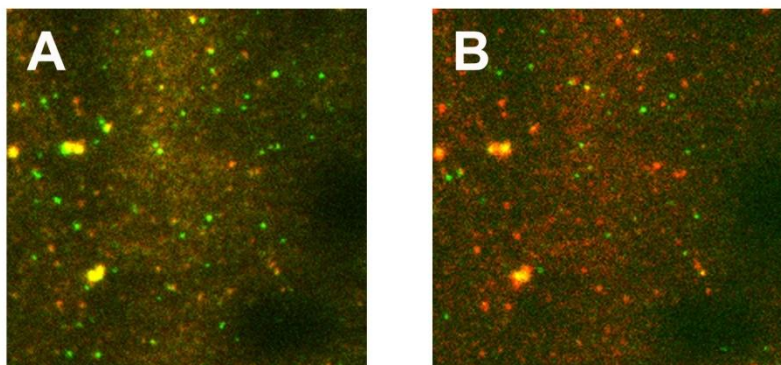


Figure 5-6. Overlay images of synaptic vesicles loaded with Qdot (green) and FM4-64 (red). (A) Synaptic vesicles before treatment with BHQ-2. (B) Synaptic vesicle after treatment with BHQ-2.

bound to the exterior of the vesicle (Figure 5-6). Images of vesicles after quenching with BHQ showed that $15.6 \pm 5.1\%$ of synaptic vesicles actually had encapsulated Qdots.¹⁵

5.4 Considerations when Loading Polymer Dots into Synaptic Vesicles

There were two main advantages to using Qdots as a model nanoparticle when developing the synaptic vesicle loading technique: (1) The Qdots used were small in size with a narrow size distribution (Figure 5-7 A) which was necessary to fit within the intravesicular region of the synaptic vesicle and (2) the negatively charged surface of carboxyl functionalized Qdots improved the non-specific interaction with the synaptosome surface.¹⁸ When developing alternative options for fluorescence based nanoparticle sensors, size and surface functionalization are important properties to control. As discussed previously, Pdots are ideal fluorescent based sensors due to their sensitivity and robustness. In addition, the size and surface functional groups can be easily controlled to optimize the Pdot for use in a wide range of studies.

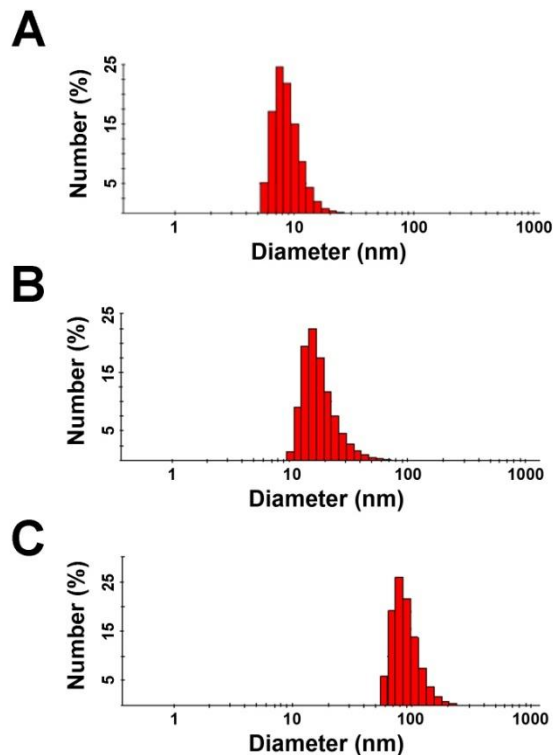


Figure 5-7. Dynamic light scattering measurements of the size distributions of (A) Q605 Qdots, (B) PFBT polymer dots generated with a slow injection and high powered sonication technique, and (C) PFBT polymer dots generated with a fast injection and low powered sonication technique.

Figure 5-7 shows how Pdots composed of poly[(9,9-dioctylfluorenyl-2,7-diyl)-co-(1,4-benzo-{2,1',3}-tiadiazole)] (PFBT) can be generated in various sizes through minor alterations to the procedure. In this case, PFBT Pdots with an average diameter of 16nm were generated by slowly injecting (3 min/ml) a PFBT/THF solution into ultrapure water during sonication using a probe sonicator with a high local sonicating power and an average diameter of 70nm was achieved by quickly injecting (<1 min) the PFBT/THF solution into ultrapure water under sonication with a typical bath sonicator. Using these methods, the size of Pdots can be optimized for each specific application.

Similarly, functionalization of Pdots is achieved with minimal variation in the method for generating Pdots. The surface of Pdots can be functionalized by including a small amount of amphiphilic polymer containing the functional group of interest with the semiconducting polymer during the formation step. Functionalization of Pdots can be verified through measurement of the ζ -potential. For example, non-functionalized poly[2-methoxy-5-(2-ethylhexyloxy)-1,4-(1-cyanovinylene-1,4-phenylene)] (CN-PPV) Pdots were found to have a ζ -potential of -35mV while CN-PPV Pdots generated with 20% poly(styrene-co-maleic anhydride) (PSMA) were found to have a ζ -potential of -55mV. By applying techniques for controlling the size and modifying the surface functional groups, pH-sensitive Pdots can be optimized for loading into synaptic vesicles.

5.5 Conclusion

Synaptic vesicles play an important role in neuronal communication. Therefore, development of techniques and new approaches for studying these subcellular organelles is ongoing. We have successfully used synaptosomes to load nanoparticles into synaptic vesicles and then isolate the vesicles for further single-vesicle studies. By combining this loading technique with the pH-sensitive Pdots, we anticipate the ability to probe the intravesicular region of the synaptic vesicle while avoiding the drawbacks of other similar techniques. The pH sensing Pdots offer a sensitivity that will contribute to development of a better understanding of the uptake of protons into synaptic vesicles and eventually how this relates to the overall function of this organelle.

5.6 Chapter References

- (1) Budzinski, K. L.; Allen, R. W.; Fujimoto, B. S.; Kensel-Hammes, P.; Belnap, D. M.; Bajjalieh, S. M.; Chiu, D. T. *Biophys. J.* **2009**, *97*, 2577-2584.
- (2) Schenck, S.; Wojcik, S. M.; Brose, N.; Takamori, S. *Nat. Neurosci.* **2009**, *12*, 156-162.
- (3) Zoccarato, F.; Cavallini, L.; Alexandre, A. *J. Neurochem.* **1999**, *72*, 625-633.
- (4) Zeigler, M. B.; Allen, P. B.; Chiu, D. T. *Biophys. J.* **2011**, *100*, 2846-2851.
- (5) Palmgren, M. G. *Anal. Biochem.* **1991**, *192*, 316-321.
- (6) Budzinski, K. L.; Zeigler, M.; Fujimoto, B. S.; Bajjalieh, S. M.; Chiu, D. T. *Biophys. J.* **2011**, *101*, 1580-1589.
- (7) Ye, F.; Wu, C.; Jin, Y.; Chan, Y.-H.; Zhang, X.; Chiu, D. T. *J. Am. Chem. Soc.* **2011**, *133*, 8146-8149.
- (8) Ye, F.; Wu, C.; Jin, Y.; Wang, M.; Chan, Y.-H.; Yu, J.; Sun, W.; Hayden, S.; Chiu, D. T. *Chem. Commun.* **2011**.
- (9) Wu, C.; Schneider, T.; Zeigler, M.; Yu, J.; Schiro, P. G.; Burnham, D. R.; McNeill, J. D.; Chiu, D. T. *J. Am. Chem. Soc.* **2010**, *132*, 15410-15417.
- (10) Chan, Y.-H.; Jin, Y.; Wu, C.; Chiu, D. T. *Chem. Commun.* **2011**, *47*, 2820-2822.
- (11) Wu, C.; Hansen, S. J.; Hou, Q.; Yu, J.; Zeigler, M.; Jin, Y.; Burnham, D. R.; McNeill, J. D.; Olson, J. M.; Chiu, D. T. *Angew. chem. Int. Ed.* **2011**, *50*, 3430-3434.
- (12) Jin, Y.; Ye, F.; Zeigler, M.; Wu, C.; Chiu, D. T. *ACS Nano* **2011**, *5*, 1468-1475.

- (13) Wu, C.; Jin, Y.; Schneider, T.; Burnham, D. R.; Smith, P. B.; Chiu, D. T. *Angew. chem. Int. Ed.* **2010**, *49*, 9436-9440.
- (14) Chan, Y.-H.; Wu, C.; Ye, F.; Jin, Y.; Smith, P. B.; Chiu, D. T. *Anal. Chem.* **2011**, *83*, 1448-1455.
- (15) Budzinski, K. L.; Sgro, A. E.; Fujimoto, B. S.; Gadd, J. C.; Shuart, N. G.; Gonen, T.; Bajjalieh, S. M.; Chiu, D. T. *ACS Chem. Neurosci.* **2011**, *2*, 236-241.
- (16) Jin, T.; Sasaki, A.; Kinjo, M.; Miyazaki, J. *Chem. Commun.* **2010**, *46*, 2408-2410.
- (17) Suzuki, M.; Husimi, Y.; Komatsu, H.; Suzuki, K.; Douglas, K. T. *J. Am. Chem. Soc.* **2008**, *130*, 5720-5725.
- (18) Zhang, Q.; Cao, Y.-Q.; Tsien, R. W. *Pro. Natl. Acad. Sci. U.S.A.* **2007**, *104*, 17843-17848.

List of References

- Ales, E.; Tabares, L.; Poyato, J. M.; Valero, V.; Lindau, M.; De, T. G. A. *Nat. Cell Biol.* **1999**, *1*, 40-44.
- Allison, S. A. *Biopolymers* **1988**, *27*, 97-111.
- Aravanis, A. M.; Pyle, J. L.; Tsien, R. W. *Nature* **2003**, *423*, 643-647.
- Axelrod, D. *Methods Cell. Biol.* **1989**, *30*, 245-270.
- Beer, N. R.; Hindson, B. J.; Wheeler, E. K.; Hall, S. B.; Rose, K. A.; Kennedy, I. M.; Colston, B. W. *Anal. Chem.* **2007**, *79*, 8471-8475.
- Bevington, P. R. *Data Reduction and Error Analysis for the Physical Sciences.*; McGraw-Hill: New York, 1969.
- Bock, G.; Steinlein, P.; Huber, L. A. *Tr. Cell Biol.* **1997**, *7*, 499-503.
- Buckley, K.; Kelly, R. B. *J. Cell Biol.* **1985**, *100*, 1284-1294.
- Budzinski, K. L.; Allen, R. W.; Fujimoto, B. S.; Kensel-Hammes, P.; Belnap, D. M.; Bajjalieh, S. M.; Chiu, D. T. *Biophys. J.* **2009**, *97*, 2577-2584.
- Budzinski, K. L.; Sgro, A. E.; Fujimoto, B. S.; Gadd, J. C.; Shuart, N. G.; Gonen, T.; Bajjalieh, S. M.; Chiu, D. T. *ACS Chem. Neurosci.* **2011**, *2*, 236-241.
- Budzinski, K. L.; Zeigler, M.; Fujimoto, B. S.; Bajjalieh, S. M.; Chiu, D. T. *Biophys. J.* **2011**, *101*, 1580-1589.
- Burger, P. M.; Mehl, E.; Cameron, P. L.; Maycox, P. R.; Baumert, M.; Lottspeich, F.; De Camilli, P.; Jahn, R. *Neuron* **1989**, *3*, 715-720.
- Burre, J.; Beckhaus, T.; Schaeffer, H.; Corvey, C.; Hofmann, S.; Karas, M.; Zimmermann, H.; Volkandt, W. *Proteomics* **2006**, *6*, 6250-6262.
- Calakos, N.; Scheller, R. H. *J. Biol. Chem.* **1994**, *269*, 24534-24537.
- Ceccarelli, B.; Hurlbut, W. P.; Mauro, A. *J. Cell Biol.* **1973**, *57*, 499-524.
- Chan, Y.-H.; Jin, Y.; Wu, C.; Chiu, D. T. *Chem. Commun.* **2011**, *47*, 2820-2822.
- Chan, Y.-H.; Wu, C.; Ye, F.; Jin, Y.; Smith, P. B.; Chiu, D. T. *Anal. Chem.* **2011**, *83*, 1448-1455.
- Cheezum, M. K.; Walker, W. F.; Guilford, W. H. *Biophys. J.* **2001**, *81*, 2378-2388.

- Chen, Y.; Lagerholm, B. C.; Yang, B.; Jacobson, K. *Methods* **2006**, *39*, 147-153.
- Chirico, G.; Fumagalli, C.; Baldini, G. *J. Phys. Chem. B* **2002**, *106*, 2508-2519.
- Chiu, D. T.; Zare, R. N. *J. Am. Chem. Soc.* **1996**, *118*, 6512-6513.
- Colliver, T. L.; Pyott, S. J.; Achalabun, M.; Ewing, A. G. *J. Neurosci.* **2000**, *20*, 5276-5282.
- Cunningham, E. *Proc. R. Soc. A* **1910**, *83*, 357-365.
- Daniels, R. W.; Collins, C. A.; Chen, K.; Gelfand, M. V.; Featherstone, D. E.; DiAntonio, A. *Neuron* **2006**, *49*, 11-16.
- Delon, A.; Wang, I.; Lambert, E.; Mache, S.; Mache, R.; Derourd, J.; Motto-Ros, V.; Galland, R. *J. Phys. Chem. B* **2010**, *114*, 2988-2996.
- Edgar, J. S.; Pabbati, C. P.; Lorenz, R. M.; He, M.; Fiorini, G. S.; Chiu, D. T. *Anal. Chem.* **2006**, *78*, 6948-6954.
- Fernandez-Alfonso, T.; Kwan, R.; Ryan, T. A. *Neuron* **2006**, *51*, 179-186.
- Fiorini, G. S.; Chiu, D. T. *Biotechniques* **2005**, *38*, 429-446.
- Garcia de la Torre, J. G.; Bloomfield, V. A. *Q. Rev. Biophys.* **1981**, *14*, 81-139.
- Gauthier, D. J.; Sobota, J. A.; Ferraro, F.; Mains, R. E.; Lazure, C. *Proteomics* **2008**, *8*, 3848-3861.
- Ghosh, S.; Guchhait, N. *Photochem. Photobiol.* **2009**, *86*, 290-296.
- Goda, Y.; Sudhof, T. C. *Curr. Opin. Cell Biol.* **1997**, *9*, 513-518.
- Goldstein, A. Y. N.; Wang, X.; Schwarz, T. L. *Curr. Opin. Neurobiol.* **2008**, *18*, 495-503.
- Goulian, M.; Simon, S. M. *Biophys. J.* **2000**, *79*, 2188-2198.
- Gracz, L. M.; Parsons, S. M. *Biochim. Biophys. Acta* **1996**, *1292*, 293-302.
- Gracz, L. M.; Wang, W. C.; Parsons, S. M. *Biochemistry* **1988**, *27*, 5268-5274.
- Hayashi, M.; Raimondi, A.; O'Toole, E.; Paradise, S.; Collesi, C.; Cremona, O.; Ferguson, S. M.; De, C. P. *Proc. Natl. Acad. Sci. U. S. A.* **2008**, *105*, 2175-2180.
- He, L.; Wu, L.-G. *Trends Neurosci.* **2007**, *30*, 447-455.
- He, L.; Wu, X.-S.; Mohan, R.; Wu, L.-G. *Nature (London, U. K.)* **2006**, *444*, 102-105.

- He, M.; Edgar, J. S.; Jeffries, G. D.; Lorenz, R. M.; Shelby, J. P.; Chiu, D. T. *Anal. Chem.* **2005**, *77*, 1539-1544.
- He, M.; Sun, C.; Chiu, D. T. *Anal. Chem.* **2004**, *76*, 1222-1227.
- Hell, J. W.; Maycox, P. R.; Stadler, H.; Jahn, R. *EMBO J.* **1988**, *7*, 3023-3029.
- Howell, K. E.; Gruenberg, J.; Ito, A.; Palade, G. E. *Prog. Clin. Biol. Res.* **1988**, *270*, 77-90.
- Jahn, R.; Sudhof, T. C. *J. Neurochem.* **1993**, *61*, 12-21.
- Jahn, R.; Sudhof, T. C. *Annu. Rev. Neurosci.* **1994**, *17*, 219-246.
- Jeffries, G. D.; Kuo, J. S.; Chiu, D. T. *Angew. Chem., Int. Ed. Engl.* **2007**, *46*, 1326-1328.
- Jin, T.; Sasaki, A.; Kinjo, M.; Miyazaki, J. *Chem. Commun.* **2010**, *46*, 2408-2410.
- Jin, Y.; Ye, F.; Zeigler, M.; Wu, C.; Chiu, D. T. *ACS Nano* **2011**, *5*, 1468-1475.
- Jung, N.; Haucke, V. *Traffic* **2007**, *8*, 1129-1136.
- Kapitein, L. C.; Kwok, B. H.; Weinger, J. S.; Schmidt, C. F.; Kapoor, T. M.; Peterman, E. J. G. *J. Cell Biol.* **2008**, *182*, 421-428.
- Klyachko, V. A.; Jackson, M. B. *Nature (London, U. K.)* **2002**, *418*, 89-92.
- Kuyper, C. L.; Budzinski, K. L.; Lorenz, R. M.; Chiu, D. T. *J. Am. Chem. Soc.* **2006**, *128*, 730-731.
- Kuyper, C. L.; Fujimoto, B. S.; Zhao, Y.; Schiro, P. G.; Chiu, D. T. *J. Phys. Chem. B* **2006**, *110*, 24433-24441.
- Kuyper, C. L.; Kuo, J. S.; Mutch, S. A.; Chiu, D. T. *J. Am. Chem. Soc.* **2006**, *128*, 3233-3240.
- Li, F.; Westphal, A. H.; Marcelis, A. T. M.; Sudholter, E. J. R.; Stuart, M. A. C.; Leermakers, F. A. M. *Soft Matter* **2011**, *7*, 11211-11215.
- Li, L.; Boedicker, J. Q.; Ismagilov, R. F. *Anal. Chem.* **2007**, *79*, 2756-2761.
- Li, Z.; Burrone, J.; Tyler, W. J.; Hartman, K. N.; Albeanu, D. F.; Murthy, V. N. *Proc. Natl. Acad. Sci. U.S.A.* **2005**, *102*, 6131-6136.
- Limpert, E.; Stahel, W. A.; Abbt, M. *BioScience* **2001**, *51*, 341-352.
- Lisman, J. E.; Raghavachari, S.; Tsien, R. W. *Nat. Rev. Neurosci.* **2007**, *8*, 597-609.

- Lorenz, R. M.; Edgar, J. S.; Jeffries, G. D.; Chiu, D. T. *Anal. Chem.* **2006**, *78*, 6433-6439.
- Lorenz, R. M.; Edgar, J. S.; Jeffries, G. D.; Zhao, Y.; McGloin, D.; Chiu, D. T. *Anal. Chem.* **2007**, *79*, 224-228.
- Magde, D.; Elson, E.; Webb, W. W. *Phys. Rev. Lett.* **1972**, *29*, 705-708.
- Matthews, G. *Neuron* **2004**, *44*, 223-226.
- Matveeva, E. A.; Vanaman, T. C.; Whiteheart, S. W.; Slevin, J. T. *Epilepsy Res.* **2007**, *73*, 266-274.
- Matveeva, E. A.; Vanaman, T. C.; Whiteheart, S. W.; Slevin, J. T. *Epilepsia* **2008**, *49*, 1749-1758.
- Matveeva, E. A.; Whiteheart, S. W.; Slevin, J. T. *J. Neurochem.* **2003**, *84*, 621-624.
- McCammon, J. A.; Deutch, J. M. *Biopolymers* **1976**, *15*, 1397-1408.
- Mirnic, K.; Middleton, F. A.; Marquez, A.; Lewis, D. A.; Levitt, P. *Neuron* **2000**, *28*, 53-67.
- Montiel, D.; Cang, H.; Yang, H. *J. Phys. Chem. B* **2006**, *110*, 19763-19770.
- Morciano, M.; Burre, J.; Corvey, C.; Karas, M.; Zimmermann, H.; Volkhardt, W. *J. Neurochem.* **2005**, *95*, 1732-1745.
- Moschakis, T.; Murray, B. S.; Dickinson, E. *Langmuir* **2006**, *22*, 4710-4719.
- Mousavi, S. A.; Malerod, L.; Berg, T.; Kjekshus, R. *Biochem. J.* **2004**, *377*, 1-16.
- Muller, M.; Goutman, J. D.; Kochubey, O.; Schneggenburger, R. *J. Neurosci.* **2010**, *30*, 2007-2016.
- Murthy, V. N.; Stevens, C. F. *Nature* **1998**, *392*, 497-501.
- Mutch, S. A.; Fujimoto, B. S.; Kuyper, C. L.; Kuo, J. S.; Bajjalieh, S. M.; Chiu, D. T. *Biophys. J.* **2007**, *92*, 2926-2943.
- Mutch, S. A.; Gadd, J. C.; Fujimoto, B. S.; Kinsel-Hammes, P.; Schiro, P. G.; Bajjalieh, S. M.; Chiu, D. T. *Nat. Protoc.* **2011**, *6*, 1953-1968.
- Mutch, S. A.; Kinsel-Hammes, P.; Gadd, J. C.; Fujimoto, B. S.; Allen, R. W.; Schiro, P. G.; Lorenz, R. M.; Kuyper, C. L.; Kuo, J. S.; Bajjalieh, S. M.; Chiu, D. T. *J. Neurosci.* **2011**, *31*, 1461-1470.

- Osborne, M. A.; Balasubramanian, S.; Furey, W. S.; Klenerman, D. *J. Phys. Chem. B* **1998**, *102*, 3160-3167.
- Palmgren, M. G. *Anal. Biochem.* **1991**, *192*, 316-321.
- Pamme, N.; Koyama, R.; Manz, A. *Lab Chip* **2003**, *3*, 187-192.
- Parpura, V.; Doyle, R. T.; Basarsky, T. A.; Henderson, E.; Haydon, P. G. *Neuroimage*. **1995**, *2*, 3-7.
- Pasquali, C.; Fialka, I.; Huber, L. A. *J. Chromatogr. B* **1999**, *722*, 89-102.
- Rastogi, V.; Velev, O. D. *Biomicrofluidics* **2007**, *1*.
- Richards, D. A.; Bai, J.; Chapman, E. R. *J. Cell Biol.* **2005**, *168*, 929-939.
- Ritchie, K.; Shan, X. Y.; Kondo, J.; Iwasawa, K.; Fujiwara, T.; Kusumi, A. *Biophys. J.* **2005**, *88*, 2266-2277.
- Rizzoli, S. O.; Betz, W. J. *Nat. Rev. Neurosci.* **2005**, *6*, 57-69.
- Rosenmund, C.; Clements, J. D.; Westbrook, G. L. *Science* **1993**, *262*, 754-757.
- Rotne, J.; Prager, S. *J. Chem. Phys.* **1969**, *50*, 4831-4837.
- Saffarian, S.; Elson, E. L. *Biophys. J.* **2003**, *84*, 2030-2042.
- Schenck, S.; Wojcik, S. M.; Brose, N.; Takamori, S. *Nat. Neurosci.* **2009**, *12*, 156-162.
- Schiro, P. G.; Kuyper, C. L.; Chiu, D. T. *Electrophoresis* **2007**, *28*, 2430-2438.
- Schivell, A. E.; Batchelor, R. H.; Bajjalieh, S. M. *J. Biol. Chem.* **1996**, *271*, 27770-27775.
- Sgro, A. E.; Allen, P. B.; Chiu, D. T. *Anal. Chem.* **2007**, *79*, 4845-4851.
- Song, H.; Chen, D. L.; Ismagilov, R. F. *Angew. Chem., Int. Ed. Engl.* **2006**, *45*, 7336-7356.
- Stevens, C. F.; Tsujimoto, T. *Neurobiol.* **1995**, *92*, 846-849.
- Sudhof, T. C. *Nature* **1995**, *375*, 645-653.
- Sudhof, T. C. *Annu. Rev. Neurosci.* **2004**, *27*, 509-547.
- Sudhof, T. C.; Jahn, R. *Neuron* **1991**, *6*, 665-677.
- Sugiyama, Y.; Kawabata, I.; Sobue, K.; Okabe, S. *Nat. Methods* **2005**, *2*, 677-684.

- Suzuki, M.; Husimi, Y.; Komatsu, H.; Suzuki, K.; Douglas, K. T. *J. Am. Chem. Soc.* **2008**, *130*, 5720-5725.
- Takamori, S.; Holt, M.; Stenius, K.; Lemke, E. A.; Gronborg, M.; Riedel, D.; Urlaub, H.; Schenck, S.; Bruegger, B.; Ringler, P.; Mueller, S. A.; Rammner, B.; Graeter, F.; Hub, J. S.; De, G. B. L.; Mieskes, G.; Moriyama, Y.; Klingauf, J.; Grubmueller, H.; Heuser, J.; Wieland, F.; Jahn, R. *Cell (Cambridge, MA, U. S.)* **2006**, *127*, 831-846.
- Tan, Y. C.; Hettiarachchi, K.; Siu, M.; Pan, Y. R.; Lee, A. P. *J. Am. Chem. Soc.* **2006**, *128*, 5656-5658.
- Taniguchi, Y.; Choi, P. J.; Li, G.-W.; Chen, H.; Babu, M.; Hearn, J.; Emili, A.; Xie, X. S. *Science* **2010**, *329*, 533-538.
- Thiele, C.; Hannah, M. J.; Fahrenholz, F.; Huttner, W. B. *Nat. Cell Biol.* **2000**, *2*, 42-49.
- Trommershauser, J.; Schneggenburger, R.; Zippelius, A.; Neher, E. *Biophys. J.* **2003**, *84*, 1563-1579.
- Wang, R.; Yu, C.; Yu, F.; chen, L. *Trends Anal. Chem.* **2010**, *29*, 1004-1013.
- Wang, X.; Wang, S.; Ma, H. *Analyst* **2008**, *133*, 478-484.
- Wienisch, M.; Klingauf, J. *Nat. Neurosci.* **2006**, *9*, 1019-1027.
- Willig, K. I.; Rizzoli, S. O.; Westphal, V.; Jahn, R.; Hell, S. W. *Nature (London, U. K.)* **2006**, *440*, 935-939.
- Wohland, T.; Rigler, R.; Vogel, H. *Biophys. J.* **2001**, *80*, 2987-2999.
- Wojcik, S. M.; Rhee, J. S.; Herzog, E.; Sigler, A.; Jahn, R.; Takamori, S.; Brose, N.; Rosenmund, C. *Proc. Natl. Acad. Sci. U. S. A.* **2004**, *101*, 7158-7163.
- Wu, C.; Hansen, S. J.; Hou, Q.; Yu, J.; Zeigler, M.; Jin, Y.; Burnham, D. R.; McNeill, J. D.; Olson, J. M.; Chiu, D. T. *Angew. chem. Int. Ed.* **2011**, *50*, 3430-3434.
- Wu, C.; Jin, Y.; Schneider, T.; Burnham, D. R.; Smith, P. B.; Chiu, D. T. *Angew. chem. Int. Ed.* **2010**, *49*, 9436-9440.
- Wu, C.; Schneider, T.; Zeigler, M.; Yu, J.; Schiro, P. G.; Burnham, D. R.; McNeill, J. D.; Chiu, D. T. *J. Am. Chem. Soc.* **2010**, *132*, 15410-15417.
- Wu, J. Q.; Pollard, T. D. *Science* **2005**, *310*, 310-314.
- Wu, W.; Xu, J.; Wu, X.-S.; Wu, L.-G. *J. Neurosci.* **2005**, *25*, 11676-11683.

- Xu, X. H.; Brownlow, W. J.; Kyriacou, S. V.; Wan, Q.; Viola, J. J. *Biochemistry* **2004**, *43*, 10400-10413.
- Yao, J.; Nowack, A.; Kensel-Hammes, P.; Gardner, R. G.; Bajjalieh, S. M. *J. Neurosci.* **2010**, *30*, 5569-5578.
- Yao, P. J. *Trends Neurosci.* **2004**, *27*, 24-29.
- Yao, P. J.; Zhu, M.; Pyun, E. I.; Brooks, A. I.; Therianos, S.; Meyers, V. E.; Coleman, P. D. *Neurobiol. Dis.* **2003**, *12*, 97-109.
- Ye, F.; Wu, C.; Chan, Y.-H.; Zhang, X.; Chiu, D. T. *J. Am. Chem. Soc.* **2011**, *133*, 8146-8149.
- Ye, F.; Wu, C.; Jin, Y.; Chan, Y.-H.; Zhang, X.; Chiu, D. T. *J. Am. Chem. Soc.* **2011**, *133*, 8146-8149.
- Ye, F.; Wu, C.; Jin, Y.; Wang, M.; Chan, Y.-H.; Yu, J.; Sun, W.; Hayden, S.; Chiu, D. T. *Chem. Commun.* **2011**.
- Ye, F.; Wu, C.; Jin, Y.; Wang, M.; Chan, Y.-H.; Yu, J.; Sun, W.; Hayden, S.; Chiu, D. T. *Chem. Commun.* **In press**.
- Yu, J.; Xiao, J.; Ren, X.; Lao, K.; Xie, X. S. *Science* **2006**, *311*, 1600-1603.
- Zeigler, M. B.; Allen, P. B.; Chiu, D. T. *Biophys. J.* **2011**, *100*, 2846-2851.
- Zhang, H.; Tumarkin, E.; Sullan, R. M. A.; Walker, G. C.; Kumacheva, E. *Macromol. Rapid Commun.* **2007**, *28*, 527-538.
- Zhang, Q.; Cao, Y.-Q.; Tsien, R. W. *Pro. Natl. Acad. Sci. U.S.A.* **2007**, *104*, 17843-17848.
- Zoccarato, F.; Cavallini, L.; Alexandre, A. *J. Neurochem.* **1999**, *72*, 625-633.

Curriculum Vitae
Dr. Jennifer Claire Gadd

EDUCATION

University of Washington Seattle, WA
Ph. D. in Analytical Chemistry, September 2012
Thesis Advisor: Professor Daniel T. Chiu
Thesis Title: "Single-Molecule Studies for the Characterization of Synaptic Vesicles"

M. S. in Chemistry, June 2006

Pacific University Forest Grove, OR
B.S. in Chemistry, May 2005

B.S. in Mathematics, May 2005

PROFESSIONAL EXPERIENCE

Graduate Research Assistant, Chemistry Department, 2005-2012
University of Washington

Teaching Assistant, Chemistry Department, 2005-2011
University of Washington

Undergraduate Research Assistant, Chemistry Department 2004-2005
Pacific University

Teaching Assistant, Chemistry Department, Pacific University 2004-2005

Chemistry Tutor, Pacific University 2003-2005

Mathematics Tutor, Pacific University 2003-2005

Mathematics Tutor, 2003
California State University, San Marcos

RESEARCH SKILLS

Graduate Research
Dr. Daniel T. Chiu, University of Washington

Primary Work:

Developing and implementing analytical techniques for characterization of nanoparticles and subcellular organelles on the single particle/organelle level

Related Work:

- Fluorescence microscopy
- Microfluidic device fabrication
- Soft lithography
- Proper handling, restraint, and use of mice
- Comprehension of Matlab, Adobe Photoshop, MetaMorph Imaging and Analysis Software, and Microsoft Office

Undergraduate Research**Dr. Kevin E. Johnson, Pacific University****Primary Work:**

Observing the pH effects on the structure of 3-mercaptopropionic acid self-assembled monolayer on gold

Related Work:

- Scanning tunneling microscopy (STM)
- Electrochemical etching for generation of STM tips

HONORS AND AWARDS

Graduated Cum Laude Pacific University	2005
CRC Press Freshman Chemistry Achievement Award California State University, San Marcos	2002

PEER REVIEWED PUBLICATIONS

(1) Schiro, P. G.; Gadd, J. C.; Yen, G. S.; Chiu, D. T. "High-Throughput Fluorescence-Activated Nanoscale Subcellular Sorter with Single-Molecule Sensitivity." *J. Phys. Chem. B* **2012**, *116*, 10490-10495.

- (2) Gadd, J.C.; Budzinski, K. L.; Chan, Y.-H.; Ye, F.; Chiu, D. T. "Probing the Interior of Synaptic Vesicles with Internalized Nanoparticles." *Proc. SPIE-Int. Soc. Opt. Eng.* **2012**, 8232.
- (3) Mutch, S. A.; Gadd, J. C.; Fujimoto, B. S.; Kensel-Hammes, P.; Schiro, P. G.; Bajjalieh, S. M.; Chiu, D. T. "Determining the Number of Specific Proteins in Cellular Compartments by Quantitative Microscopy." *Nature Protocols* **2011**, 6, 1953-1968.
- (4) Budzinski, K. L.; Sgro, A. E.; Fujimoto, B. S.; Gadd, J. C.; Shuart, N. G.; Gonen, T.; Bajjalieh, S. M.; Chiu, D. T. "Synaptosomes as a Platform for Loading nanoparticles into Synaptic Vesicles." *ACS Chem. Neurosci.* **2011**, 2, 236-241.
- (5) Mutch, S. A.; Kensel-Hammes, P.; Gadd, J.C.; Fujimoto, B. S.; Allen, R. W.; Schiro, P. G.; Lorenz, R. M.; Kuyper, C. L.; Kuo, J. S.; Bajjalieh, S. M.; Chiu, D. T. "Protein Quantification at the Single Vesicle Level Reveals that a Subset of Synaptic Vesicle Proteins are Trafficked with High Precision." *J. Neurosci.* **2011**, 3, 1461-1470.
- (6) Gregersen, K. A. D.; Hill, Z. B.; Gadd, J. C.; Fujimoto, B. S.; Maly, D. J.; Chiu, D. T. "Intracellular Delivery of Bioactive Molecules using Light-Addressable Nanocapsules." *ACS Nano* **2010**, 4, 7603-7611.
- (7) Gadd, J. C.; Kuyper, C. L.; Fujimoto, B. S.; Allen, R. W.; Chiu, D. T. "Sizing Subcellular Organelles and Nanoparticles Confined within aqueous Droplets." *Anal. Chem.* **2008**, 80, 3450-3457.